1-1-2016

Synthesis And Characterization Of Transition Metal Phosphide Nanoparticles For Catalytic Applications: Model Catalysts For Hydrodesulfurization And Electrocatalysts For The Oxygen Evolution Reaction

Don Malinda Ruchira Liyanage
Wayne State University,

SYNTHESIS AND CHARACTERIZATION OF TRANSITION METAL PHOSPHIDE NANOPARTICLES FOR CATALYTIC APPLICATIONS: MODEL CATALYSTS FOR HYDRODESULFURIZATION AND ELECTROCATALYSTS FOR THE OXYGEN EVOLUTION REACTION

by

DON MALINDA RUCHIRA LIYANAGE

DISSERTATION

Submitted to the Graduate School

of Wayne State University,

Detroit, Michigan

in partial fulfillment of the requirements

for the degree of

DOCTOR OF PHILOSOPHY

2016

MAJOR: CHEMISTRY

Approved By:

_____

Advisor Date

_____

_____

_____

DEDICATION

To my beloved parents and wife

ACKNOWLEDGEMENTS

It is an immense pleasure to pay my sincere gratitude to my advisor Prof. Stephanie L Brock, who always brought the best out of me which made the strong and professional scientist that I am today. Her guidance, mentorship and advising reveals her broad understanding of students, which lead to the great relationships that she has built with her students. She is an amazing advisor who inspires students with her passion for seeking knowledge. I consider myself so fortunate to be a Dr. Brock's student and work under her supervision during my graduate studies. Thank you very much Dr. Brock.

I am also thankful to my committee members Prof. Charles H Winter, Prof. H. Bernhard Schlegel, Prof. Eranda Nikolla and Prof. Zhixian Zhou. I highly appreciate their valuable feedback and suggestions during my research. Especially, I would like to thank Prof. Zhixian Zhou for his kindness to serve in my committee at the very last moment.

Our collaborators Prof. Mark E. Bussell and group at Western Washington University deserve my heartfelt gratitude in every aspect. Prof. Bussell is a great collaborator to work with who is always available for the discussions related to my research.

It would be a great inadequacy if I did not mention my former advisor Prof. Craig J. Eckhardt at University of Nebraska Lincoln. He was such a nice person who understood the inevitable situation that I had at that time. His support was a great deal for me to continue my graduate studies at Wayne State University.

I am also thankful for my undergraduate advisor Prof. S. P. Deraniyagala who always teaches me how to handle difficult situations in life and pushes me forward to achieve my goals.

I am also grateful to staff members in the Lumigen instrument center. Specially, training and support I received from Dr. Mie Zei with TEM, help of Dr. Philip Martin for resolving PXRD instrument issues, and assistance of Dr. Olena Danylyuk and Corey Lambert for ICP-MS

measurements were unforgettable. I should also be thanking Nestor Ocampo for resolving IT related issues.

Melissa Barton in the chemistry department does a remarkable job to ensure students' fulfillment of all the requirements to complete the PhD program successfully. I am really thankful for her assistance since I started my application process to Wayne State University. I am also grateful to other staff members of the chemistry department, especially Debbie McCreless, the late Mary Wood, Bernadette Miesik, Diane Kudla and Jacqueline Baldyga. Also a big thank goes to Science Store staff, including Joseph Oravec, Gregory Kish, Elizabeth Ries, Bonnie Cetlinski, and Jason Parizon for helping with purchasing chemicals and other required materials.

It's my pleasure to thank the past Brock group members Dr. Elayaraja Muthuswamy Dr. Layan Savithra, Dr. Yanhua Zhang, Dr. Lasantha Korala, Dr. Asha Bandara and Dr. Derak James. Dr. Savithra taught me how to set up an air sensitive reaction using Schlenk line and glove box techniques at the beginning of my research career. Dr. Bandara is being a friend of mine for nearly 15 years and she was very supportive in all the time. She never hesitated to share her knowledge during my research. She and her husband hosted me and my wife and helped us a lot during our initial settlement in Detroit.

I should mention all my current lab mates in the Brock group. I thank Roshini Pimmachcharige, Jessica Davis, Indika Hewavitharana, Da Li, Malsha Hettiarachchi and Samuel Mutinda for their support and friendship. I'm so lucky to work with and be around with such a friendly crowd. I wish them all the very best.

I also want to thank the two undergraduate researchers, David Livermore and Quintin B. Cheek. I really enjoyed working with them.

I also want to thank all the Sri Lankan community in Wayne State who help us in numerous ways in all these years.

Last, but not least, I would like to thank my parents who made a lot of sacrifices and dedications to build up the person who I am here today. Words cannot express my gratitude towards them. I hope I have done my best to achieve their dreams. Also my heartfelt thanks goes to my wife Wathsala for all her support, encouragement and motivation to achieve my goals. She made things much easier for me during this time period and thanks a lot Waths for all your patience, understanding and there for me always.

TABLE OF CONTENTS

Dedication ii

Acknowledgements iii

List of Tables viii

List of Figures ix

List of Schemes xiii

Chapter 1 – Introduction 1

1.1 Solution-phase arrested-precipitation synthesis of nanoparticles 2

1.2 Transition metal phosphides 4

1.3 Hydrodesulfurization 13

1.4 Water splitting as a renewable energy source 19

1.5 Thesis statement 21

Chapter 2 - Experimental and Materials Characterization Techniques 25

2.1 Materials 25

2.2 Experimental techniques 26

2.3 Characterization techniques 26

Chapter 3 - Simultaneous Control of Composition, Size and Morphology in Discrete $Ni_{2-X}Co_xP$ Nanoparticles 49

3.1 Introduction 49

3.2 Experimental 50

3.3 Results and Discussion 51

3.4 Conclusions 75

Chapter 4 - Synthesis of Binary and Ternary Ru-P Phases and Evaluation of OER Catalytic Activity of $Ni_{2-x}Ru_xP$ Nanoparticles 76

4.1 Introduction 76

4.2 Experimental……77

4.3 Results and Discussion……80

4.4 Conclusions……96

Chapter 5 - Probing Hydrodesulfurization Catalytic Activity of $Ni_{2-x}M_xP$ (M=Co, Ru) Nanoparticles Encapsulated in Mesoporous Silica 98

5.1 Introduction……98

5.2 Experimental……99

5.3 Results and Discussion……104

5.4 Conclusions……122

Chapter 6 - Conclusions and Prospectus 124

6.1 Conclusions……124

6.2 Prospectus……126

Appendix A - Preparation of Encapsualted Crystalline Ru_xP_y Nanoparticles 129

Appendix B - Permission/Licence Agreement for Copyright Material……132

References……137

Abstract……154

Autobiographical Statement 157

LIST OF TABLES

Table 1.1. Binary phases of transition metal phosphides reported via colloidal routes 6

Table 1.2. Amount of crude oil imported to USA from two different sources 14

Table 2.1. Anode materials with different wavelengths of X-rays produced and the suitable filters to eliminate Kβ radiation 29

Table 3.1. Ni:Co target and actual (as assessed by EDS) metal ratios, crystallite sizes (by Scherrer application to PXRD data), particle size (by TEM) and refined lattice parameters for different compositions of $Ni_{2-x}Co_xP$ 55

Table 3.2. Surface Compositions for $Ni_{2-x}Co_xP$ Nanoparticle Compositions 64

Table 4.1. Ni:Ru target and actual (as assessed by ICP-MS) metal ratios, crystallite sizes (by application of the Scherrer equation to PXRD), and particle sizes (by TEM) for different $Ni_{2-x}Ru_xP$ compositions. 86

Table 5.1. Physicochemical data for the $Ni_{2-x}Co_xP@mSiO_2$ nanocatalysts 108

Table 5.2. Dibenzothiophene HDS catalytic data for the $Ni_{2-x}Co_xP@mSiO_2$ nanocatalysts 108

Table 5.3. Dibenzothiophene HDS product selectivities at 623 K for different $Ni_{2-x}Co_xP@mSiO_2$ catalysts 114

Table 5.4. Carbon and sulfur analyses for post HDS catalysts 115

Table 5.5. Carbon analysis for the material reduced with two different P sources 117

Table 5.6. Physicochemical data for the $Ni_{2-x}Ru_xP@mSiO_2$ nanocatalysts 119

LIST OF FIGURES

Figure 1.1. Illustration of La Mer's model for the nucleation and growth of colloidal nanocrystals……..……..……3

Figure 1.2. Structure of MoS_2 catalyst……...16

Figure 1.3. Fe_2P type Ni_2P structure with square pyramidal M(2) and tetrahedral M(1) sites….17

Figure 2.1. Schematic diagram of an X-ray tube with main components…..…….....27

Figure 2.2. Illustration of X-ray generation process with the Cu metal as the anode…….....28

Figure 2.3. Illustration of Bragg's law…….. 31

Figure 2.4. Illustration of diffraction from a powdered sample……31

Figure 2.5. Different processes undergone by bombarded electrons interacting with a specimen ….…… 34

Figure 2.6. Schematic diagram of a TEM instrument with basic components……36

Figure 2.7. Basic imaging modes of TEM (a) bright Field mode (b) dark field mode…….37

Figure 2.8. SAED mode of TEM……. 39

Figure 2.9. Basic components of an EDS system……40

Figure 2.10. The basic adsorption types ……. 43

Figure 2.11. Schematic diagram illustrating the photoemission process in XPS…… 47

Figure 3.1. Orthorhombic Co_2P structure-type (left) hexagonal Fe_2P structure-type (right)….. 52

Figure 3.2. PXRD patterns for different targeted compositions of $Ni_{2-x}Co_xP$. Reference patterns for Co_2P and Ni_2P are shown for comparison with drop lines indicating the major distinguishing peaks for the two phases. The sharp peaks denoted with * arise from an internal Si standard. Peaks denoted with ■ arise from a CoP impurity……...…...…… 53

Figure 3.3. PXRD pattern of the reaction attempted to synthesize pure Co_2P……. 54

Figure 3.4. Hexagonal unit cell parameters (Ni_2P structure) plotted as a function of the Co content (polynomial fits are guides for the eye) ……..……..…….. 55

Figure 3.5. TEM images for $Ni_{2-x}CoxP$ nanoparticles (targeted com-positions indicated). The insets illustrate HRTEM images for each composition showing lattice fringes and, for x=1.75, hollow particle formation……...…….57

Figure 3.6. Histograms for the particle size distribution for different compositions of $Ni_{2-x}Co_xP$……... 59

Figure 3.7. STEM images and elemental mapping data for a $Ni_{0.67}Co_{1.33}P$ sample. In the plot of intensity vs. point number, Ni is shown in red, Co in green and P in blue…….…… 60

Figure 3.8. XPS spectra of $Ni_{2-x}Co_xP$ nanoparticle compositions: (a) Ni_2P, (b) $Co_{0.08}Ni_{1.92}P$, (c) $Co_{0.25}Ni_{1.75}P$ and (d) $Co_{0.50}Ni_{1.50}P$ in the Ni($2P_{3/2}$), Co($2P_{3/2}$) and P(2P) regions……... 62

Figure 3.9. PXRD patterns and TEM images of NiCoP nanoparticles obtained from heating at (a) 30 °C (b) 260 °C (c) 290 °C for 1.5 h with TOP:M=4.48 (reference PXRD patterns for CoO, fcc Ni, Co and for NiCoP are shown). The insets in TEM micro-graphs show HRTEM images of representative particles.....66

Figure 3.10. PXRD patterns and TEM images of products isolated after heating at 230°C for different time intervals with TOP:M=4.48. (Reference patterns for fcc Co, Ni and for CoO are shown.....68

Figure 3.11. PXRD patterns of products isolated after heating at 260°C for different time intervals with TOP:M=4.48. (Reference patterns for fcc Co and Ni are shown) 69

Figure 3.12. PXRD pattern (reference pattern for NiCoP is shown) and TEM images of nanoparticles obtained from heating at (a) 230 °C for 7.5 h (b) 260 °C for 1.5 h with TOP:M=4.48 and then at 350 °C for 4.5 h after injecting an extra 13.44 mmol of TOP……..…… 70

Figure 3.13. PXRD patterns (reference patterns for Ni, Co, and NiCoP are shown) and TEM images of nanoparticles obtained from reactions (a) initially heated at 230 °C with TOP:M=1.12 for 7.5 h (b) followed by heating at 350 °C for 4.5 h after injection of an additional 20.2 mmol of TOP. The inset shows the enlarged image to highlight the hollow particles……..…….72

Figure 3.14. PXRD patterns (reference pattern for NiCoP is shown) and TEM images of products isolated from reactions directly heated to 350 ºC for different time intervals with TOP:M=11.2……..……74

Figure 3.15. (a) PXRD pattern (reference pattern for NiCoP is shown) and (b) TEM image of nanoparticles obtained from reaction directly heating at 350 °C for 4.5 h with TOP:M=4.48…..…….…….....……74

Figure 4.1. (a) PXRD pattern and TEM image corresponding to Ru nanoparticles isolated after heating at 260 °C for 1.5 h; (b) PXRD pattern and TEM image of product isolated by heating Ru nanoparticles at 350 °C for 4 h with 6 mL of TOP……..……81

Figure 4.2. PXRD and TEM image of Ru nanoparticles heated at 350 °C for 12 h with 8 mL of TOP…….....…….……82

Figure 4.3. PXRD patterns of the product obtained by annealing the amorphous materials (a) Ru:P ~2 (b) Ru:P~1 with Ar/H_2 at 450 °C for 1 h……...……...…….83

Figure 4.4. PXRD patterns for different targeted compositions of $Ni_{2-x}Ru_xP$. Reference patterns for Ni_2P, Ru_2P and Ru are shown for comparison. Magnified peaks for the (111) reflection (calibrated against a Si internal standard) of the calibrated patterns are shown in Figure 4.5……..…….....……87

Figure 4.5. (111) reflection of PXRD patterns calibrated against Si as an internal standard…….88

Figure 4.6. TEM images for $Ni_{2-x}Ru_xP$ nanoparticles (targeted compositions indicated, with sizes obtained from size histograms (see Figure 4.7) …..…….89

Figure 4.7. Particle size histograms for different $Ni_{2-x}Ru_xP$ compositions…...……90

Figure 4.8. Elemental mapping and line scanning data for a $Ni_{1.25}Ru_{0.75}P$ particle……..……91

Figure 4.9. PXRD patterns and TEM images of Ru rich compositions (x=1.25, 1.5) prepared by the protocol given in Scheme 4.1……. .……...….92

Figure 4.10. Polarization curves for different compositions of $Ni_{2-x}Ru_xP$ nanoparticles in 1.0 M KOH…….……. 95

Figure 4.11. Change in overpotential (at 10 mA/cm^2) for different compositions of $Ni_{2-x}Ru_xP$ in 1.0 M KOH…….…….……. 95

Figure 4.12. PXRD pattern and TEM image for Ni_2P particles prepared for OER catalytic testing…….……..96

Figure 5.1. PXRD patterns and TEM images of the as prepared $Ni_{2-x}Co_xP$ nanoparticles for HDS catalytic testing. Insets show particle size distributions……..……104

Figure 5.2. PXRD patterns and TEM images of the encapsulated nanoparticles. Insets show HRTEM image for a representative particle for each composition with lattice fringes…….....…106

Figure 5.3. HRTEM image of a $Ni_{1.5}Co_{0.5}P$ nanoparticle showing lattice fringes corresponding to exposed (100) planes with 0.5 nm spacing and the {100}, {001} and {101} sets of facets……...……...….106

Figure 5.4. Nitrogen adsorption-desorption isotherms for the $Ni_{2-x}Co_xP@mSiO_2$ nanocatalysts. The inset depicts the pore size distribution calculated from the adsorption branch of the isotherm……...……..…..107

Figure 5.5. Infrared spectra of adsorbed CO on $Ni_{2-x}Co_xP@mSiO_2$ nanocatalysts……...……..110

Figure 5.6. Dibenzothiophene HDS conversion vs. temperature for $Ni_{2-x}Co_xP@mSiO_2$ nanocatalysts…….....112

Figure 5.7. Dibenzothiophene HDS TOFs vs. Co content for $Ni_{2-x}Co_xP@mSiO_2$ nanocatalysts……...…….113

Figure 5.8. Dibenzothiophene HDS product selectivities vs. temperature for (a) $Ni_2P@mSiO_2$ and (b) $Ni_{1.50}Co_{0.50}P@mSiO_2$ nanocatalyst…….....…...115

Figure 5.9. PXRD patterns for the post-HDS tested catalysts……...……..116

Figure 5.10. PXRD patterns for the encapsulated $Ni_{2-x}Ru_xP$ materials reduced with different amounts of P source…….……..118

Figure 5.11. PXRD patterns and TEM images of the encapsulated $Ni_{2-x}Ru_xP$ nanoparticles.....119

Figure 5.12. 4,6-dimethyldibenzothiophene HDS conversion vs. temperature for $Ni_{2-x}Co_xP@mSiO_2$ nanocatalysts…….……120

Figure 5.13. 4,6-dimethyldibenzothiophene HDS TOFs vs. Ru content for $Ni_{2-x}Ru_xP@mSiO_2$ nanocatalysts……..……121

Figure 5.14. 4,6-DMDBT HDS product selectivities vs. Ru content……..122

Figure A1. PXRD patterns of the encapsulated amorphous Ru:P~2 materials annealed in reducing environment under different conditions (a) annealed 450 °C for 1 h (b) annealed 500 °C for 2 h with 1 g of PPh3 (c) product from (b) step further annealed 550 °C for 2 h with no P source……..……..130

Figure A2. PXRD patterns of the encapsulated Ru nanoparticles annealed in reducing environment under different conditions (a) as encapsulated material directly reduced at 550 °C for 2 h with 1 g PPh_3 (b) encapsulated material first calcined at 425 °C for 2 h and then reduced at 550 °C for 2 h with 1 g PPh_3..... 131

Figure A3. PXRD patterns of the encapsulated amorphous Ru:P~1 nanoparticles annealed in reducing environment under different conditions (a) as encapsulated material directlyreduced at 550 °C for 2 h with 1 g PPh3 (b) encapsulated material first calcinedat 425 °C for 2 h and then reduced at 550 °C for 2 h with 1 g PPh_3 131

LIST OF SCHEMES

Scheme 1.1. Different HDS pathways for DBT molecule (direct desulfurization (DDS) vs hydrogenation (HYD) pathways)……..……...……...…....15

Scheme 3.1. Reaction protocol used for the synthesis of $Ni_{2-x}Co_xP$ nanoparticles……..…...…51

Scheme 4.1. Reaction protocol used for the synthesis of $Ni_{2-x}Ru_xP$ nanoparticles…..…….…..…84

Scheme 5.1. Protocol for the encapsulation of nanoparticles in mesoporous silica……..…100

Scheme 5.2. Dibenzothiophene HDS reaction network……...…….…..…..114

Scheme 5.3. Different HDS pathways for 4,6-DMDBT molecule (DDS vs HYD).……....…121

CHAPTER 1 INTRODUCTION

Solids with sizes less than 100 nm in one or more dimensions are considered nanomaterials. With these size boundaries, the nanomaterials exhibit unique optical, catalytic and magnetic properties relative to their bulk counterpart.[1-4] For example, gold nanoparticles ~ 30 nm in size are red in color, in contrast to the color observed for bulk gold.[5] Likewise Au nanoparticles of size 2-4 nm are catalytically active for CO oxidation, despite the inert nature of the bulk gold.[6] In general, on the nanoscale, many materials show size and shape-dependent properties.[7-9] The promising behavior of nanoscale materials make them ideal candidates for photovoltaics, biological and other technological applications.[10-12]

In order to exploit the advantages of nanomaterials, they have to be prepared in the right size, composition and shape. Accordingly, research over the last two decades has been focused on developing synthetic methodologies that enable control of size, shape and composition. With respect to transition metal pnictide (pnicogen=Group 15 elements) nanoparticles of interest for magnetic and catalytic applications,[13, 14] the Brock group has developed methods to prepare different transition metal phosphides,[15, 16] arsenides,[17, 18] and antimonides,[19] as binary phases with fine control over size, shape and composition. Very recently, the Brock group has focused on developing methodologies for bimetallic ternary phases, particularly of transition metal phosphides, in order to exploit the behavior afforded by the synergetic interaction of two metals.[20-22]

This dissertation research is focused on the synthesis of ternary phosphide nanoparticles by solution-phase arrested-precipitation reactions and evaluation of the composition-dependent catalytic activity of these ternary phases. The research work includes development of synthetic methodologies to prepare nearly monodisperse $Ni_{2-x}M_xP$ (M=Co, Ru) nanoparticles over a large composition range. Additionally, synthetic levers were identified to control the size and

morphology of $Ni_{2-x}Co_xP$ nanoparticles using Ni:Co=1:1 as a representative composition. Composition dependent hydrodesulfurization (HDS) catalytic activity was evaluated for the nanoparticles along with some preliminary oxygen evolution reaction (OER) catalytic studies for $Ni_{2-x}Ru_xP$ nanoparticles.

This chapter describes the background information relevant to colloidal synthesis of binary and ternary transition metal phosphide synthesis. Additionally, the importance of hydrodesulfurization and oxygen evolution reaction processes and application of transition metal phosphides as catalysts for these two processes is presented.

1.1 Solution-phase arrested-precipitation synthesis of nanoparticles

Solution-phase arrested-precipitation reactions provide excellent control over the synthesis of nanoparticles. In this method, precursors are decomposed/reacted in the presence of coordinating ligands. As the name suggests, the particle growth is restricted by the ligands present in the system. As the surface area of nanoparticles is large they possess high surface energy and tend to aggregate. Binding of ligands on the surface of crystals serves to minimize aggregation. Typically these ligand are long chain organic molecules either functionalized with an amine, a phosphonic acid, a carboxylic acid or a alkanethiol.[12] The chain length of the ligand can be varied depending on the requirement; shorter chains promote particle growth and limit inter particle spacing. As these ligands have very high boiling points, materials can be synthesized at high temperatures to obtain well crystallized products. As the polarity of the ligands on the nanoparticle surfaces are modified, these particles can be dispersed in different solvents. Depending on the binding affinity of ligands on certain facets, different morphologies could be obtained for the same composition, as growth of particles is expected to be more rapid on unpassivated facets.[23-25]

To explain the growth of nanoparticles in the solution phase, La Mer's model can be used and Figure 1.2 illustrates different processes taking place in particle growth according to this model.[26] When the precursors are rapidly injected into a hot coordinating solvent, thermal decomposition of precursors takes place forming monomers. Once the monomer concentration becomes supersaturated it starts forming nuclei and this process takes place until the monomer concentration reaches a critical concentration known as nucleation threshold. After this point, formation of new nuclei ceases and particle growth takes place with addition of the remaining monomers to the already formed nuclei. When the monomer concentration is further reduced, particle growth takes place with Ostwald ripening. In Ostwald ripening, larger particles grow at the expense of smaller particles (with higher surface energy), which dissolve. Temperature, time and surfactant can be used to control the rate of nucleation and growth of nanoparticles.

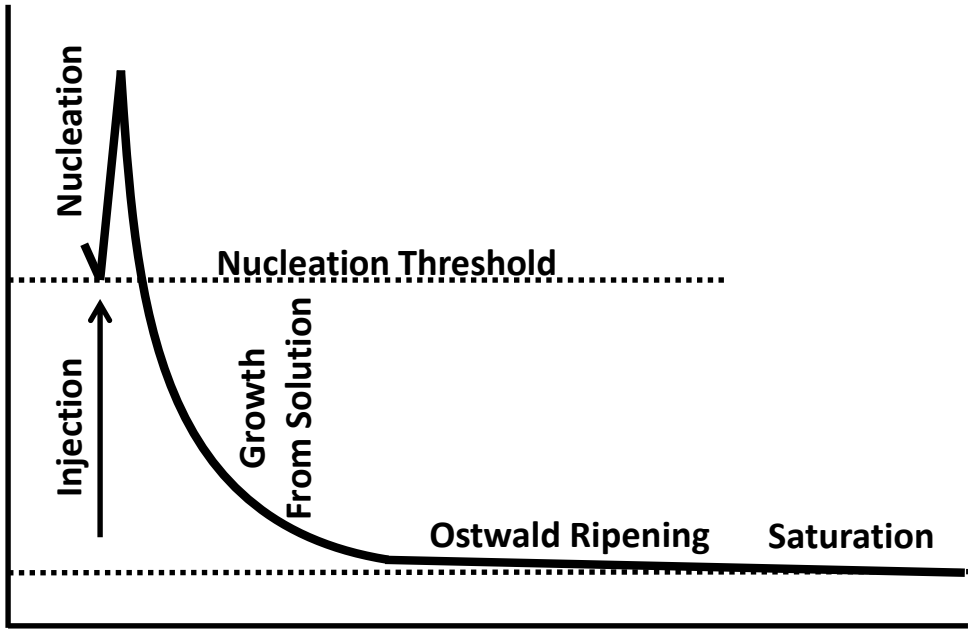

Figure 1.1. Illustration of La Mer's model for the nucleation and growth of colloidal nanocrystals (adapted from Kilmov)[26]

1.2 Transition metal phosphides

1.2.1 Binary transition metal phosphides

Binary transition metal phosphides are versatile materials that can be used in diverse applications in energy storage,[27, 28] catalysis[14, 29], magnetism,[13] and optics.[30] With respect to catalysis, transition metal phosphides have recently drawn much attention for the hydrogen evolution reaction,[31] oxygen evolution reaction,[32] hydrodeoxygenation,[33] and hydrodesulfurization.[34] These materials can exist in different stoichiometries and structures, with metal-rich phases exhibiting metallic character and phosphorous-rich phases covalent character.[29] From X-ray absorption studies, Mar and coworkers revealed the electronic structure of metal-rich phosphides is similar to the corresponding pure metals.[35] Due to the existence of different phases, the same metal in different compositions shows different properties. For instance, Ni_2P is a very promising hydrotreating catalyst while Ni_5P_4 can be used as a lithium intercalation material in battery applications.[36, 37] Among Fe-P phases, FeP_2 is a small bandgap semiconductor while Fe_3P is a ferromagnet with a high transition temperature (T_c=692 K).[14] Due to the promising properties exhibited on the nanoscale, there has been considerable effort expanded to prepare transition metal phosphides on the nanoscale as described below.

1.2.2 Synthesis of binary transition metal phosphides

Historically, solvothermal methods have been used to prepare transition metal phosphides. This method involves heating at a temperature above the boiling point of the solvent in a closed vessel. Qian and coworkers prepared different metal phosphides using metal salts along with sodium phosphide and white phosphorous (P_4) as the P sources.[38, 39] In 2008 Gillan and coworkers reported the synthesis of P rich transition metal phosphides using metal chlorides and yellow phosphorous as precursors.[40] The materials prepared via solvothermal methods suffer from large

polydispersity and aggregation of particles, making it difficult to study the size-dependent properties.

Temperature programmed reduction (TPR) method has also been employed in transition metal phosphide synthesis. In this method, first precursor materials are incorporated on a support such as silica by the incipient wetness impregnation method. In the impregnation method precursors are dissolved in a solvent and added to the support in portions (For example in the case of Ni_2P, according to the synthesis reported by the Bussell group, $Ni(NO_3)_2.6H_2O$ and $NH_4H_2PO_4$ are dissolved in water).[41] In the addition process, the volume should be equal to the pore volume of the support. Capillary action draws the solution into the pores of the support. If the solution volume is larger than the pore volume, a diffusion process takes places, which is much slower. The solvent can be removed from the support by drying and calcination in air. Subsequently, the oxide material formed is subjected to a reduction process by the TPR method to obtain the required phase. In the TPR method H_2 gas mixed with an inert gas (N_2, Ar) is passed over the sample at variable temperatures and the reduction process can be monitored by probing the consumption of H_2 at different temperatures. A higher consumption of H_2 gas indicates the reduction process is taking place [42, 43] Generally after the reduction step the sample is passivated with about 1 mol% O_2/He mixture to prevent pyrophoric reaction upon contact with air. The disadvantages of this technique include, the inhomogeneous nature of particles and particle sizes are defined by the support interaction.

Solution-phase arrested-precipitation reactions have been used by different groups to prepare binary transition metal phosphides with more control over the size, shape and composition enabling the effect of these parameters on catalytic activity. Table 1.1 illustrates the different transition metal phosphides that were being accessible via solution phase routes.

Table 1.1. Binary phases of transition metal phosphides reported via colloidal routes

7	8	9	10
MnP[44,45]	Fe_2P[15,45,47] FeP[15,45,46]	Co_2P[48,49] CoP[49]	Ni_2P[16,50] $Ni_{12}P_5$[16] Ni_5P_4[56] NiP_2[56]
		Rh_2P[50]	Pd_5P_2[50] PdP_2[50]
			PtP_2[50]

With respect to Mn-P phases the Brock group developed a protocol for the synthesis of MnP nanoparticles using the Mn(0) complex ($Mn_2(CO)_{10}$) as the metal precursor and $P(Si(Me_3)_3$ as the P source.[44] The size of the particles could be adjusted by the temperature and the time scale of the reaction. For example, a reaction at 220 °C for 24 h resulted in particles of diameter 5.11±0.48 nm whereas reaction at 250 °C for 18 h followed by 220 °C for 18 h produced 6.67±0.33 nm nanoparticles. The Brock group further evaluated the potential of using a different type of P source other than $P(Si(Me_3)_3$, which is very expensive and highly reactive. They found alkyl phosphines (trioctylphosphine, TOP) can also contribute P in the formation of MnP. Although high temperatures (ca. 300 °C) are required to break P-C bond in TOP, the lower reactivity, toxicity and cost of TOP make it an ideal P source in metal phosphide nanoparticle synthesis.[29]

Hyeon and coworkers reported the synthesis of 1-D metal phosphide nanoparticles including MnP, by injecting a M-TOP complex into a hot surfactant solution.[45] They used a syringe pump in order to maintain a continuous and constant flow rate of metal precursor, which led to uniform nanorods that could not be obtained by rapid injection. In the case of MnP, the Hyeon group used $Mn_2(CO)_{10}$ as a precursor and the nanorod preparation was carried out in the presence of TOPO as the surfactant and solvent at 330 °C. The dimensions of the nanorods could be varied from 8×16 nm and 6×22 nm using 10 mL/h and 20 mL/h injection rates respectively. When $Mn(acac)_2$ was used as the metal precursor, no nanocrystals were obtained indicating the importance of the precursor for phosphide nanoparticle synthesis. When the reaction was carried out using octyl ether

and oleylamine, spherical MnO nanoparticles were obtained, thus underscoring the critical nature of the solvent system for the final product. The growth direction of nanorods for each phase was assigned with PXRD and HRTEM data and it was revealed that MnP grows perpendicular to the (002) series of planes. The rod formation was explained, due to the differences in binding affinity of ligands to different crystal facets during the growth process.

With respect to Fe-P phases, the Brock group reported the synthesis of FeP using $Fe(acac)_3$ and (trimethylsilyl)phosphine ($P(Si(Me_3)_3$) as the precursors, using trioctlyphosphine as the solvent at temperatures 240-320 °C.[46] They also studied the effect of coordinating solvents on the final product using different ligands, such as dodecylamine (DA), myristic acid (MA) and hexylphosphonic acid (HPA). The DA and MA capped particles resulted in similar sizes ~5 nm with FeP as the only crystalline product, but in the presence of HPA, no final product could be isolated.

Later a systematic study was carried out by the Brock group for the preparation of different phases of iron phosphide nanoparticles.[15] In this study, pre-prepared iron nanoparticles with spherical morphology were converted to the phosphide phase by the reaction of TOP, using oleylamine as the stabilizing ligand and octadecene as the solvent. Two strategies were followed: (i) injection of TOP to the metal nanoparticles at 200 °C followed by heating to elevated temperatures (350-385 °C) (ii) cannulation of nanoparticles at 200 °C to pre-heated TOP maintained at 350 -370 °C. A series of reactions were carried out via both pathways, varying heating temperature, time, and reactant concentration independently, in order to identify optimal conditions to obtain phase-pure Fe_xP_y materials. Fe_2P was observed to form at shorter reaction times, adopting a rod morphology (occasionally with voids due to the Kirkendall effect). At longer reaction times and higher temperatures, Fe_2P incompletely transformed to spherical FeP

nanoparticles. However, when the cannulation method was used, phase-pure FeP can be produced as clean samples, free of ferromagnetic impurities. It was hypothesized that this route avoids formation of Fe_2P intermediates that are resistant to complete conversion. Conversion of Fe to Fe_2P or Fe_2P to FeP did not appear to be happening topotactically.

Hyeon and coworkers also studied the Fe-P system using their continuous injection approach. Fe_2P and FeP nanorods were synthesized by injection of an Fe-TOP complex (prepared by the reaction of $Fe(CO)_5$ and TOP) at varying temperature (300 °C for Fe_2P and 360 °C for FeP) in the presence of TOPO. Hyeon group observed that with oleylamine instead of TOPO, Fe_2P was the final phase (360 °C) and attributed this to the P rich environment in the presence of TOPO.[45, 47]

With respect to Co-P phases, the Robinson group synthesized Co_2P hyperbranched nanocrystals by the reaction of $Co(oleate)_2$ with trioctylphosphine oxide (TOPO) at 350 °C.[48] In this study, it was identified that TOPO is not only acting as the coordinating solvent but also as the P source. Robinson group also reported, by varying the concentration of the surfactant the morphology of the hyperbranched structures could be tuned from six-arm symmetric star structures to sheaflike structures.

In a separate study by the Robinson group structural evolution and diffusion during the transformation of different Co-P phases were studied.[49] First, Co nanoparticle were prepared at 180 °C using $Co_2(CO)_8$ as the precursor, and these particles were converted to phosphide phases under different conditions. To prepare the Co_2P phase the reaction was carried out 1h at 300 °C in the presence of 3 mL of TOP. About 70% of the resultant particles were hollow, with average sizes of 12.8 nm. For the CoP phase, the reaction was conducted at 350 °C for 2.5 h in the presence of 15 mL TOP. Only a few of the particles were hollow, with average sizes of 16.2 nm. According to the Robinson group's findings, during the transformation from Co to Co_2P phase, P diffuses into

the Co lattice and forms an amorphous Co-P layer first. When Co is the majority phase inside the core, P diffuses inside faster than the outward diffusion of Co. Once Co_2P becomes the majority phase the progression of Co outward becomes faster, resulting in hollow particles due to the Kirkendall effect.

With respect to Ni-P phases, the Schaak group prepared Ni_2P nanoparticles using $Ni(acac)_2$ and TOP as precursors.[50] In their synthesis, metal nanoparticles were prepared first and subsequently transformed to metal phosphides by phosphidation with TOP at 300 °C. As the final product hollow particles formed, attributed to the Kirkendall effect previously observed by Alvisatos and coworkers for metal chalcogenide nanocrystals.[51] The Kirkendall effect is caused by the difference in the diffusion rates of different elements. In the case of metal phosphide formation, inward diffusion of P is slower compared to the outward diffusion of metal, which causes a hollow structure in the final particle. The manifestation of this effect depends on many factors such as size of the precursor particle, metal, and concentration of P inside and outside of the particle. In parallel to the Schaak group's work, Chiang and coworkers prepared Ni_2P nanoparticles (at 320 °C) by phosphidation of pre-prepared Ni nanocrystals (prepared by the reaction of $Ni(acac)_2$ in the presence of TOPO and oleylamine at 250 °C). They also observed hollow particle formation due to Kirkendall effects.[52]

Systematic studies of the synthesis of nickel phosphides were performed by the Brock group with a study carried out to understand how synthetic parameters govern the phases of nickel phosphide; Ni_2P vs $Ni_{12}P_5$.[16] In this study a solvent system of octyl ether (solvent) and oleylamine (reducing agent and coordinating ligand) was employed along with $Ni(acac)_2$ and TOP to make crystalline Ni or amorphous Ni_xP_y nanoparticles at intermediate temperatures (200-230 °C), which were subsequently converted to crystalline Ni-P phases with the introduction of additional TOP at

elevated temperatures (300-350 °C) . The intermediate particles acted as templates for the final crystalline particles and the nature of these intermediate particles was governed by the initial metal:P ratio. In this study different synthetic levers were identified to control the phase and morphology of Ni-P nanoparticles. A larger TOP quantity, longer heating times and higher reaction temperatures favor the Ni_2P phase while a larger oleylamine quantity favors the $Ni_{12}P_5$ phase and results in particles with smaller voids (reduction of Kirkendall effect). In their recent review, Sanchez and coworkers proposed three reasons for the favorable formation of $Ni_{12}P_5$ in the presence of larger amounts of oleylamine.[53] First, amine reduces the Ni(II) precursor and favors the fast formation of Ni(0) nuclei, which prevents the interaction of TOP with unsaturated Ni(0) nuclei to cleave the P-C bonds due to steric effects of amine ligands. Second, formation of Ni-amido complexes modifies the surface free energy of Ni nanoparticles, favoring the formation of Ni rich phases due to thermodynamics. Third, amines diminish the inclusion of third party elements (either N or C) to the nanoparticles which favor the formation of tetragonal $Ni_{12}P_5$ phase over hexagonal Ni_2P.

Later, the Brock group reported that different sizes of Ni_2P nanoparticles could be prepared by varying the oleylamine amount.[54] In contrast to the report of Sanchez and coworkers the oleylamine quantity is proportional to the Ni_2P particle size enabling sizes ranging from ~5-15 nm.[55] Due to the larger amount of oleylamine present in the reaction, formation of Ni-P nuclei is limited as oleylamine will inhibit the reaction of Ni(0) and TOP. This decreases the concentration of Ni-P nuclei formed initially, which can subsequently grow to larger particles.

Ni-P phase studies were further continued by the Brock group with the preparation of more P-rich phases; Ni_5P_4 and NiP_2 from reaction of Ni(II) salts or Ni(0) complexes with TOP in octyl ether and oleylamine.[56] Synthetic levers were optimized to obtain phase pure Ni_xP_y phases and it

was identified that for a constant Ni precursor concentration, increasing the time, temperature and TOP/oleylamine ratio favors the phosphidation process. It was further revealed that the intermediate step at 230 °C hinders the formation of P-rich phases, even with very high TOP/M ratios. At larger concentrations of oleylamine, different Ni precursors (Ni(II)acetylacetonate, Ni(II)acetate, and bis(cyclooctadiene)Ni(0)) resulted in formation of Ni_5P_4 as the major phase unless the TOP/M ratio is dramatically reduced.

With respect to the noble metal phosphides, the Schaak group synthesized PtP_2, Rh_2P, PdP_2 and Pd_5P_2 nanoparticles by the phosphidation of the preformed metal nanoparticles.[50] A number of recent review articles on transition metal phosphide nanoparticles and their applications have been published. In these articles the authors discuss in detail the approaches used by different groups to prepare different transition metal phosphides.[29, 31, 53, 57]

1.2.2 Ternary transition metal phosphides

Although binary phases of metal phosphides have been extensively studied on the nanoscale, only recently have researchers started exploring ternary phases, despite the opportunities for synergism presented by bimetallic systems. However, the properties of bulk phases are well established. Fruchart and coworkers provided the phase diagrams with lattice parameters and magnetic data for ternary transition metal phosphides comprising different metals (Cr, Co, Fe, Mn, Ni).[58]

Until very recently there have been very few reports on the synthesis of bimetallic ternary metal phosphides by colloidal routes. In 2008, Hyeon and coworkers reported the synthesis of Ni-Fe-P nanorods by the thermal decomposition of metal-TOP complexes.[59] In a typical synthesis, a Ni-TOP complex formed by the reaction of $Ni(acac)_2$ and TOP was injected into a solution containing a Fe-TOP complex formed by the reaction of $Fe(CO)_5$ with TOP. Three different

compositions of $Ni_{2-x}Fe_xP$ (x=0.75, 0.8, 0.9) nanorods were prepared by this synthesis. It was revealed that continuous and constant injection by a syringe pump is critical to get low polydispersity nanorods. As previously mentioned the formation of anisotropic structures is related to the binding affinity of TOP ligands to certain facets and, there is a critical concentration of TOP required to obtain the nanorod morphology.

In 2011, Han and coworkers reported the synthesis of $Co_{2-x}Fe_xP$ nanostructures by the reaction of metal oleate complexes with TOP in the presence of oleylamine.[60] Temperature-dependent composition and morphology were observed for a reaction comprising Co:Fe=1:2 ratio. At 290 °C, $Co_{1.5}Fe_{0.5}P$ was obtained adopting rice-shaped nanorods whereas at 320 °C, split nanostructures were obtained of $Co_{1.7}Fe_{0.3}P$ composition.

In 2011, Whitmire and coworkers reported the synthesis of Fe-rich ($0.15 \leq x \leq 0.7$) $Fe_{2-x}Mn_xP$ nanoparticles by the thermal decomposition of a single source molecular precursor $FeMn(CO)_8(\mu\text{-}PH_2)$ in the presence of oleic acid and hexadecylamine.[61]

In 2015, Sun and coworkers demonstrated the anisotropic growth of $Co_{2-x}Fe_xP$ nanoparticles during the conversion of Co-Fe-O to the phosphide phase.[62] The oxide particles were synthesized by the thermal decomposition of acetylacetonate (acac) precursors. In the presence of oleylamine and oleic acid as surfactants, polyhedral structures were obtained, whereas adding sodium oleate to the reaction led to the formation of cubic-shaped oxide particles. During the conversion, polyhedral particles lead to the formation of nanorods ($Co_{0.94}Fe_{1.06}P$, $Co_{1.58}Fe_{0.42}P$) and cubic particles resulted in sea-urchin-like particles ($Co_{0.48}Fe_{1.52}P$, $Co_{1.08}Fe_{0.92}P$).

Recently the Brock group extended their expertise for binary phosphide phase synthesis to ternary phases ($Ni_{2-x}Fe_xP$, $Co_xFe_{2-x}P$ and $Co_{2-x}Mn_xP$). Different approaches have been followed depending on the targeted metals. For the $Ni_{2-x}Fe_xP$ system ($0 \leq x \leq 2$), amorphous Ni_xP_y

nanoparticles were prepared first by the reaction of $Ni(acac)_2$ with TOP at 230 °C followed by the introduction of iron precursor in the Fe(0) state to form the amorphous mixed metal phosphide phase. Subsequently, the amorphous phase materials were converted to crystalline phase by increasing the temperature to 350 °C. A composition-dependent morphology was observed for these materials; Ni-rich materials adopt spherical morphology whereas Fe-rich products adopt rod-shape morphology.[20] A synthetic protocol was also developed for the preparation of $Co_xFe_{2-x}P$ nanoparticles ($0 \leq x \leq 2$). In this synthesis the preformed Co_xFe_{1-x} alloy precursor particles (at 200 °C) were converted to the crystalline ternary phosphide phase by reaction with TOP (330-350 °C). The resultant particles were hollow due to the Kirkendall effect. Particles sizes could be tuned from 12-22 nm by varying the oleylamine/M ratio.[22] Finally the preparation of CoMnP nanoparticles with size 4.59 ± 0.76 nm was reported. In the preparation, CoMn precursor particles formed at 200 °C were converted to the final phase by the reaction with TOP at 350 °C.[63]

1.3 Hydrodesulfurization

Increasingly stringent regulations on the allowed sulfur content in diesel fuel is necessitating new approaches for removing sulfur impurities in processing of fossil fuels.[64] The SO_x emitted during burning of fossil fuel can cause acid rain and S residues present in fuel can inhibit the catalyst present in the catalytic converters of automobiles, resulting in emission of many non-combusted hydrocarbons and poisonous oxides.[65] The issue with sulfur in the USA has intensified by the gradual shift of oil sources from the conventional Saudi Arabian oil to the Canadian oil sands. In conventional oil, about 1.8 wt % sulfur is present, whereas in Canadian oil sands the percentage is 5 wt%.[66] Table 1.2 shows the imported amounts from the two sources at two different time periods revealing this shift.

The most commonly used industrial process to remove sulfur from crude oil is hydrodesulfurization (HDS). It is a hydro-treating catalytic process that requires a catalyst at high temperature and pressure due to the high activation barrier for the desulfurization reaction. The sulfur compounds present in crude oil can be categorized into four groups according to HDS reactivity. Sulfur compounds with (i) alkyl benzothiophenes, (ii) dibenzothiophenes and alkyl dibenzothiophenes without alkyl groups at 4- and 6- positions (iii) alkyl dibenzothiophenes with one alkyl group either at 4- or 6- positions (iv) alkyl groups at both 4- and 6- positions. The latter compounds with the alkyl groups at 4- and 6- positions are known as refractory compounds and are hard to desulfurize due to steric and electronic effects.[65]

Table 1.2. Amount of crude oil imported to USA from two different sources (data source: US energy information administration)

Crude oil sources	**In May 2000 (Thousand barrels)**	**In May 2016 (Thousand barrels)**
Saudi Arabian	48,554	36,313
Canadian	59,123	110,694

The hydrodesulfurization process can take place by two different pathways. Scheme 1.1 illustrates the two pathways for a dibenzothiophene (DBT) molecule a member of group(ii). In the direct desulfurization (DDS) pathway, the S atom is directly removed from the molecule due to the direct cleavage of the C-S bond. In this case the S atom directly binds to the catalyst surface. In the hydrogenation (HYD) pathway, hydrogenation of aromatic rings takes place first, followed by the cleavage of the C-S bond. The pathway is determined by the steric bulk of the sulfur containing molecule and the nature of the catalyst. Molecules like thiophene easily undergo the DDS pathway whereas bulky molecules like 4,6-DMDBT, that have steric bulk protecting the C-

S bond, undergo the HYD pathway. After the hydrogenation of the aromatic rings, the molecule loses planarity and the sulfur is then able to bind to the catalyst surface.[67, 68]

Scheme 1.1 Different HDS pathways for DBT molecule (direct desulfurization (DDS) vs hydrogenation (HYD) pathways)

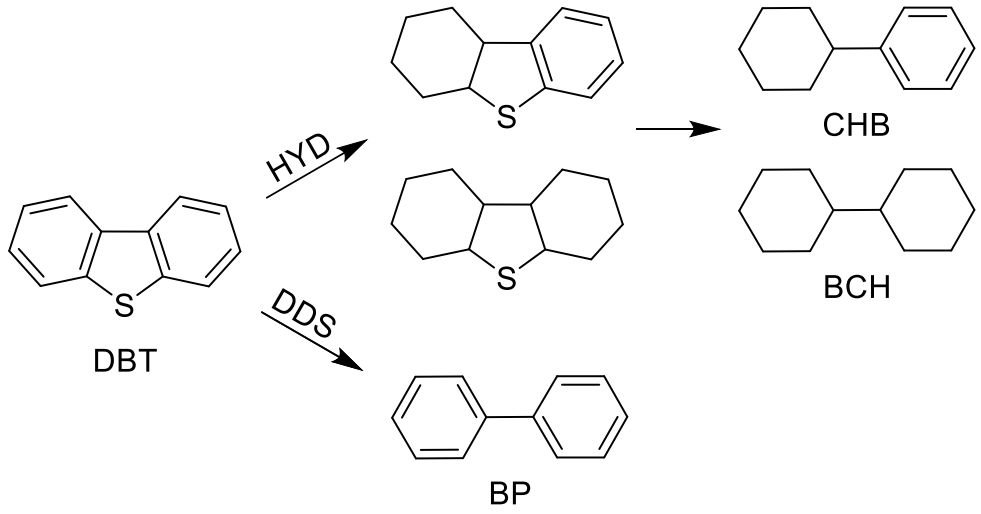

1.3.1 Conventional industrial HDS catalyst: Ni or Co promoted MoS_2

The currently used industrial catalyst for hydrodesulfurization is MoS_2, promoted either with Co or Ni. The promoter is purported to change the electronic nature of the Mo atom, thereby enhancing the catalytic activity. The Mo atoms are exposed only on edge planes (Figure 1.2), limiting the site density for catalytic activity. Considerable research has been done to improve the conventional catalyst systems with a two fold increase in activity gained over the last thirty years.[66] However, it is not clear whether these types of catalyst can produce the low sulfur levels that will only be achieved by removal of the most refractory thiophenes. As a result, other types of catalysts have been investigated for the HDS process.

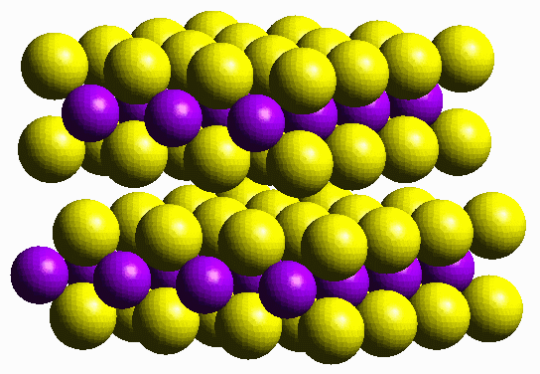

Figure 1.2. Structure of MoS_2 catalyst[67]

1.3.2 Binary metal phosphides for HDS

Among alternative HDS catalysts, transition metal phosphides have been extensively investigated due to the isotropic nature of these materials which, if properly optimized, should result in a higher density of catalyst sites. Oyama and coworkers studied dibenzothiophene (DBT) HDS catalytic activity of different metal phosphides supported on silica prepared via conventional temperature program reduction. They observed the activity of these phosphides increased in the order $Fe_2P<CoP<MoP<WP<Ni_2P$.[36] Since then Ni_2P has been studied by different groups to assess the effects of preparation methods, supports and other variables to obtain the best HDS activity and stability.

1.3.2.1 Ni_2P as a HDS catalyst

Ni_2P adopts the Fe_2P-type hexagonal crystal structure with two different metal sites. The Ni(1) site is coordinated to four P atoms with tetrahedral geometry and the Ni(2) site is coordinated to five P atoms forming a square pyramidal geometry (Figure 1.4).[69] Two alternative atomic layers with stoichiometries Ni_3P and Ni_3P_2 alternate along the (0001) direction to build up the bulk Ni_2P structure.[34] It has been purported that surface Ni(2) sites favor the HYD pathway while Ni(1) sites favor the DDS pathway.[70]

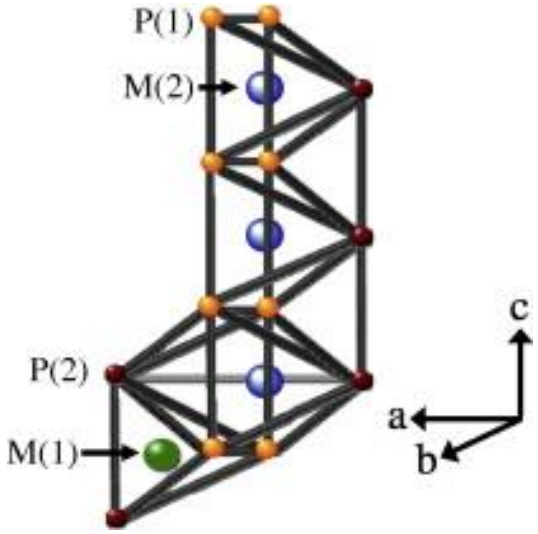

Figure 1.3. Fe_2P type Ni_2P structure with square pyramidal M(2) and tetrahedral M(1) sites (Copyright from Elsevier 2010)[69]

1.3.3 Ternary nickel phosphide systems for HDS

In order to augment the activity of Ni_2P, incorporation of a secondary metal has been explored. Bussell and coworkers studied the thiophene HDS catalytic activity of silica supported Ni_2P incorporated with Fe or Co as a second metal. From $Ni_{2-x}Co_xP$ materials about a 34% increase in activity was observed for the nominal composition $Ni_{1.92}Co_{0.08}P_{1.6}$. The higher activity was observed for nickel rich compositions and activity went down with increasing Co.[71] They did a similar systematic study on $Ni_{2-x}Fe_xP$ materials, and again, the highest activity was shown for a nominal composition $Ni_{1.97}Fe_{0.03}P_{2.0}$. From Mössbauer spectroscopy, they found for Ni-rich $Ni_{2-x}Fe_xP$ materials, the Ni prefers to occupy M(2) sites and with increasing Fe amount, M(1) sites are preferred (Fe preferentially resides in M(2) sites for ca. $x>0.6$).[69] They attributed the higher activity of Ni-rich compositions to the surface enrichment of P related to the preferential segregation of Ni into M(2) sites, which inhibits S poisoning during the catalytic process.

Smith and coworkers studied the 4,6-dimethyldibenzothiophene (4,6-DMDBT) HDS catalytic activity for $Ni_{2-x}Co_xP$ materials and observed the highest activity for a material of nominal composition $Ni_2Co_{0.08}P$. For this composition, they observed the DDS product selectivity increases

to 49% compared to the <3% DDS selectivity for Ni_2P. The shift in the selectivity was attributed to the higher number of acidic sites present on the $Ni_2Co_{0.08}P$ catalyst surface, as probed by n-propylamine titration. They concluded that the acidic sites promote the isomerization of the 4,6-DMDBT molecule to undergo the DDS pathway preferably.[72]

Oyama and coworkers studied the 4,6-DMDBT HDS activity for TPR prepared $Ni_{2-x}Fe_xP$ materials and observed a shift in the product selectivity towards the DDS pathway with increasing Fe. Extended X-ray absorption fine structure (EXAFS) studies were conducted for three $Ni_{2-x}Fe_xP$ compositions (x=0.5, 1, 1.5) and it was revealed that substitution of Fe for Ni on M(2) sites is most likely to happen for x=1 and 1.5 compositions (consistent with Mössbauer studies from the Bussell group, substitution takes places ca. x>0.6). As a consequence of the substitution of M(2) sites, which are responsible for the HYD pathway, with Fe atoms in Fe-rich compositions, the product selectivity is changed towards the DDS pathway. IR spectroscopic analysis of CO adsorbed on the catalyst surface revealed that the bond frequency decreased with increasing Fe. They concluded there is a donation of electron density from Fe to Ni atoms.[73, 74]

1.3.5 Solution-phase synthesis of Ni_2P for HDS studies

In 2007, the Brock group reported the use of discrete Ni_2P nanoparticles (~10 nm) prepared via solution-phase methods as model catalysts for thiophene HDS. The surface ligation chemistry of the particles was found to modify the activity and stability of the nanocatalyst under harsh HDS conditions (500 K-650 K, 3 MPa).[75] In later work reported by the Brock group, the size-dependent HDS catalytic activity of Ni_2P nanoparticles was evaluated. For the study, three different sizes of Ni_2P nanocrystals (~5 nm, ~10 nm, ~15 nm) were prepared via colloidal routes and incorporated onto a silica support by incipient wetness impregnation method. Particles were found to have low activity attributed to sintering under strong HDS conditions. To avoid sintering, an approach to

encapsulate nanoparticles in a mesoporous silica matrix was developed, which enabled excellent thermal and phase stability of Ni_2P under HDS conditions.[54] Recently, Jin and coworkers reported the synthesis of Ni_2P nanoparticles in solution phase (at 330 °C) using triphenylphosphine (TPP) as the P source. In the synthesis, the metal and P precursors were combined with an MCM-41 support at the outset. Thus, they obtained in-situ supported Ni_2P particles as the final product. By varying the temperature of the system they were able to prepare different phases (Ni, $Ni_{12}P_5$, Ni_2P). During DBT HDS studies, they reported that solution-phase prepared materials showed better activity compared to the TPR-prepared materials, attributed to the better dispersion of particles and lower concentration of P on the surface of the catalyst.[76]

1.4 Water splitting as a renewable energy source

With the rapid growth of the global population, energy consumption in 2010 (17 TW) is anticipated to boost up to 27 TW by 2040. Due to their high energy density and ease of combustion, fossil fuels have served as the most reliable energy source to date. However, with the continued depletion of fossil fuel energy sources and environmental issues, like the greenhouse effect, caused by the burning of fossil fuel, global attention has shifted to alternative energy sources. Solar, wind and other renewable energy sources are excellent alternatives for fossil fuel, but these sources are dependent on the time of the day and weather, thus requiring sophisticated energy storage technologies.

With respect to storage of energy in a chemical bond, molecular hydrogen is an ideal source as it has a high specific energy and emits water as the only combustion product. Hence, it is important to find affordable, clean and scalable methodologies to produce H_2. A common approach used currently in the production of H_2 is steam-methane reforming at high temperatures, which again raises environmental issues due to the emission of CO_2.[57] As a solution to this energy crisis,

production of hydrogen by water splitting has drawn much attention.[77-79] Water splitting is an electrochemical process that splits water into molecular H_2 (at the cathode) and O_2 (at the anode). It has a free energy of 237.2 kJ/mol under standard conditions, which makes it a highly endothermic reaction requiring (ideally) 1.23 V per electron transferred. Production of clean H_2 fuel by water splitting is limited by the sluggish kinetics of the oxygen evolution reaction (OER) at the anode, which involves a 4-electron oxidation process ($2H_2O \rightarrow 4H^+ + O_2 + 4e$). Hence, electrocatalytic water splitting processes require an efficient catalyst to reduce the overpotential associated with the more challenging OER process to increase the rate. Density functional theory based OER studies predict a volcano type activity plot for different materials and Ru oxides exist near the top.[80, 81] Thus, Ru based materials have emerged as one of the most promising and largely studied materials in OER.[82-88] Despite high activity, scarcity and cost of noble metals pose limitations for their use in large scale applications. Recent efforts have focused on developing catalysts from Earth-abundant and inexpensive metals. Non-noble transition metal phosphides have recently emerged as efficient catalysts for water splitting due to their activity, stability and good electrical conductivity.[31, 89]

1.4.1 Binary and ternary metal phosphides as OER catalysts

The Schaak group first reported the high hydrogen evolution reaction (HER) catalytic activity of Ni_2P in acidic solution and activity was attributed to the exposure of (001) facets on the surface of nanoparticles.[90] Since then, transition metal phosphides have been widely studied as electrocatalysts for water splitting. With respect to OER, cheap and Earth-abundant binary metal phosphides have been evaluated and among them, Ni_2P and CoP have been widely studied and shown promising activity as catalysts.[91-95] Du and coworkers studied OER catalytic activity for different morphologies of Ni_2P; nanowires and nanoparticles yielded ~400 mV and ~500 mV

overpotentials respectively.[92] Li and coworkers observed a 400 mV overpotetntial for a CoP hollow polyhedron catalyst.[95] Recently, researchers have focused on ternary phases to obtain better activity via synergetic interaction of two different metals. In OER, ternary phosphide systems comprising two metals from Ni, Fe, Co, Mn have shown enhanced activity compared to the binary counterparts, as assessed by the overpotentials required to reach a current density of 10 $mAcm^{-2}$. Li et al prepared CoMnP nanoparticles by colloidal routes and evaluated their OER catalytic activity, observing the lowest overpotential (0.33 V) for CoMnP compared to the Co_2P (0.37 V) and $CoMnO_2$ (0.39 V) phases.[63] Garcia et al. prepared different morphologies of CoFeP nanoparticles by converting the oxide phase materials to phosphide and evaluated the OER catalytic activity for different compositions. They observed the highest catalytic activity to be shown by sea-urchin like materials with the composition $Co_{1.08}Fe_{0.92}P$, exhibiting an overpotential of 0.37 V in 0.1M KOH. These materials outperformed the commercial Ir catalyst as well as the binary Fe_2P and Co_2P phases.[62] Read et al. recently prepared metal phosphide films using commercially available metal foils and observed the highest OER catalytic activity (lowest overpotential) for NiFeP (0.28 V) compared to binary phases Ni_2P (0.34 V), Co_2P (0.37 V) and Fe_2P (0.39 V).[96]

1.5 Thesis statement

Increasingly stringent regulations on the allowed sulfur content in diesel fuel combined with a switch to crude oil sources with higher impurity concentrations is necessitating new approaches for removing sulfur impurities in the processing of fossil fuels. Hydrodesulfurization (HDS) is the common industrially-used hydro-treating process to remove sulfur compounds from crude oil in the refining process.[65] Different catalysts have been studied for this process, including sulfides of Co-Mo, Ni-Mo, and Ni-W, supported on silica or alumina. Among catalysts, sulfided

molybdenum-based materials are the most widely used commercially. However, the lamellar structure of these materials, which results in metal sites exposed on edge planes only, results in low active site density, limiting the catalytic activity.[66] It is doubtful whether further engineering of sulfided molybdenum catalysts can provide the ultralow sulfur levels required to satisfy future regulatory limits. Alternatively, metal phosphides such as Co_2P, CoP, Ni_2P, MoP and WP have been found to be active catalysts for hydrodesulfurization processes, attributed in part to the isotropic distribution of metal sites on the surface resulting in improved catalytic activity. Among binary phosphides studied, Ni_2P supported on silica has shown the best performance and good resistance to sulfur poisoning and can even out-perform sulfided molybdenum under optimized conditions and when site activity is normalized.[36]

While binary phases of phosphides have been actively studied for hydro-treating, only very recently have researchers extended studies to ternary phosphides with the aim of obtaining synergistic effects. It is expected that the interaction of the two metals in the structure will enhance the activity of ternary materials due to structural or electronic effects; however, this depends strongly on the metal and composition.[69, 71, 72]

Previously reported catalytic studies for binary and ternary phosphides employed the traditional temperature programmed reduction (TPR) method to prepare the materials. Typically, the TPR method involves deposition of metal and phosphorous precursors onto a support (silica) followed by reduction to form the supported phosphide catalyst. This process yields samples with polydisperse particle sizes, precluding a detailed understanding of how active site density and quality impact activity and mechanism. Thus, to evaluate both size and composition effects synthetic methods that enable phase-pure, narrow polydispersity materials to be produced are

needed. Solution-phase arrested precipitation reactions enable excellent control of size, shape and composition in the formation of discrete nanoparticles.[15, 16, 20, 22, 97]

Additionally, as a solution to the anticipated energy crisis and environmental issues caused by burning of fossil fuels, production of renewable energy by water splitting is an area of considerable interest.[77-79] The electrocatalytic water splitting process requires an efficient catalyst to reduce the overpotential needed for the oxygen evolution reaction (OER) step. Ruthenium and iridium metal oxides are well known OER catalysts, but the scarcity and cost of these metals pose limitations to using these as industrial catalysts. Approaches to overcome these challenges include finding a catalyst comprising Earth-abundant metals only or diluting the noble metals with a relatively inexpensive, but comparatively active, second metal. Recently metal phosphides have emerged as effective electrocatalysts in OER but such studies have not evaluated the noble metal phosphides that are most active for OER: Ru and Ir.[63, 94, 95, 98, 99]

The dissertation research was focused on two major goals. The first goal was to develop synthetic methodologies to prepare bimetallic ternary phosphide nanoparticles ($Ni_{2-x}M_xP$; M=Co, Ru) via solution-phase arrested-precipitation reactions in order to obtain phase-pure, nearly monodisperse nanoparticles. The second goal was to evaluate the composition-dependent catalytic activity of these ternary phosphide nanoparticles and evaluate how active site density impacts activity.

To achieve the first goal, $Ni_{2-x}Co_xP$ and $Ni_{2-x}Ru_xP$ nanoparticles were prepared as crystalline phase-pure materials over a large composition range (for Co, $x \leq 1.7$ and for Ru, $x \leq 1$) with narrow size distributions and the structural and morphological changes taking place with compositional changes were evaluated. Moreover, synthetic levers were identified enabling control over the size

and morphology of $Ni_{2-x}Co_xP$ nanoparticles. The synthetic and characterization details of these ternary phosphide nanoparticles are discussed in Chapters 3 ($Ni_{2-x}Co_xP$) and 4 ($Ni_{2-x}Ru_xP$).

To achieve the second goal, we evaluated the hydrodesulfurization activity of $Ni_{2-x}M_xP$ (M=Co, Ru) nanoparticles and the OER catalytic activity of $Ni_{2-x}Ru_xP$ nanoparticles. As described in Chapter 5, dibenzothiophene (DBT) HDS catalytic activity was measured for Ni-rich compositions of $Ni_{2-x}Co_xP$ and, with probing the bond strengths of adsorbed CO by IR spectroscopy, a change in the electronic nature of the active sites with the incorporation of the second metal was assessed. Higher electron density on the Ni sites for Co-rich materials was revealed, which resulted in a higher turnover frequency for these materials even as we presume the total number of active sites has decreased, judging by the overall decrease in activity. Composition-dependent OER catalytic activity studies of $Ni_{2-x}Ru_xP$ nanoparticles are presented in Chapter 4. Ternary phases outperformed the binary end products and the best performance with respect to overpotential (0.34 V at 10 $mAcm^{-2}$, 1.0 M KOH) was at x=0.75. Preliminary HDS data for Ni-rich phases are presented in Chapter 5 and show that introduction of Ru decreases activity towards HDS of 4,6-DMDBT.

A summary of findings with respect to the solution-phase synthesis of ternary phosphide nanoparticles and their performance as HDS model catalysts and/or OER electrocatalysts along with the significance of the two-metal interaction for the performance of ternary phosphide nanocrystals, will be discussed as conclusions in Chapter 6. Additionally, future studies inspired by these findings will be presented.

CHAPTER 2 EXPERIMENTAL AND MATERIALS CHARACTERIZATION TECHNIQUES[1]

Transition metal phosphide nanoparticles were synthesized under inert conditions and these materials, along with nanoparticles encapsulated in mesoporous silica were characterized for phase, size, morphology and composition. This chapter describes all the materials and techniques used in the syntheses and the characterization methods, which include Powder X-Ray Diffraction (PXRD), Electron Microscopy (EM), Energy Dispersive Spectroscopy (EDS), Inductively Coupled Plasma-Mass Spectroscopy (ICP-MS), X-ray photoelectron spectroscopy (XPS), surface area and porosimetry.

2.1 Materials

Nickel acetylacetonate ($Ni(acac)_2$, Alfa Aesar, 95%), cobalt(II) acetylacetonate ($Co(acac)_2$, Sigma-Aldrich, 99%), n-octyl ether (TCI America, 95%), oleylamine (TCI America, >50%), tri-n-octylphosphine (TOP, STREM Chemicals, 97%), tetraethylorthosilicate (TEOS, ACROS), ruthenium chloride hydrate (Pressure Chemicals, 40-43% metal), Nafion (5%, LQ-1105, Ion Power), sodium hydroxide (Aldrich, ≥98%), chloroform (Fisher Scientific), hexanes (technical grade, Fisher), methanol and ethanol (200 proof) (Decon laboratories). All chemicals were used as received.

[1] Portions of the text in this chapter were reprinted or adapted with permission from: Chem. Mater. 2015, 27, 4349-4357 and Surface Science 2016, 648, 126-135

2.2 Experimental techniques

2.2.1 Glove Box

Glove box technique provide the environment to handle air-sensitive chemicals and reactions under inert conditions. In metal phosphide syntheses, TOP is handled inside the glove box due to its air sensitivity. The box is maintained under an Ar environment and, a photohelic pressure gauge is used to maintain positive pressure inside the box. A copper catalyst along with molecular sieves is attached to the box and the Ar gas is continuously flowing through the catalyst to minimize the amount of oxygen and water contamination. With time, as the catalyst is oxidized, an occasional regeneration of the catalyst is required to maintain the optimum quality. A glovebox model HE 493 purchased from Vacuum Atmospheres is used in this dissertation research.

2.2.2 Schlenk line techniques

All the solution phase syntheses of metal phosphides in this dissertation research are carried out using standard Schlenk line techniques. A Schlenk line consists of two manifolds, one is connected to the vacuum pump through a cold trap to create a vacuum and other is connected to inert gas (Ar, N_2, etc) supply. This enables an inert environment to carry out air sensitive reactions.

2.3 Characterization techniques

2.3.1 Powder x-ray diffraction (PXRD)

PXRD is a principle technique used to characterize materials in solid state chemistry. This technique can provide information regarding the structure of a material including phase, composition and crystallinity. As this method is based on diffraction of radiation by atoms, each material exhibits a fingerprint pattern in the PXRD. The wavelength of X-rays is ca. 1 Å (10^{-10} m), which is similar to the inter-atomic spacing within a lattice. Thus, the lattice acts as a diffraction grating for the radiation.

Figure 2.1 shows the basic set up involved in the generation of X-ray radiation.[100] The X-ray tube consists of a (i) anode (target to produce X-rays) (ii) cathode (electron generating material), and (iii) evacuated chamber (providing the pathway for highly accelerated electrons). The commonly used cathode material for electron generation is W metal and when this material is heated with a filament current, it produces electrons. These electrons are accelerated by applying a high voltage (30-60 kV) and strike the metal target (anode). The electrons have sufficient energy to excite the core electrons in the metal target which will lead to generation of X-ray radiation. The radiation passes through a Be window, which is largely transparent to radiation due to its low atomic number. During the collision with the anode, the kinetic energy of the accelerated electrons converts to heat and this leads to heating of the anode, necessitating a continuous flow water cooling system. Some PXRD machines are equipped with a continuously rotating, disk shape anode and this set up increases the efficiency of X-ray generation by minimizing the produced heat.

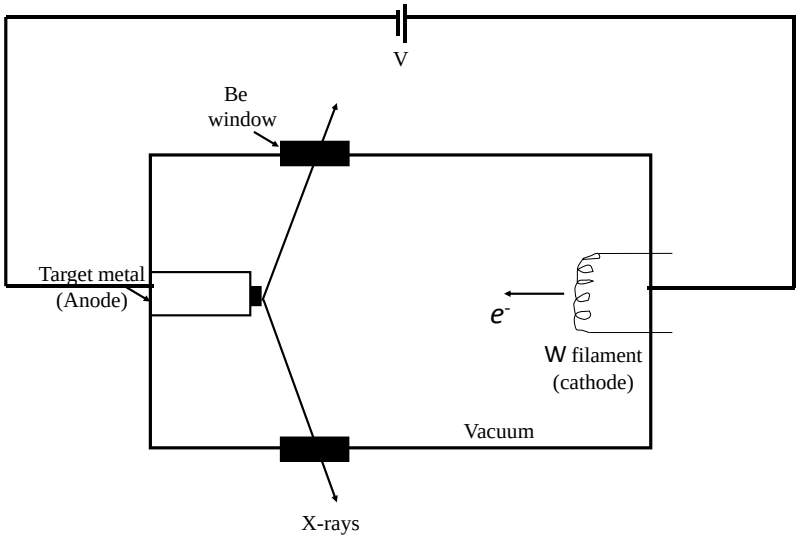

Figure 2.1. Schematic diagram of an X-ray tube with main components (adapted from West)[105]

Figure 2.2 illustrates the typical process involved in the production of X-rays with the commonly used metal anode Cu.[100] When the electrons strike the Cu metal target, a 1s electron is ionized creating a vacant hole in the K shell. To fill this vacancy, electrons in higher energy levels (2p or 3p) transit to the vacant level and during this transition energy is released as X-ray radiation. Typically, an X-ray spectrum consist of two major parts. One part is a broad spectrum (white radiation) which is produced by the deceleration of electrons due to the collision with anode, and other part consists of discrete spectral lines with monochromatic radiation. These lines include Kα ($2p \rightarrow 1s$) and Kβ ($3p \rightarrow 1s$) transitions. Typically, as the Kα line is higher in intensity it is mainly used for diffraction experiments. As the 2p level has two spin states ($2p_{1/2}$ and $2p_{3/2}$) with slightly different energies, the Kα line consists of doublet known as $K\alpha_1$ (1.54051 Å) and $K\alpha_2$ (1.54433 Å).

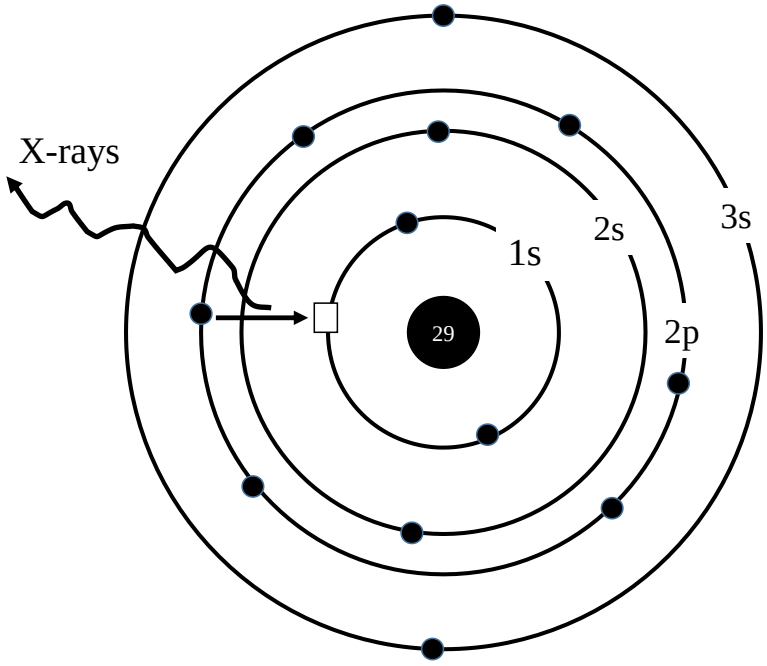

Figure 2.2. Illustration of X-ray generation process with the Cu metal as the anode (adapted from West)[105]

For X-ray experiments it is important to have monochromatic radiation. Hence, to remove Kβ radiation a filter can be used. Typically, this filter is a metal one or two atomic numbers lower than the anode metal, and for Cu the most common filter used is Ni metal.

The X-ray fluorescence is an issue that can interfere with the quality of the PXRD spectra. This is caused by the knocking of an inner shell electron in the sample followed by dropping of an outer shell electron to fill the vacancy by releasing energy as X-ray radiation. In this case, the sample itself acts as an X-ray source. The significance of interference depends on the anode material and the type of material analyzed. For an instance, when collecting data using a Cu anode (wavelength 1.5418 Å), for Co and Ni materials in which the ionization potentials of the 1s electron are 1.6081 and 1.4880 Å, respectively, the Cu radiation can ionize the 1s electron in cobalt but not in nickel.[101] To minimize the interference from this X-ray fluorescence, the anode material can be varied depending on the analyte. Table 2.1 shows the anode materials available with their radiation wavelengths and suitable filters.[102] The wavelength of X-ray released by each metal is related to the atomic number (Z) given by Moseley's law (Equation 2.1).[101]

$$f^{1/2} = \left(\frac{c}{\lambda}\right)^{1/2} \alpha Z \qquad (2.1)$$

f = frequency of Kα line

Table 2.1. Anode materials with different wavelengths of X-rays produced and the suitable filters to eliminate Kβ radiation (adapted from Pecharsky)[107]

Metal	Wavelength (Å)			β Filter
	$K\alpha_1$	$K\alpha_2$	Kβ	
Cr	2.28975(3)	2.29365(2)	2.08491(3)	V
Fe	1.93608(1)	1.94002(1)	1.75664(3)	Mn
Co	1.78900(1)	1.79289(1)	1.62082(3)	Fe
Cu	1.540593(5)	1.54441(2)	1.39225(1)	Ni
Mo	0.709317(4)	0.71361(1)	0.63230(1)	Nb

The repetitive arrangement of atoms in a crystal can be compared to an optical grating and as the atomic distance in a crystal is similar to the X-ray wavelength, diffraction from atoms is similar to optical diffraction. Bragg's law can be used to illustrate the diffraction taking place in a crystal. As shown in Figure 2.3, two waves a and b interact with two atoms present in two adjacent A and B crystal planes. The distance between the two planes is denoted as d_{hkl}. The first incident beam (a) with an angle of Θ is reflected from the first plane at the same angle Θ while the second beam (b) passes through the first plane and is reflected by the second plane. The difference in distance traveled by the two waves (xyz) can be expressed as in Equation 2.2.[100]

$$xyz = 2d\sin\Theta \qquad (2.2)$$

Bragg's law expresses a relationship between the path length difference and the wavelength of radiation (Equation 2.3). Accordingly, if the difference is a multiple integer of the wavelength, constructive interference between the two waves takes place. The angle which satisfies this condition is known as Bragg's angle and any wave which has a different angle undergoes destructive interference.

$$n\lambda = 2d\sin\Theta \ (n=1,2.3,\ldots\ldots n) \qquad (2.3)$$

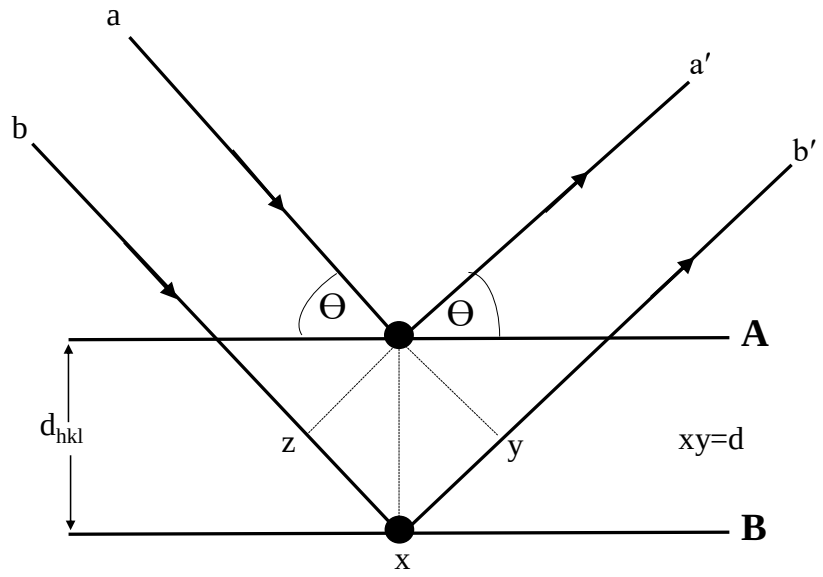

Figure 2.3. Illustration of Bragg's law (adapted from West)[105]

Figure 2.4 illustrates X-ray diffraction taking place from finely powdered samples. As there are multiple orientations fulfilling Bragg's angle, constructive diffraction takes place in multiple directions. This diffracted radiation can be collected by a photographic film, CCD camera or a movable detector.

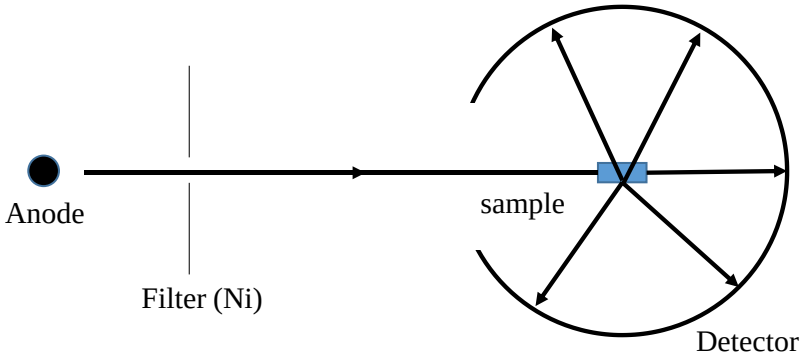

Figure 2.4. Illustration of diffraction from a powdered sample (adapted from West)[105]

The intensity of the peaks in the PXRD pattern is critical determining the structural properties of the material. During the diffraction process from an atom, the electric field of the X-ray interacts with the electrons in the atom and scattering takes place in different directions. The scattered

intensity is a sum of the individual intensities from all electrons and can be defined as the form factor (f). The form factor is a function of the atomic number and, as the scattering angle increases, this value goes down. The form factor directly correlates to the structure factor (F_{hkl}), a parameter that governs the overall peak intensity in a PXRD pattern which can be defined as[103]

$$F_{hkl}= \sum_j f_j \exp\{-i2\pi(hx_j+ky_j+lz_j) \quad (2.4)$$

f_j = form factor for j^{th} atom

h,k,l = miller indices for the reflection

x_j,y_j,z_j= fractional coordinates for the j^{th} atom

The PXRD pattern can also be used to interpret the growth direction and size of the crystallites present in the sample. The breadth of the peaks is a measure of the crystallite size and typically for nanoparticles broad peaks are observed due to the fact that there are fewer crystalline planes present, limiting the destructive interference for angles near the Bragg angle. Additionally, for anisotropic materials, as there is a preferred direction of growth, the peaks corresponding to that growth direction are narrow and more intense whereas those corresponding to short axes are broader, again reflecting the number of diffracting planes. The breadth of the peaks can be used to estimate the crystallite size (t) using the Scherrer equation (Equation 2.5).

$$t= \frac{k\lambda}{\beta Cos\theta} \quad (2.5)$$

λ= wavelength of X-ray

k= shape factor (typically 0.9 for spherical particles)

β= Full width half maximum of the peak (FWHM)

Θ=Bragg angle

In this dissertation research, powder X-ray diffraction (PXRD) data were collected on a Rigaku RU 200B rotating anode diffractometer with Cu Kα radiation (0.154 nm) operated at 40kV,

150mA with a step size of 0.02° for $Ni_{2-x}Co_xP$ samples and a Bruker D_2 Phaser X-ray diffractometer with Cu Kα radiation (0.154 nm) operated at 30 kV, 10 mA with a step size of 0.02° was used for Ru_xP_y and $Ni_{2-x}Ru_xP$ samples. Samples were deposited on a zero background quartz holder using minimal grease and data were collected over the 2Θ range 30-80°. Silicon was used as an internal standard. The patterns were compared to powder diffraction files (PDFs) from the ICDD database for phase identification. The collected patterns were analyzed using Jade 5.0 software for crystallite size (using the Scherrer equation).

2.3.2 Transmission electron microscopy (TEM)

Microscopy techniques involve the magnification of materials. As shown in Equation 2.6, the resolution (δ) of a microscope depends on the wavelength of the radiation(λ).[104] Optical microscopes use visible light, which limit the resulting resolution to a few hundreds of nanometers, which is insufficient for imaging samples on the nanoscale.

$$\delta=\frac{0.61\lambda}{\mu Sin\beta} \qquad (2.6)$$

μ= refractive index of the viewing medium

β= semi-angle of collection of the magnifying lens

$$\lambda=\frac{h}{(2m_0eV)^{\frac{1}{2}}} \qquad (2.7)$$

h= Planck's constant

V= accelerating voltage

m_0= mass of electron

eV= kinetic energy

In 1925 de Broglie demonstrated that electrons have wave-like properties, opening the door to the invention of electron microscopy methods, which are capable of imaging nanoscale objects. According to Equation 2.6, the small wavelength of electrons could provide very high resolution in material characterization (electron microscope operated at 100 kV voltage, resolution is about 0.24 nm and optical microscope for green light (550 nm) resolution is 300 nm). In nanotechnology, which deals with sizes in the nano regime, electron microcopy is a very versatile tool to analyze size, morphology, composition and crystallinity of materials. Figure 2.5 illustrates different processes taking place when a sample is bombarded with a beam of electrons.[104] Among these processes, the transmitted electrons are the basis for transmission electron microscopy (TEM), the backscattered electrons are used in scanning electron microcopy (SEM) and the generated X-rays can be used for energy dispersive spectroscopy (EDS). Two techniques related to this dissertation research, TEM and EDS will be discussed in detail in this chapter.

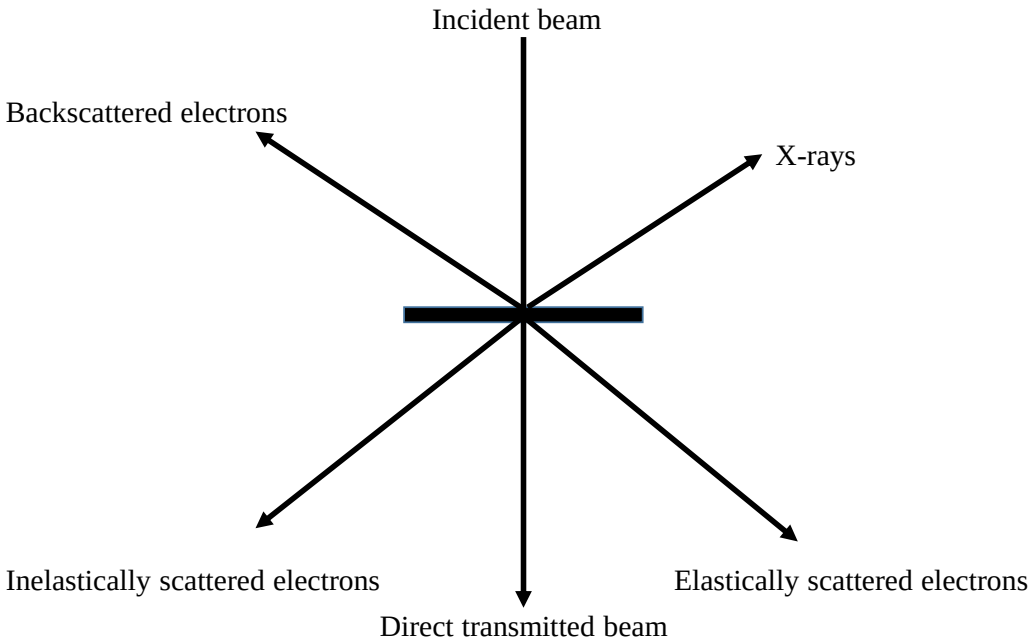

Figure 2.5. Different processes undergone by bombarded electrons interacting with a specimen (adapted from Williams)[109]

As mentioned before, the resolution of the analysis depends on wavelength of the radiation. Hence, lower wavelengths will result in better resolution. Equation 2.7 can be constructed using de Broglie wavelength (λ) and kinetic energy (eV) of electrons, and according to this equation, the wavelength directly correlates to the voltage applied to the cathode.[104] Typically, TEM is operated at high voltage (100kV-400 kV) to obtain lower wavelengths (at 100 kV, λ=3.88 pm and at 400 kV, λ=1.94 pm) and to minimize the scattering of these high energy electrons, the electron pathway is in a high vacuum environment. To control the direction of electrons, electromagnetic lenses are used, which perform a similar function to the optical lenses used in optical microscopy.

Figure 2.6 shows a schematic diagram of a typical TEM instrument with basic components.[105] The first component consists of the electron gun to produce electrons. There are two types of electron guns. Thermionic guns produce electrons by the heating of the cathode (W and LaB_6) whereas field-emission guns produce electrons with the application of a voltage. The produced electrons are passed through condenser lenses in order control the intensity and angular aperture of the beam before interacting with the specimen. Objective lenses focus the beam coming through the specimen and the intermediate projective lenses expand the beam on the viewing screen. In TEM, imaging is based on the transmitted radiation, which depends on the atomic number of the elements and the thickness of the sample. So it is important for the sample to be uniformly deposited and sufficiently thin (<1000 Å) to obtain high quality images.

TEM has two basic imaging modes. As shown in Figure 2.7(a), in the bright field mode the diffracted beams are blocked by an objective aperture and only the direct beam reaches the screen. In these images, the material appears dark in a bright background. In the dark field mode (Figure 2.7(b)) only the diffracted beams reach the screen and the direct beam is blocked. In these images the crystalline region of the material appears bright in a dark background.[104]

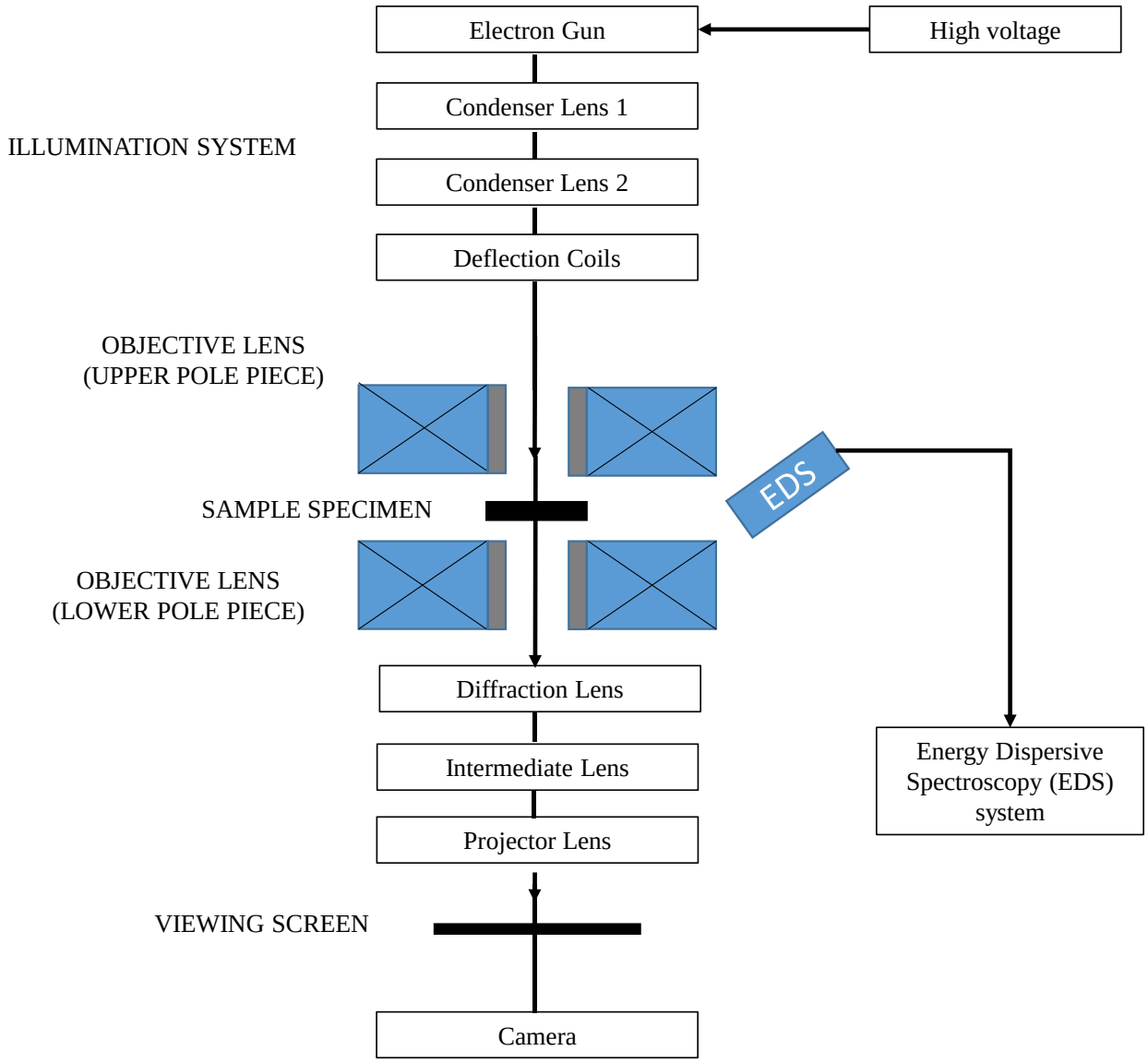

Figure 2.6. Schematic diagram of a TEM instrument with basic components (adapted from Fultz)[110]

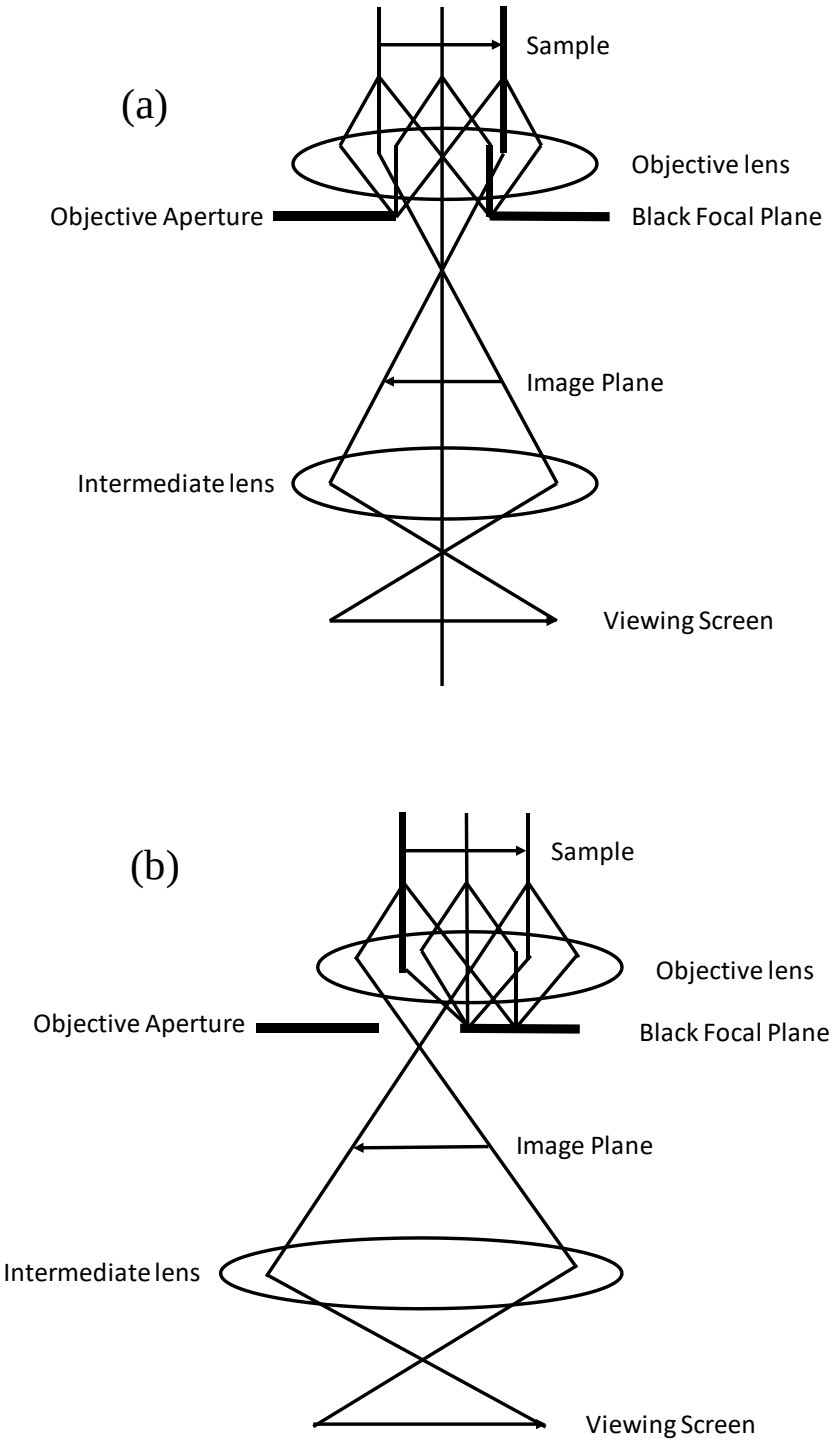

Figure 2.7. Basic imaging modes of TEM (a) bright Field mode (b) dark field mode (adapted from Williams)[109]

Other than providing information on morphology and size, TEM can provide information on the crystallinity of the sample by selected area electron diffraction (SAED). To achieve this, it has to be operated in diffraction mode. In this mode a second aperture, called the intermediate aperture, is placed in the image plane of the objective lens in order to select only a selected region of the specimen and the direct beam is blocked so only diffracted beams are obtained (Figure 2.8).[105] The resulting image appears as a set of dots in a ring for single crystalline samples or a continuous set of rings for polycrystalline samples. The distance between two opposite positions of a ring across the center can be used to calculate the d-spacing of the crystal.

In this dissertation research TEM images were collected with a JEOL 2010 electron microscope operating at a voltage of 200 kV. Bright field images were captured by Amtv 600 software. TEM specimens were prepared by dispersion of nanoparticles in chloroform and depositing a drop of solution on a formvar carbon-coated 200 mesh Cu grid, followed by drying in air.

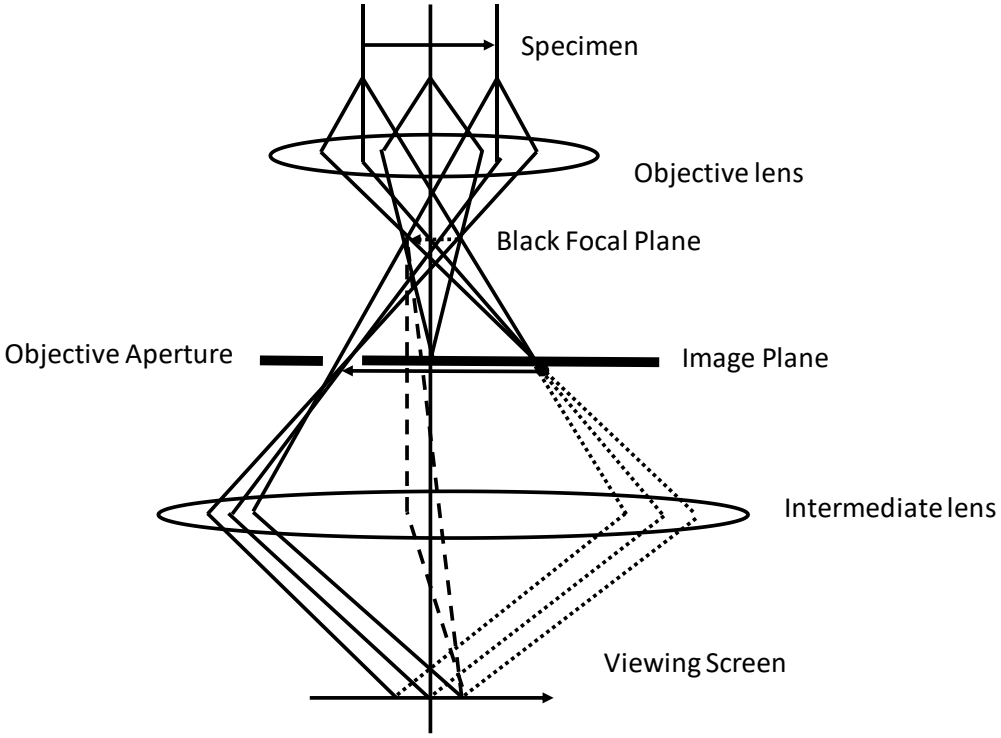

Figure 2.8. SAED mode of TEM (adapted from Fultz)[110]

2.3.3 Energy dispersive spectroscopy (EDS)

As shown Figure 2.5 when the high energy electrons collide with the specimen it can produce X-rays. Generation of X-rays is taking place by the same mechanism explained in the PXRD section 2.3.1. The produced X-ray energy is characteristic of the elements present in the sample. Hence, the intensity and energy of the X-rays can be used as a semi quantitative method to identify elements quantify the percentage of each element present in a sample. EDS is commonly coupled with another technique such as TEM and SEM. Figure 2.9 illustrates the basic components involved in an EDS system.[104]

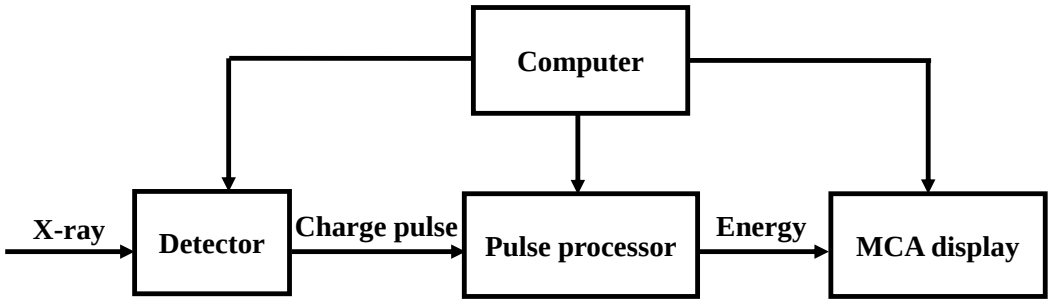

Figure 2.9. Basic components of an EDS system (adapted from Williams)[109]

Once X-rays reach the detector, typically a Si crystal cooled to liquid N_2 temperature, the high energy of the X-ray generates electron-hole pairs in the detector and these pairs subsequently constitute a charge pulse. Next, this pulse is converted to a voltage by the pulse processor and the voltage is further amplified by amplifiers. The amplified voltage signal is sent to a computer and the intensity (X-ray counts) against energy is plotted as the output. EDS is a semi quantitative method and it is important to choose non overlapping peaks for reasonable quantification.

In this dissertation, EDS data were collected using an EDS detector (EDAX Inc) coupled to the JEOL 2010 TEM instrument. Quantification of elements was carried out using EDAX Genesis software 1.0 version. The peak positions in the EDS were calibrated using Al (1.486 keV) and Cu (8.040 keV) metals.

2.3.4 Scanning transmission electron microscopy (STEM)

STEM is a combination of TEM and SEM (collecting transmitted electrons while scanning across the sample), serving as a novel and versatile technique for nanomaterial characterization. In this method, a finely focused thin beam of electrons is scanned through the sample in a raster pattern rather than bombarding with a parallel beams of electrons as is done in conventional TEM. Typical STEM is equipped with different detectors to probe different processes taking place during the scanning process. Bright field and dark field images can be captured by collecting the direct

beam electrons and the scattered beam electrons, respectively, as in TEM process. Characteristic X-rays produced by the elements can be probed by EDS detector and these data can be used for elemental mapping. In STEM the high angle annular dark field (HAADF) detector can probe the electrons scattered by elements in a larger angle resulting a stronger signal. Since the scattering of electrons by atoms is proportional to the atomic number (Z), atoms with higher Z appear brighter. Therefore, this mode is known as Z-contrast imaging.[106] Overall STEM provides great deal of spatial information on a finer scale than is achievable in conventional TEM.

In the dissertation work, STEM images were taken using a high angle annular dark field detector (HAADF) on a FEI Titan 80-200 scanning transmission electron microscope (STEM) with ChemiSTEM Technology operated at 200 kV. The so-called "Super X" EDS system, which includes 4 windowless silicon-drift detectors (SDD) around the specimen (made by Bruker Corporation), provides a solid angle of more than 0.9 srad, and the X-ray signal is usually more than 1000 cps at a magnification of about 640,000x.

2.3.5 Surface area and porosimetry

Determination of surface area and pore size is critical for porous materials, especially for catalytic applications. Surface area can be determined by quantifying the adsorption of a gas on a porous surface. Depending on the interaction of the surface (adsorbent) and gas (adsorbate) adsorption can be categorized into two parts. Gases adsorb to the surface via weak forces (van der Waals forces) called physisorption and this process is reversible. In contrast, chemisorption is caused by chemical bond formation between the adsorbent and adsorbate. The chemisorption interaction is strong and irreversible. During the analysis, the amount of gas adsorbed to the surface as a function of pressure at constant temperature is quantified. The amount adsorbed depends on many factors such as sample mass, temperature and purity of the adsorbent surface. Thus, it is very

important to get rid of any impurities such as moisture and atmospheric vapors from the surface of the analyte. This is achieved by evacuating or heating the sample under a flow of an inert gas. The optimum temperature has to be chosen to avoid transformation within the sample while enabling desorption of physisorbed species. Once the surface cleaning is done, the sample is weighed and then subjected to the analysis. As the adsorption depends on the temperature, the analysis is carried out isothermally at cryogenic temperatures, usually liquid N_2 (77.3K). An isotherm is constructed by plotting the volume of gas adsorbed against the relative pressure (P/P_0), where P is gas pressure and P_0 is the vapor pressure. In a typical experiment, both adsorption and desorption isotherms are included in order to extract more information, especially with respect to the pore structure. Depending on size, pores can be divided into three categories. The smallest, micropores (<2 nm), fill with the gas (adsorbate) first at low pressures followed by filling of larger mesopores (2-50 nm) and macropores (>50 nm) at high pressures.[107]

As shown in Figure 2.11 isotherms can be categorized into six types depending on shape.[107] Type I is characteristics of adsorbents with very small micropores (<2 nm) showing a saturation of adsorption at relatively low pressure. Type II and IV represent either relatively larger pores (mesopore 2-50 nm) or nonporous materials sharing the same type of adsorption curves but different desorption curves. Type III and V are typical for materials which have stronger interactions between the adsorbates themselves than the interactions between the adsorbent and adsorbate. Types III and V isotherms are not very useful for surface area analysis. Type VI curves are characteristic of a nonporous material with a uniform surface. Some of the above isotherms exhibit with a hysteresis loop, which is caused by the capillary condensation of adsorbate at high pressures.

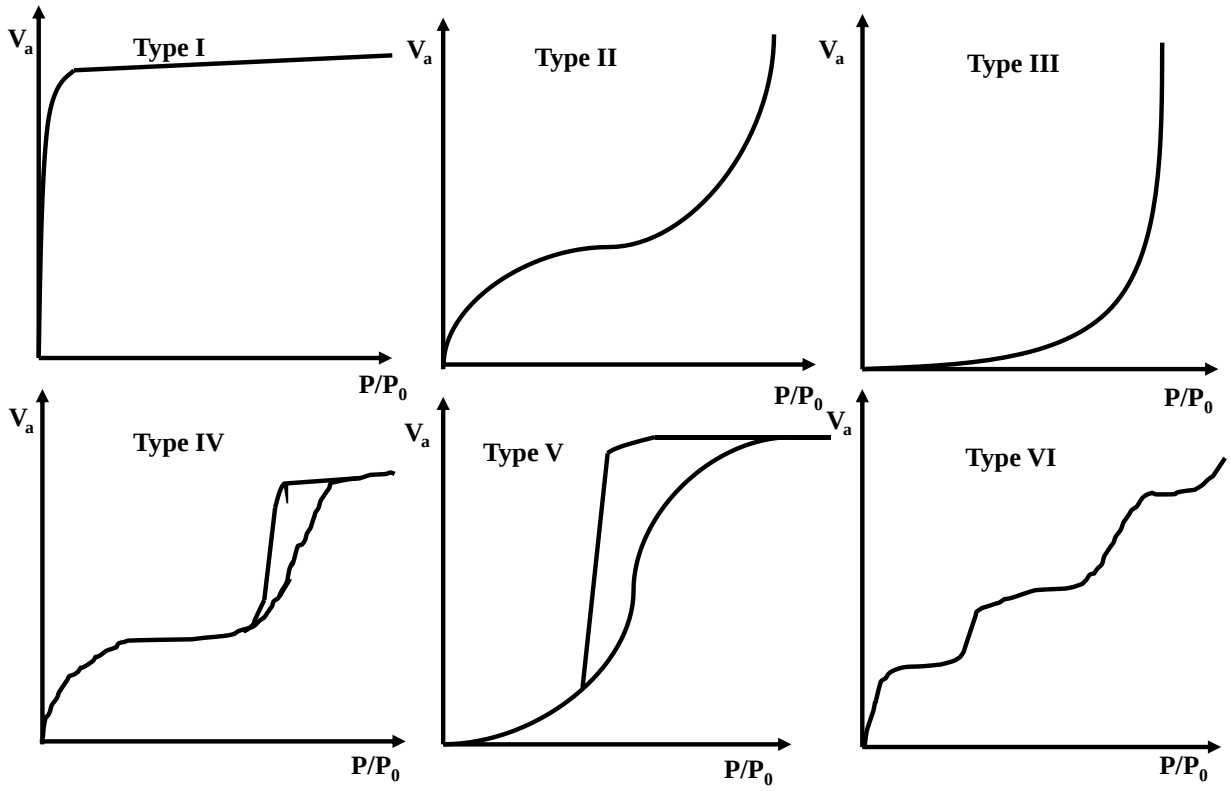

Figure 2.10. The basic adsorption types (adapted from Webb)[112]

The adsorption of gas to a surface can be treated with different theories. The Langmuir adsorption model was developed in 1916 by Irving Langmuir and this model is more relevant for chemisorption as it assumes a monolayer adsorption.

Equation 2.8 shows the relationship of volume of gas (V_a) adsorbed with pressure (P) for the Langmuir model. V_m is the volume of gas adsorbed to form the monolayer and b is an empirical constant.[107]

$$V_a = \frac{V_m bP}{1+bP} \qquad (2.8)$$

Equation 2.8 can be rearranged to obtain a linear form as in Equation 2.9. According to this equation when P/Va is plotted against P a linear graph should be obtained and from the slope and

intercept Vm and b can be evaluated. From these values the specific surface area (s) of the adsorbent could be calculated by Equation 2.10.[107]

$$\frac{P}{V_a} = \frac{1}{V_m b} + \frac{P}{V_m} \quad (2.9)$$

$$S = \frac{V_m \sigma N_A}{m V_0} \quad (2.10)$$

σ = area of surface occupied by a single adsorbed gas molecule
N_A= Avogadro number
m= mass of the sample
V_o= molar volume of gas

In order to treat for multi-layer adsorption Brunauer, Emmett and Teller introduced the BET theory in 1938. This theory suggests there is infinite number of layers adsorbed on the surface of adsorbent and there is no interaction between each layer. Equation 2.11 was introduced to explain the BET theory, where C is a constant and P_0 is the saturation pressure of the gas.

$$\frac{P}{V_a(P_0 - P)} = \frac{1}{V_m C} + \frac{C-1}{V_m C}\left(\frac{P}{P_o}\right) \quad (2.11)$$

The pore size distribution, pore volume and average pore diameter of the material can be calculated by the BJH method developed by Barrett, Joyner and Halenda. This method is based on the Kelvin equation given in Equation 2.12 and it is based on the assumption the pores are cylindrical in shape. The amount of gas used or released to fill or empty the pores in each step during adsorption and desorption processes, respectively, are used to solve the equation. The basic geometric equations for a cylinder can be further used to calculate other parameters such as pore length and pore area.[107]

$$\ln\left[\frac{P^*}{P_0}\right] = -\left[\frac{2\gamma v Cos\Theta}{RTr_m}\right] \qquad (2.12)$$

P^* = critical condensation pressure

Γ = liquid surface tension

V = molar volume of condensed adsorptive

Θ = contact angle between solid and condensed phase

r_m = mean radius of curvature of the liquid meniscu

In the dissertation work surface area and pore size distributions for encapsulated silica samples were collected using a Micromeritics Tristar II surface area/porosimeter. All samples were degassed for 16 h at 423 K under N_2 flow before the analysis. Surface areas were calculated based on the Brunauer–Emmett-Teller (BET) multimolecular adsorption method and pore size distributions were obtained by the Barrett- Joyner- Halenda (BJH) method.

2.3.6 X-ray photoelectron spectroscopy (XPS)

XPS is a surface sensitive technique which can provide information on the oxidation state, chemical environment and composition of elements on the surface of a material. This technique is based on the principle of the photoelectron effect, which uses X-rays as the electron exciting source. Generally X-rays produced by Mg (Kα=1253.6 eV) and Al (Kα=1486.6 eV) are used in this experiment. Figure 2.13 illustrates the photoelectron effect; X-rays interact with a core level electron, photon energy is transferred to the electron, followed by ejection of the electron with kinetic energy.[108] As the photon energy is known, by measuring the kinetic energy (E_k) of the emitted electron, the binding energy of electron (E_b) can be calculated according to the Equation 2.13. In an element, as the binding energy of an electron in a particular shell is unique, it can be used to identify the elements and relative concentration.

$$E_b = h\nu - E_k - \phi_s \quad (2.13)$$

ν = frequency of X-ray

ϕ_s = work function of the instrument

In this dissertation research X-ray photoelectron spectroscopy (XPS) analyses were carried out using a Surface Science Instruments S-probe spectrometer. This instrument has a monochromatized Al Kα X-ray source and a low energy electron flood gun for charge neutralization of non-conducting samples. The samples were dusted onto double-sided tape and run as insulators. The X-ray spot size for these acquisitions was approximately 800 μm and the pressure in the analytical chamber during spectral acquisition was less than 5 x 10^{-9} Torr. The pass energy for survey spectra (to calculate composition) was 150 eV and the pass energy for high resolution scans was 50 eV. The binding energy scales of the high-resolution spectra were calibrated by assigning the most intense C1s high-resolution peak a binding energy of 285.0 eV.

2.3.7 Infrared spectroscopy

Infrared (IR) spectroscopy can be used as an important tool to probe vibrations in a molecule. This technique deals with the infrared region of the electromagnetic radiation. The vibrational frequency of a bond depends on the mode of vibration, bond strength and mass of atoms in the bond. For a vibration to be IR active the dipole moment should change with the vibration. This technique commonly used in organic spectroscopy to identify the functional groups. Typically, IR spectra are collected 4000-400 cm^{-1}. Experimental details on IR spectroscopy used in this dissertation research is given in Chapter 5.

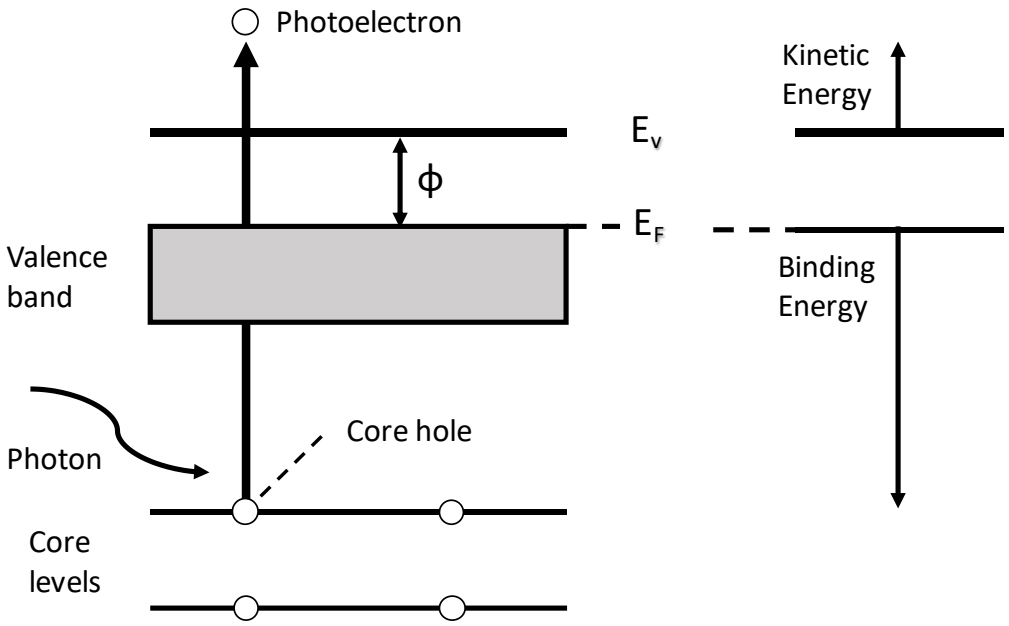

Figure 2.11. Schematic diagram illustrating the photoemission process in XPS (adapted from Wagner)[113]

2.3.8 Carbon monoxide (CO) pulse chemisorption analysis

A pulse chemisorption analysis determines active surface area, percent metal dispersion, and active metal particle size by measuring the consumption of a gas (CO) input as pulses. The consumption can be monitored by a thermal conductivity detector. Typically, in the first few pulses the gas reacts with the available active sites and a reduction in the output signal can be observed. Once all active sites react with the gas, no change in the output signal will be observed for successive pulses. By measuring the total amount of gas consumed in each pulse total chemisorption capacity can be calculated. The experimental details used to calculate chemisorption capacities of encapsulated catalyst samples are given in Chapter 5.

The XPS, IR and CO chemisorption capacity measurements were conducted by the research group of Mark Bussell at Western Washington University.

2.3.9 Inductively Coupled Plasma-Mass Spectrometry (ICP-MS)

ICP-MS is an analytical technique used for elemental analysis consisting of an ICP coupled to a mass spectrometer. The high sensitivity for wide range of elements is the key advantage of this instrument over other techniques. In the operation of ICP-MS, Ar gas flows inside the channel of an ICP torch that is connected to a radio frequency generator. When the power is supplied, an oscillating magnetic and electric field is generated at the end of the torch. When a spark is applied to the flowing Ar, the gas is ionized and forms Ar ions. These ions are trapped inside the oscillating fields and collide with other Ar atoms creating a plasma. In the analysis, the sample is introduced to the ICP torch as an aerosol, converting the sample to gaseous atoms. These atoms are further ionized at the end of plasma. The generated ions are next passed through the mass spectrometer and they are separated based on the mass-to-charge ratio before reaching the detector.

In the dissertation research inductively coupled plasma-mass spectrometry (ICP-MS) measurements were carried out on an Agilent 7700 ICP-MS instrument to determine concentrations of elements. In this process, about 2 mg of dried sample was digested in 5 mL of concentrated nitric acid over a few days and then diluted with nano pure water. The instrument was calibrated using a series of standards over the desired concentration range.

CHAPTER 3 SIMULTANEOUS CONTROL OF COMPOSITION, SIZE AND MORPHOLOGY IN DISCRETE $Ni_{2-x}Co_xP$ NANOPARTICLES[2]

3.1 Introduction

Transition metal phosphides have emerged as efficient catalysts in different applications as discussed in Chapter 1. While binary phases have been extensively studied, only recently have researchers started to explore opportunities for synergism afforded by ternary phases. Ternary phosphides of formula $Ni_{2-x}Co_xP$ are of particular interest as they have shown improved HDS activity relative to the best of the binary phases (Ni_2P) at low concentrations of Co ($x \leq 0.1$) for materials prepared by the TPR method.[71] Likewise Zhang and co-workers observed $Ni_{2-x}Co_xP$ to be an active catalyst for hydrazine decomposition, with the highest activity observed for the $Ni_{1.0}Co_{1.0}P_{1.5}$ composition.[109] While these studies point to the promise of these phases as active catalysts with a range of potential applications, the lack of synthetic methodologies enabling nanoparticle formation with independent tuning of composition and size impedes the development of a comprehensive model for their function. To our knowledge, reports of discrete $Ni_{2-x}Co_xP$ nanoparticles are limited to a 2014 report by Peng and co-workers on the synthesis of $Co_{1.33}Ni_{0.67}P$ nanorods.[110] This material proved to be active for HER, underscoring the need for a rational synthetic approach that would enable tuning of catalytic function in ternary phosphide nanoparticles by independently addressing size, shape and composition.

This chapter discusses a synthetic protocol developed to prepare different compositions of $Ni_{2-x}Co_xP$ nanoparticles ($x \leq 1.7$) as nearly monodisperse particles with excellent control over composition. Additionally, synthetic levers were identified to control the morphology and size of these nanoparticles using Ni:Co=1:1 as a representative composition.

[2] Portions of the text in this chapter were reprinted or adapted with permission from: Chem. Mater. 2015, 27, 4349-4357

I performed the synthesis of nanoparticles and some characterizations (PXRD, TEM, EDS) at Wayne State University. X-ray photoelectron spectroscopy, Rietveld refinement and interpretation of data were carried out by Prof. Mark E Bussell's group at Western Washington University. Elemental mapping data and line scanning for ternary phosphide particles were collected by Dr.Yi Liu at the electron microscopy facility at Oregon State University.

3.2 Experimental

All materials used in the synthesis of $Ni_{2-x}Co_xP$ nanoparticles are given in Chapter 2.

3.2.1 Synthesis of $Ni_{2-x}Co_xP$ nanoparticles ($0 \leq x \leq 2$)

All reactions were carried out under argon atmosphere using standard Schlenk line techniques. In a typical synthesis, the corresponding amounts (overall 2.0 mmol) of the two metal precursors ($Ni(acac)_2$, $Co(acac)_2$) were combined with 5.0 mL (8.0 mmol) of oleylamine (coordinating ligand), 10.0 mL of octyl ether (solvent) and 4.0 mL (10.0 mmol) of trioctylphosphine (TOP, P source) in a Schlenk flask. The mixture was degassed at 110 °C for 20 min to remove any moisture or oxygen, followed by purging with argon for 20 min at this temperature. The temperature was then increased to 230°C and maintained for 90 min. Next, the temperature was set to 350 °C; as soon as the temperature started increasing, an extra 6 mL aliquot of TOP was injected, followed by heating for 4.5 h at 350 °C. The black product was isolated by precipitation with ethanol. The product was dispersed again in chloroform, sonicated for 5-10 min and reprecipitated with ethanol. This sonication and precipitation process was carried out at least three times.

Scheme 3.1. Reaction protocols for the synthesis of $Ni_{2-x}Co_xP$ nanoparticles

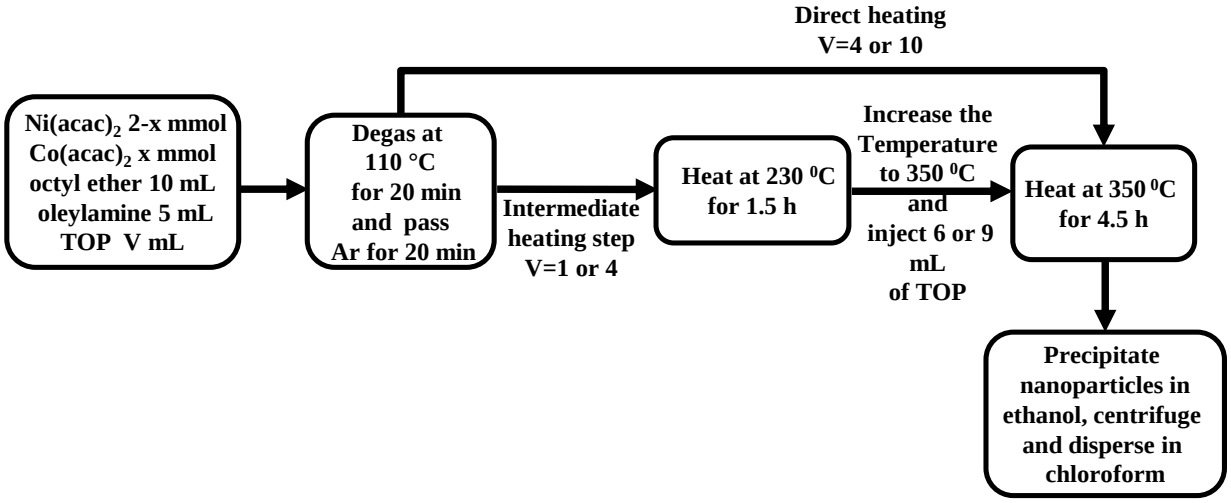

3.3 Results and Discussion

The protocol developed to synthesize $Ni_{2-x}Co_xP$ nanoparticles is based on the method refined by our group to synthesize discrete Ni_2P phase-pure nanoparticles.[16] To make the binary nanoparticles, Ni and Co acetylacetonate (acac) complexes are combined at the outset of the reaction with trioctylphosphine (TOP) in a solution of octyl ether and oleylamine (OA) as shown in Scheme 3.1. This was heated to 230°C to prepare the Ni-Co-P alloy precursor particles, which are then converted to the crystalline ternary phosphide by adding an additional aliquot of TOP and heating to 350°C. In the original Ni_2P study, we observed that the initial TOP:M:OA=10.0:2.0:8.0 molar ratio resulted in nearly monodisperse (±20% S.D., in the terminology coined by Finke[111]) and discrete amorphous intermediate Ni_xP_y precursor particles. Accordingly, in all the Ni, Co compositions targeted, the initial molar ratio was set to TOP:M:OA = 10.0:2.0:8.0 while the final TOP:M ratio was increased to 11.2 by injecting an additional 6.0 mL of TOP at 350°.

3.3.1 Structure and morphological changes of ternary phosphide nanoparticles with composition

Ni_2P and Co_2P adopt the hexagonal Fe_2P and orthorhombic Co_2P structure-types, respectively. Both have two metal sites, M(1) and M(2) with tetrahedral and squre pyramidal geometries, respectively, defined by P. However, the two structures differ in the packing of rhombohedral subcells containing M(1) and M(2) sites within the crystal (Figure 3.1). Each P atom is in a tri-capped trigonal prismatic geometry defined by Ni atoms.

The products of the different targeted compositions obtained were characterized for phase by PXRD, morphology by TEM, and composition by EDS. Figure 3.2 illustrates the PXRD patterns for different targeted compositions.

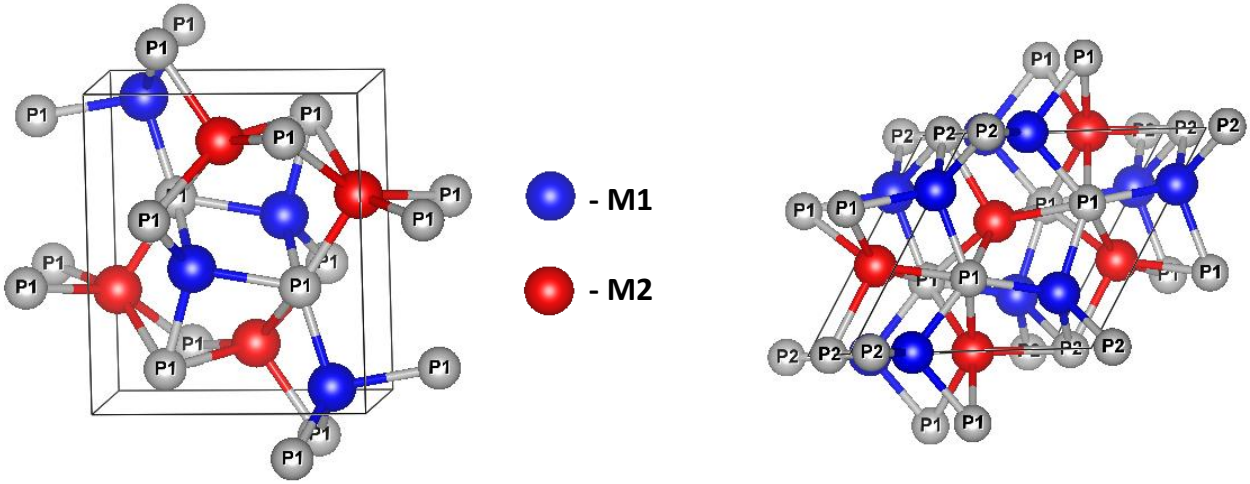

Figure 3.1. Orthorhombic Co_2P structure-type (left) hexagonal Fe_2P structure-type (right).

In Figure 3.2 the patterns match the Ni_2P (hexagonal) structure in the nickel rich region and this phase is clearly maintained up to a targeted composition of $Ni_{0.67}Co_{1.33}P$, at which point we observed a change in the pattern. For the nickel rich compositions, there is a broad peak near 55° 2Θ corresponding to the overlapping reflections of (300) and (211) planes. Due to the small size of the crystallites these two peaks overlap, resulting in one broad peak. However, for the composition $Ni_{0.67}Co_{1.33}P$, we observed the appearance of two peaks that shift away from each

other as the Co is increased. This splitting can be attributed to a separation of the (300) and (211) reflections upon Co-incorporation, or a shift to the Co_2P structure type. Importantly, all observed

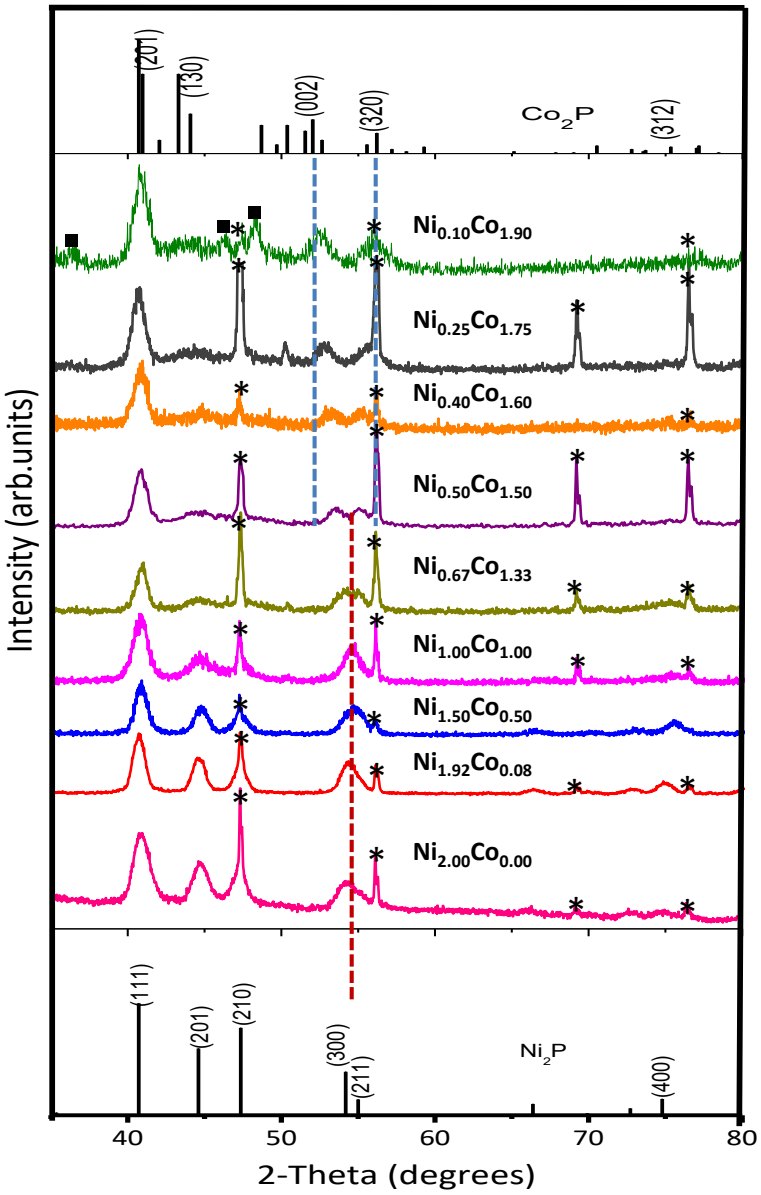

Figure 3.2. PXRD patterns for different targeted compositions of $Ni_{2-x}CoxP$. Reference patterns for Co_2P and Ni_2P are shown for comparison with drop lines indicating the major distinguishing peaks for the two phases. The sharp peaks denoted with * arise from an internal Si standard. Peaks denoted with ■ arise from a CoP impurity.

peaks for compositions up to x=1.75, could be assigned to the desired ternary phase, suggesting that homogeneous materials can be prepared in this composition space (i.e., no detectable crystalline impurities are present). However, at the very Co-rich end (x=1.9), CoP is observed as an impurity. Likewise, this methodology is unsuccessful at preparing phase pure Co_2P; attempts to do so produce a mixture of Co_2P, CoP and unidentified impurities (Figure 3.3).

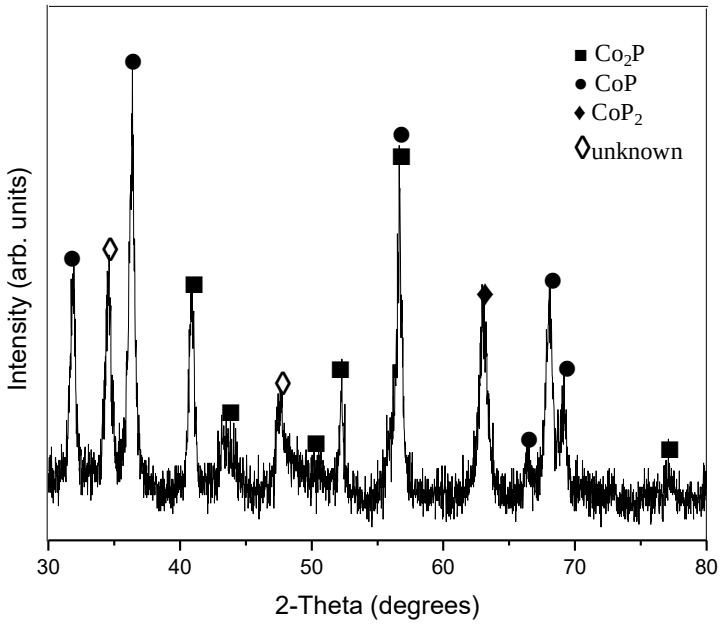

Figure 3.3. PXRD pattern of the reaction attempted to synthesize pure Co_2P

Table 3.1. Ni:Co target and actual (as assessed by EDS) metal ratios, crystallite sizes (by Scherrer application to PXRD data), particle size (by TEM) and refined lattice parameters for different compositions of $Ni_{2-x}Co_xP$

Target ratio (Ni:Co)	Actual ratio (Ni:Co)	Crystallite size (nm)	TEM size (nm)	Lattice parameters (Å)					Molecular Volume (Å^3)
				Ni_2P type refined		Co_2P type refined			
				A	c	a	b	c	
2.00 : 0.00	2.00 : 0.00	9.1	11.26±0.34	5.889(5)	3.364(2)	-	-	-	33.69
1.92 : 0.08	1.91 : 0.09	10.3	12.36±0.65	5.877(9)	3.372(3)	-	-	-	33.62
1.50 : 0.50	1.52 : 0.48	9.6	11.09±0.97	5.877(5)	3.354(3)	-	-	-	33.43
1 : 1	1.06 : 0.94	8.1	9.77±0.94	5.853(6)	3.381(3)	-	-	-	33.44
0.67 : 1.33	0.71 : 1.29	10.9	13.28±2.04	5.824(9)	3.398(4)	-	-	-	33.27
0.5 : 1.5	0.55 : 1.45	10.0	12.73±1.98			5.851(9)	6.530(7)	3.414(6)	32.62
0.4 : 1.6	0.44 : 1.56	9.1	11.57±2.07	-	-	5.83(3)	6.44(3)	3.42(2)	31.98
0.25 : 1.75	0.29 : 1.71	9.5	12.5±1.88	-	-	5.801(7)	6.468(5)	3.443(3)	32.30

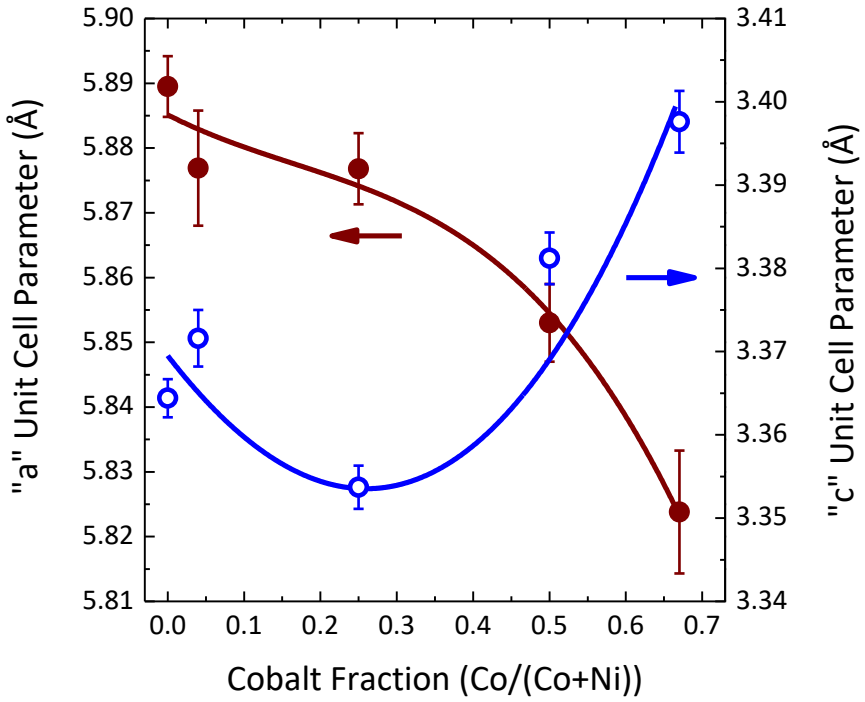

Figure 3.4. Hexagonal unit cell parameters (Ni_2P structure) plotted as a function of the Co content (polynomial fits are guides for the eye).

All the PXRD patterns were calibrated using silicon as an internal standard. Crystallite sizes were calculated by application of the Scherrer equation to the most intense peak, around 41°,

corresponding to the (111) plane of Ni_2P or to the overlapping(121), (201) planes of Co_2P (Table 3.1). The crystallite sizes range from 8-11 nm with no discernible size trends based on composition.

The PXRD patterns were analyzed using the Rietveld refinement method in order to determine the lattice constants for the phase-pure $Ni_{2-x}Co_xP$ materials. The refined lattice constants and molecular volumes (Ni_2P structure: (unit cell volume)/3; Co_2P structure: (unit cell volume)/4) are listed in Table 3.1. For nominal compositions $x<1.5$, the PXRD patterns were refined starting from the Ni_2P structure (PDF#74-1385) and good fits were obtained. However, attempts to refine the $x=1.5$ composition on the hexagonal structure resulted in a poorer quality fit of the pattern. Thus, for the three most Co rich compositions, refinement was carried out based on the Co_2P structure (PDF#32-0306), resulting in a notable improvement in the fit and more reasonable lattice parameters. Intriguingly, the phase transformation appears at a somewhat more Ni-rich composition in our nanoparticles than is reported for the bulk material ($x = 1.7$).[58, 112]

The unit cell parameters for the $Ni_{2-x}Co_xP$ materials adopting the Ni_2P structure ($x<1.5$) are consistent with those reported for bulk phases of similar composition, and exhibit clear trends as a function of Co content as shown in Figure 3.4. The "a" lattice parameter decreases with increasing Co content while the "c" lattice parameter shows a minimum for the $Ni_{1.50}Co_{0.50}P$ composition. The orthorhombic unit cell parameters for the three most Co-rich compositions, which were fitted based on the Co_2P structure, are also consistent with those for bulk phase $Ni_{2-x}Co_xP$ materials.[58, 112] Except for the $Ni_{0.4}Co_{1.6}P$ composition, which yielded the poorest fit, the molecular volumes calculated for the nanoparticle samples (Table 3.1) using the results of the

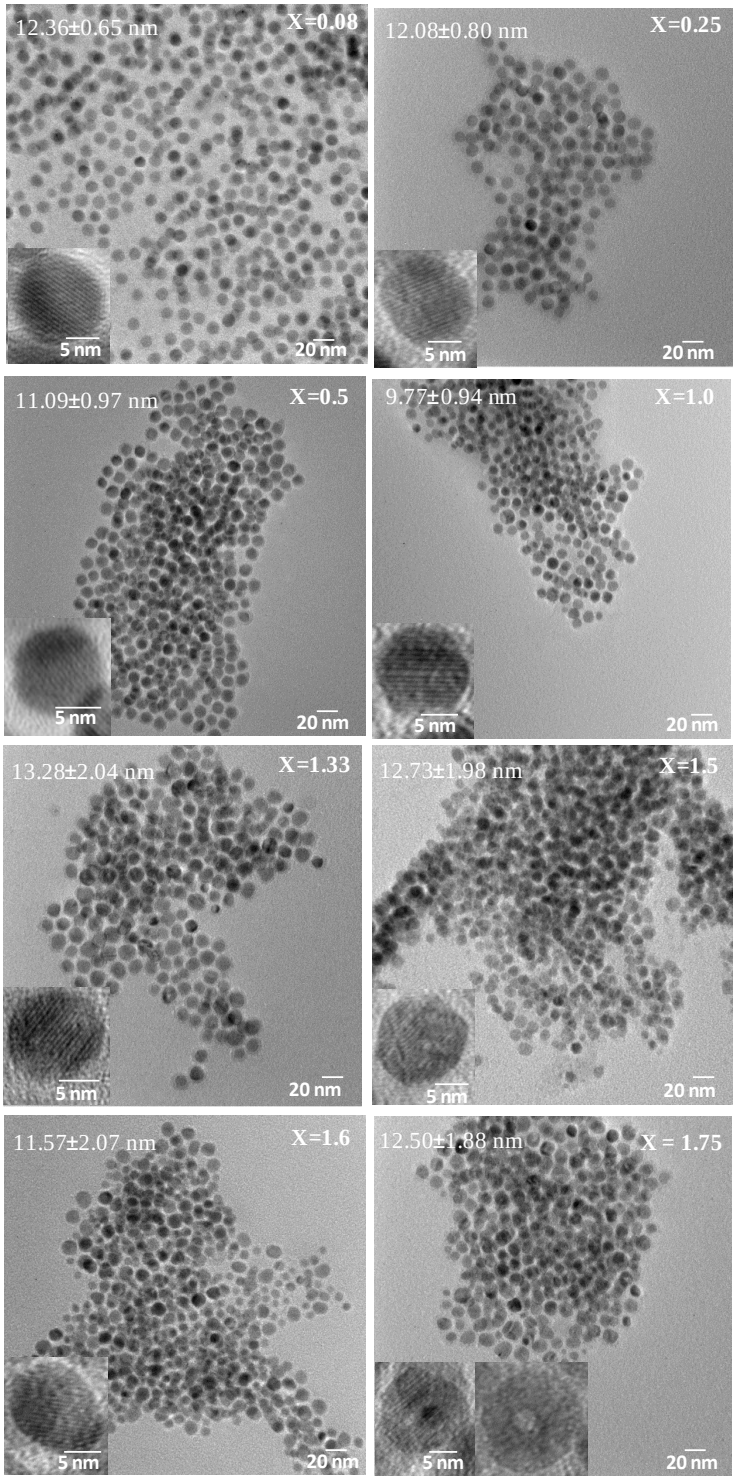

Figure 3.5. TEM images for $Ni_{2-x}Co_xP$ nanoparticles (targeted compositions indicated). The insets illustrate HRTEM images for each composition showing lattice fringes and, for x=1.75, hollow particle formation.

Rietveld refinement analyses, are in excellent agreement with those noted previously for bulk phase $Ni_{2-x}Co_xP$ materials over the entire composition range investigated ($0 \leq x \leq 1.75$).[112] The unusual trend observed for the hexagonal unit cell parameters, with "c" exhibiting a minimum value near the composition $Ni_{1.50}Co_{0.50}P$, has been attributed previously to ordering of the metal atoms in the M(1) and M(2) sites.

Neutron diffraction measurements carried out on bulk phase $Ni_{2-x}Co_xP$ materials (x = 0.8, 1.0, 1.2) showed a strong preference for Ni atoms to occupy the square pyramidal (M(2)) sites, which is unexpected based on atomic size (covalent radii: Ni - 121 pm, Co - 126 pm).[113] For $Co_{1.0}Ni_{1.0}P$, Artigas et al. observed that 80.5% of the M(2) sites were occupied by Ni atoms, while only 19.5% of the more spatially confined M(1) sites were occupied by Ni atoms. The extent of ordering of the metal atoms in the M(1) and M(2) sites increased with increasing Ni content. Preferential ordering of the metal atoms has been observed for Ni and Fe in bulk and nanoscale $Ni_{2-x}Fe_xP$ materials as measured by Mössbauer spectroscopy.[69, 114]

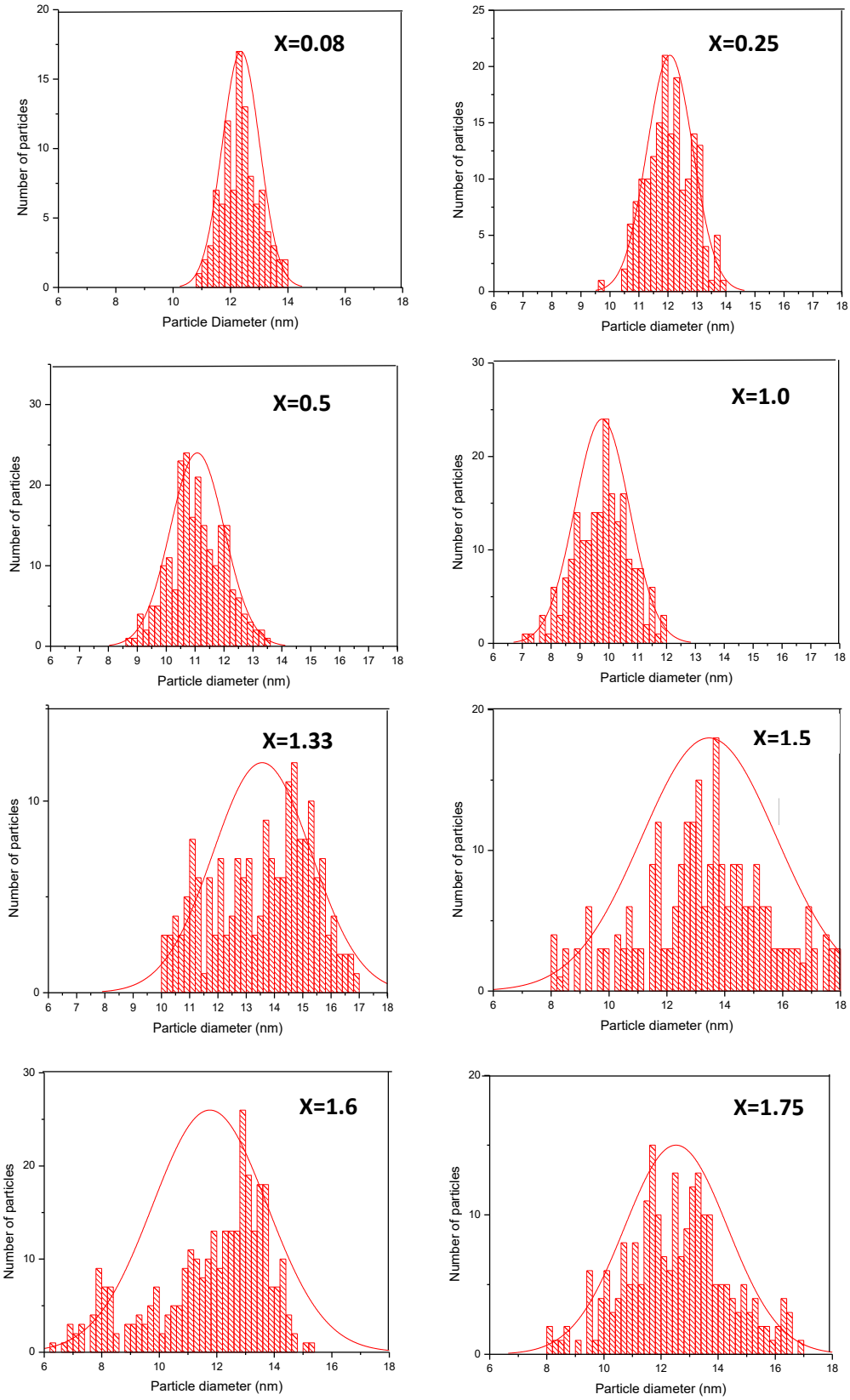

Figure 3.6. Histograms for the particle size distribution for different compositions of $Ni_{2-x}Co_xP$

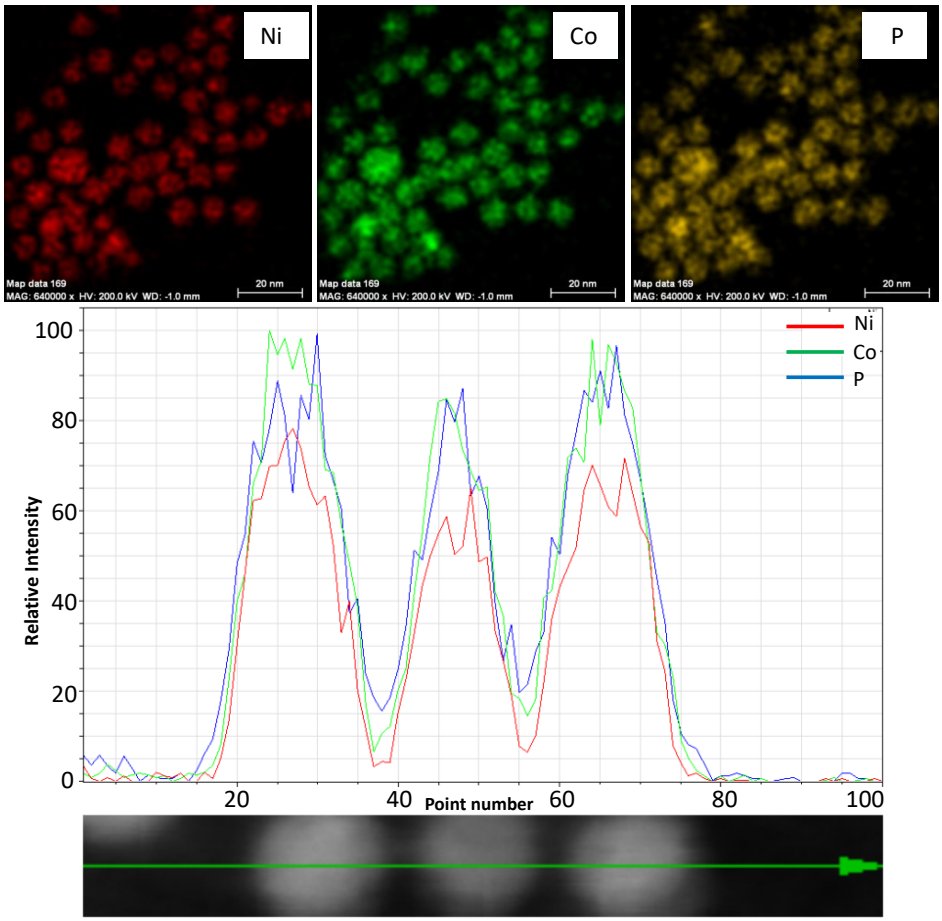

Figure 3.7. STEM images and elemental mapping data for a $Ni_{0.67}Co_{1.33}P$ sample. In the plot of intensity vs. point number, Ni is shown in red, Co in green and P in blue.

The morphology, particle size and composition of the $Ni_{2-x}Co_xP$ nanoparticle materials were analysed by TEM and EDS, respectively, and the results are shown in Figure 3.5 and Table 3.1. The particle sizes are in the range 9-14 nm, slightly larger, but comparable to values obtained from crystallite size analysis of the PXRD data (Table 3.1). The standard deviations range from ± 5-18% with greater deviations manifesting for x>1.0.

The particle size distribution histograms with Gaussian profiles are shown in Figure 3.6 for all compositions. The histograms reveal a larger size distribution of particles for cobalt rich compositions. However, for all compositions the standard deviation is < ±20. High resolution TEM

(HRTEM) images were taken for all compositions and are shown as insets in each TEM image. Lattice planes are evident throughout the crystallites, but at the Co-rich compositions, hollow particles are also observed. The formation of hollow particles may be attributed to the diffusion rate differences between metals and P, according to the Kirkendall effect.[52] In previous studies the formation of hollow particles for cobalt phosphides has also been noted, suggesting that Co is a highly mobile metal within the phosphide lattice.

In comparing the sizes obtained from PXRD (by application of the Scherrer equation) to TEM (average from histrogram), it is evident that the former method is slightly underestimating the size. This may be due to an amorphous layer on the particle surface, polydispersity of particles and/or the presence of hollow particles for some compositions (x=1.75 in Figure 3.5). Additionally, the TEM size measurement method could be contributing as the software models assume a perfect sphere, but TEM images indicate that some particles are elongated along the a or c axes (see Figure 3.5 inset, x = 1.5).

From the EDS analysis the compositions of the materials were calculated and the metal ratio is found to be close (within 5-20%) to the ratio employed in the synthesis, as shown in Table 3.1. STEM images and elemental mapping data for the $Ni_{0.67}Co_{1.33}P$ composition show that the two metals are homogeneously distributed within a particle, consistent with solid-solution formation (Figure 3.6). Overall the developed protocol is ideal to synthesize $Ni_{2-x}Co_xP$ nanoparticles as nearly monodisperse samples ($\leq\pm$20% S.D.)[111] with good control of composition in the range $x<1.7$.

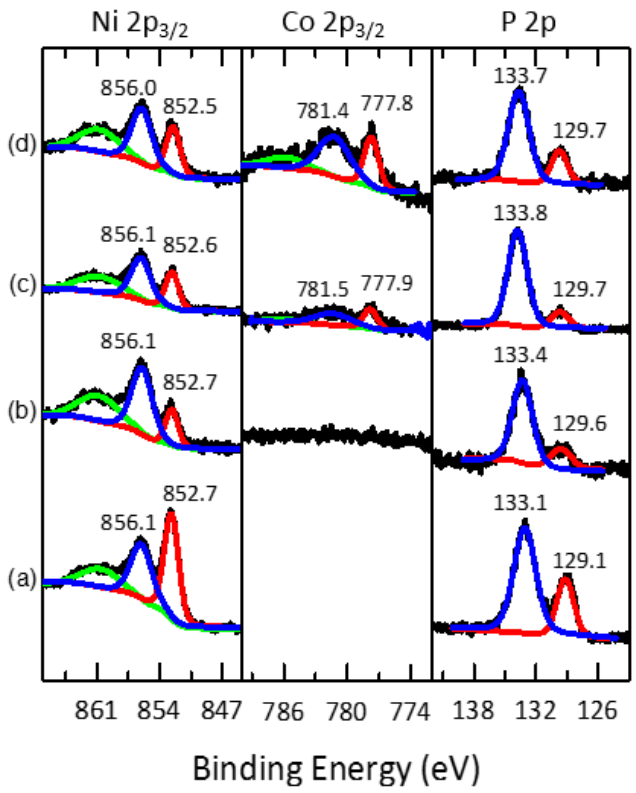

Figure 3.8. XPS spectra of $Ni_{2-x}Co_xP$ nanoparticle compositions: (a) Ni_2P, (b) $Co_{0.08}Ni_{1.92}P$, (c) $Co_{0.25}Ni_{1.75}P$ and (d) $Co_{0.50}Ni_{1.50}P$ in the Ni($2P_{3/2}$), Co($2P_{3/2}$) and P(2P) regions.

The surfaces of some of the $Ni_{2-x}Co_xP$ compositions (x =0, 0.08, 0.25, 0.50) were probed with XPS and the resulting spectra in the Ni($2P_{3/2}$), Co($2P_{3/2}$) and P(2P) regions are shown in Figure 3.8.

The binding energies observed for Ni (856.0-856.1 eV), Co (781.4-781.5 eV) and P (133.1-133.8 eV) correspond to the oxidized phase of each component resulting from the oxide layer formation on the nanoparticle surface due to air exposure. Those binding energies noted for each component correspond to Ni^{2+}, Co^{2+} and P^{5+}, respectively.[115] The oxide layer is not an issue for catalytic studies as these materials are preheated under reducing conditions prior to catalytic testing. The binding energy observed for reduced P species (129.1-129.7 eV) is lower than that for the elemental P (129.9-130.2 eV).[35, 116] This is attributed to a higher electron density present in these phosphides caused by transfer of electron density from the metal species to the more

electronegative phosphorus. The lower binding energies for P are consistent with previous studies done for Ni_2P/SiO_2 and Co_2P/SiO_2 materials prepared by temperature-programed reduction (TPR). The peaks observed for reduced species of Ni (852.5-852.7 eV) and Co (777.8-777.9 eV) are consistent with the binding energies reported for zero-valent Ni (852.5-852.9 eV) and Co (778.1-778.2 eV).[41, 117, 118]

The binding energies for the present ternary phosphide components are in the range of values observed by Bussell and coworkers in their study of TPR-prepared $Ni_{2-x}Co_xP/SiO_2$.[71] XPS studies were performed for three compositions (x=0.25, 1.00, 1.75), but there was no clear pattern in binding energy shifts with increasing cobalt. Mar and co-workers studied the effect of metal substitution in bulk $(Ni_{1-x}M_x)_2P$ (M=Cr, Fe, Co) using XPS and X-ray absorption near-edge spectroscopy (XANES).[119] By comparing the satellite intensity of Ni $2p_{3/2}$ XPS spectra and the Ni and metal (Cr, Fe, Co) edge XANES spectra, Mar and coworkers concluded that charge transfer from M to Ni does occur in the $(Ni_{1-x}M_x)_2P$ phases, although this is small in magnitude for bulk Ni_2P doped with Co.

The surface compositions of the $Ni_{2-x}Co_xP$ nanoparticles (x =0, 0.08, 0.25, 0.50) were evaluated by XPS and the normalized metal ratios are shown in Table 3.2. The surface metal compositions closely track those measured by EDS, while the P:M ratios determined by XPS are in the range 2-2.9, indicating that the surfaces are P rich. Surface enrichment in P might be due to the stripping of metal ions from the surface during the nanoparticle washing procedure. The loss of surface metal ions on metal chalcogenide nanoparticles during ligand exchange has been noted by Owen and co-workers.[120] It is likely that a similar mechanism is operable here. Intriguingly, in TPR-prepared Ni rich materials the surface compositions were found to be quite P enriched for

bulk phase materials (P:M = 1.2-4.8),[72] but less so for nanoscale $Ni_{2-x}Co_xP$ particles prepared on a silica support (P:M = 0.51-0.76).[71]

Table 3.2. Surface Compositions for $Ni_{2-x}Co_xP$ Nanoparticle Compositions

Nominal Bulk Composition	Surface Composition	Surface Co/Ni Mole Ratio	Surface P/(Ni+Co) Mole Ratio
Ni_2P	$Ni_{0.44}P_{1.00}$	---	2.3
$Ni_{1.92}Co_{0.08}P$	$Ni_{0.40}Co_{0.02}P_{1.00}$	0.05	2.4
$Ni_{1.75}Co_{0.25}P$	$Ni_{0.29}Co_{0.06}P_{1.00}$	0.21	2.9
$Ni_{1.50}Co_{0.50}P$	$Ni_{0.37}Co_{0.13}P_{1.00}$	0.35	2.0

3.3.2 Mechanistic studies on particle formation: NiCoP

3.3.2.1 Effect of intermediate heating temperature and heating time on precursor particle formation and templating

Based on our experience with Ni_2P, the initial hypothesis regarding the mechanism of $Ni_xCo_{2-x}P$ particle formation was that an intermediate mixed-metal phase was formed at 230 °C and these particles acted as templates for the final ternary phosphide. To test this hypothesis, intermediate particles were isolated after the synthesis step at 230 °C with TOP:M=4.48 (8.96 mmol:2.00 mmol) for a representative composition, Ni:Co=1:1 (Scheme 3.1). As shown in Figure 3.9a, precursor particles formed at 230 °C were found to have CoO, NiO or a mixed metal oxide as the only crystalline phase. NiO and CoO are virtually indistinguishable by PXRD but CoO is the more likely impurity phase as we do not see NiO in the binary Ni_2P synthesis.[16] Our presumption of CoO formation is also consistent with a study done by Seo et al.[121] In their work, a reaction protocol of $Co(acac)_3$ and oleylamine was developed at 200°C to synthesize two different phases of CoO, presuming the oxygen was contributed by the acetylacetonate ligand in the metal precursor complex. From the TEM image in Figure 3.9(a), it is evident that while some spherical particles form, much of the product consists of features < 1 nm, most likely nuclei. We do observe an

amorphous shell on these particles that may be due to an amorphous layer of reactant species or uncrystallized oxide on the particle surface. Thus, it appears that while nucleation starts at 230 ℃, particle growth is incomplete at the 1.5 h mark, unlike the case for pure Ni_2P.[16] Nevertheless the final ternary phosphide particles obtained are nearly monodisperse and spherical, as shown in Figure 3.5.

In order to better understand the chemical and structural changes that occur upon heating the precursor particles to the crystallization temperature (350°C), the initial reaction temperature was changed from 230 °C to 260 °C and 290 °C and particles were isolated. For the particles heated at 260 °C no CoO was observed in the PXRD pattern (Figure 3.9b). Instead a broad peak is observed near 44° 2θ that can be indexed to the (111) reflection of fcc Ni (or Co). Based on the breadth of the peak and the absence of any higher order reflections, we presume this to be a metal-P amorphous alloy.[49, 122, 123] The absence of CoO is attributed to reduction to fcc Co metal by oleylamine at this temperature, as observed by Nam et al.[124]

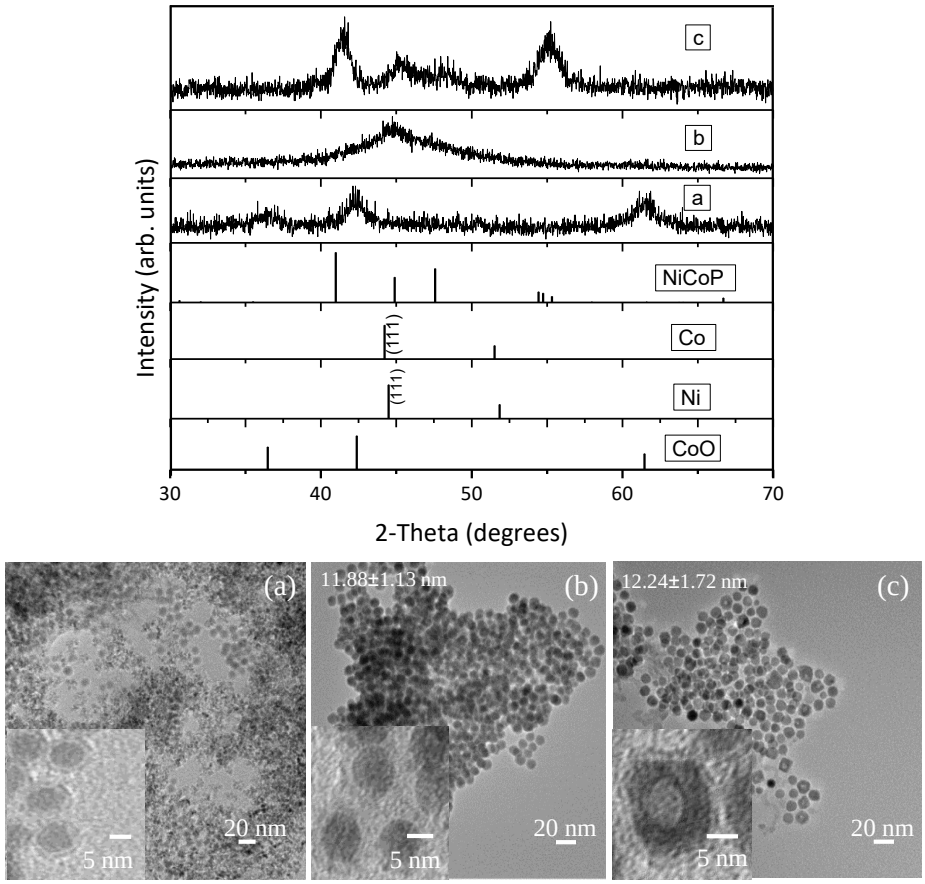

Figure 3.9. PXRD patterns and TEM images of NiCoP nanoparticles obtained from heating at (a) 230 °C (b) 260 °C (c) 290 °C for 1.5 h with TOP:M=4.48 (reference PXRD patterns for CoO, fcc Ni, Co and for NiCoP are shown). The insets in TEM micro-graphs show HRTEM images of representative particles

When the intermediate temperature was increased to 290 °C, the formation of crystalline NiCoP was observed (Figure 3.9c), indicating this temperature is sufficient to crystallize the material. The particle size is slightly larger (8.8 nm from the PXRD data and 12.24 ± 1.72 nm from TEM) than that obtained at 350 °C and some hollow particles are observed (Figure 3.9c). Hollow particle formation for this composition can be attributed to the lower amount of TOP used in the reaction medium relative to the two step synthesis, where a second aliquot of TOP is added before increasing the temperature to form the crystalline phosphide. When less TOP is present, the

concentration of P diffusing into the particles is decreased and the effect of Co-diffusion outward is magnified according to the Kirkendall effect.

Prior studies have shown a strong relationship between the composition and size of the precursor particles and that of the final crystalline phosphide. Robinson and co-workers did a thorough investigation on incorporation of P into Ni nanocrystals, observing that phosphorus incorporation increases with time and temperature.[123] Accordingly, we sought to investigate the effect of time on particle shape and composition at 230 °C and 260 °C.

As shown in Figure 3.10, heating for 1.5 or 3.5 h at 230 °C resulted in CoO as the only detectable phase by PXRD, whereas by 7.5 h the fcc (111) peak manifests as a very broad reflection superposed over peaks for CoO. At the same time, the TEM data show a shift from poorly-defined particles at shorter times to ca 12 nm spherical particles at 7.5 h (Figure 3.10). EDS analysis was carried out for regions with spherical particles and it was revealed that the P amount increased with time (@1.5 h M:P = 24, @3.5 h M:P=5.5, @7.5 h M:P=3.4).

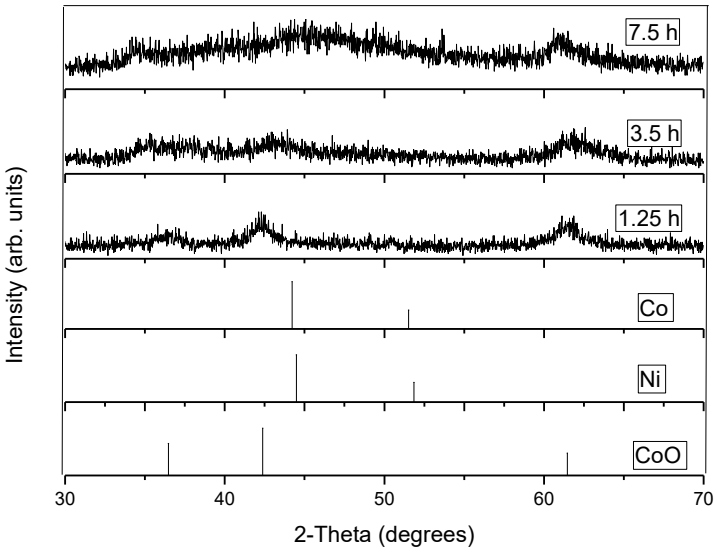

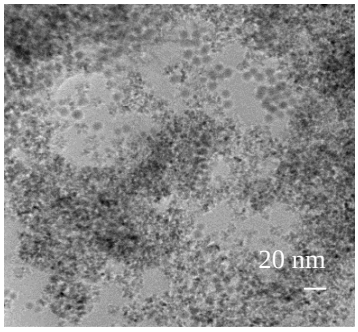

1.5 h

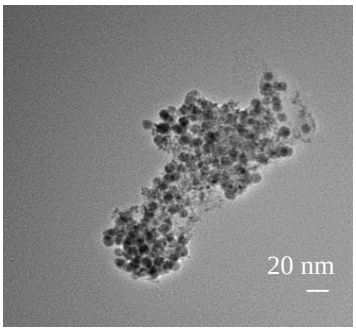

3.5 h

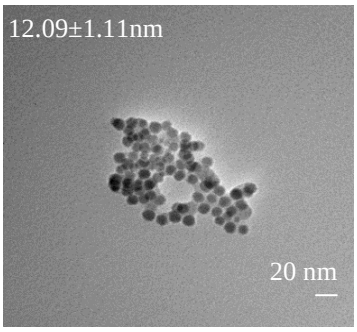

7.5 h

Figure 3.10. PXRD patterns and TEM images of products isolated after heating at 230°C for different time intervals with TOP:M=4.48. (Reference patterns for fcc Co, Ni and for CoO are shown.

A similar series of reactions was done for precursor particle formation at 260 °C at different time intervals, yielding only the (111) reflection by PXRD and a particle size of (again) ca. 12 nm (Figure 3.11). Relative to 230 °C, more P is being incorporated at 260 °C and the extent of incorporation also increases with time (@1.5 h M:P=3.5, @3.5 h M:P=3.2, @7.5 h M:P=2.9). This pattern of P incorporation is similar to that reported by Robinson and co-workers.[123]

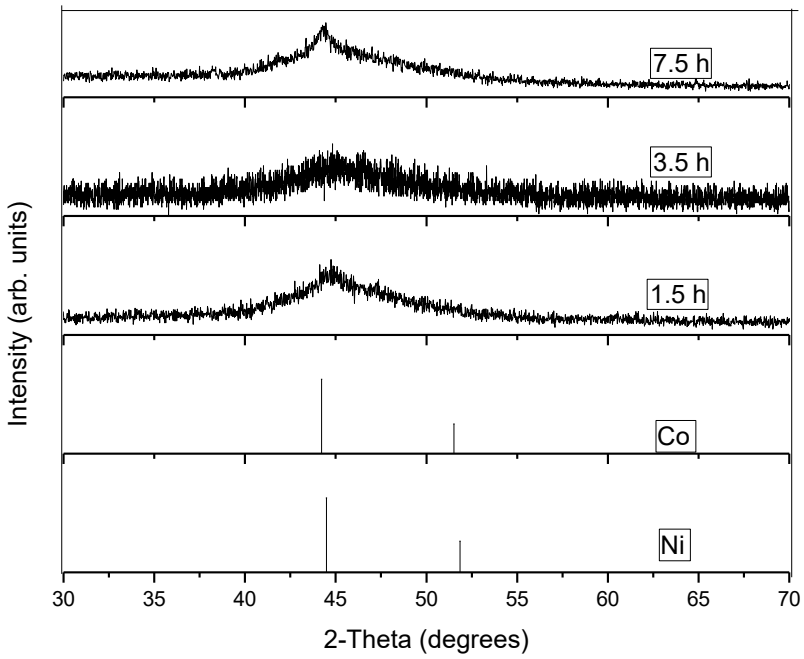

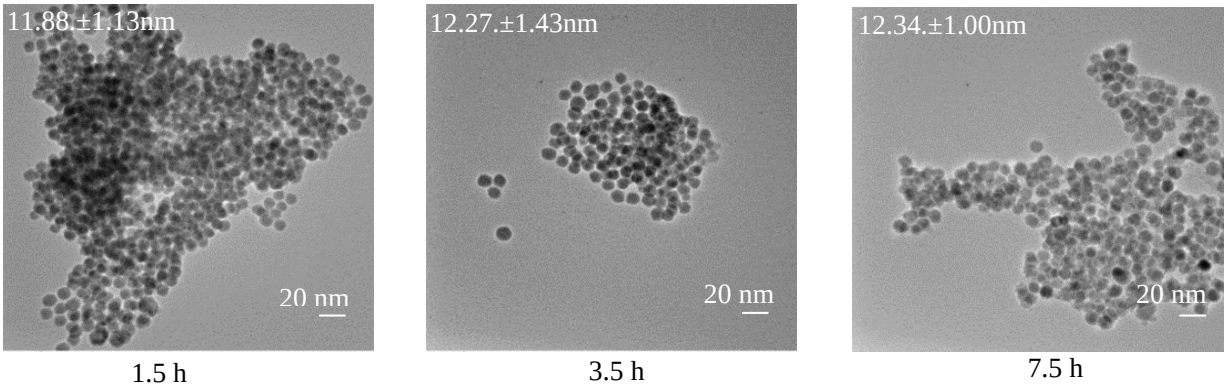

1.5 h 3.5 h 7.5 h

Figure 3.11. PXRD patterns of products isolated after heating at 260°C for different time intervals with TOP:M=4.48. (Reference patterns for fcc Co and Ni are shown.)

To investigate whether spherical precursor particles formed at low temperatures act as templates for the final crystalline ternary phosphide particles, reactions were done by heating at 230 °C and 260 °C for 7.5 h and 1.5 h, respectively, with TOP:M=4.48, and then heated to 350 °C for 4.5 h after injecting an additional 6 mL of TOP, thus modifying only the intermediate step in our standard preparation. In both cases, spherical particles adopting the NiCoP phase were obtained. The size (ca. 13 nm, Figure 3.12) was slightly larger than the precursor particles (ca. 12

nm, Figure 3.10, 3.11), attributed to crystallization and lattice expansion upon inclusion of more P.

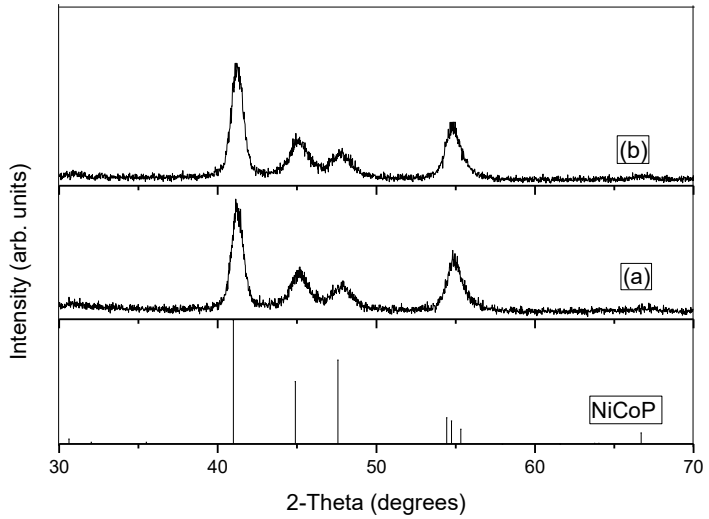

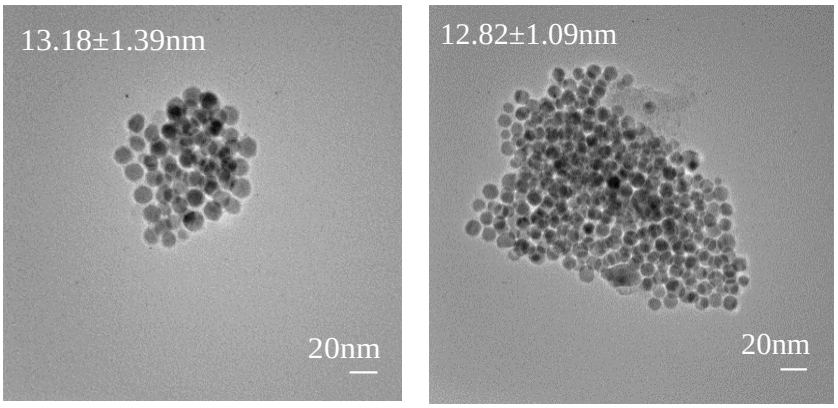

Figure 3.12. PXRD pattern (reference pattern for NiCoP is shown) and TEM images of nanoparticles obtained from heating at (a) 230 °C for 7.5 h (b) 260 °C for 1.5 h with TOP:M=4.48 and then at 350 °C for 4.5 h after injecting an extra 13.44 mmol of TOP.

3.3.2.2 Modifying the precursor particles to increase the size

We sought to modify the size of the precursor particles as a means to control the size of the NiCoP product. This was achieved by using a minimum of TOP in the initial synthesis (1 mL of initial TOP to produce TOP:M=1.12) to force formation of crystalline NiCo nanoparticles over Ni-Co-P amorphous alloys (Scheme 3.1). As shown in Figure 3.13, when the reaction mixture is heated for 7.5 h at 230 °C, crystalline peaks appeared that could be assigned to the (111) and (200)

reflections of fcc Ni-Co alloy, which has a very similar pattern to each of the pure metals as observed by Li et al.[125] The TEM image indicates the particles are larger (20.63±2.14 nm) compared to reactions using 4 mL of TOP, attributed to the lesser degree of stabilization of the particles' surface. In the isolation process the particles adhered to the stirring bar, suggesting ferromagnetic or superparamagnetic behavior that is indicative of Ni-Co alloys, and not of amorphous Ni-Co-P particles, similar to our previous observations for amorphous Ni-P particles.[16]

The precursor particles were subsequently converted to the final ternary phosphide phase by introducing a further 9 mL (20.2 mmol) of TOP at 350 °C to make overall TOP:M=11.2. The final ternary phosphide particles obtained have the correct phase and the size of these particles (23.62±2.85) is again similar to the large precursor particles from which they formed, consistent with templated formation (Figure 3.13). Some hollow particles were also present in the reaction product, attributed to both the large precursor particle size and the absence of P-incorporation inducing a large diffusion gradient for phosphidation.

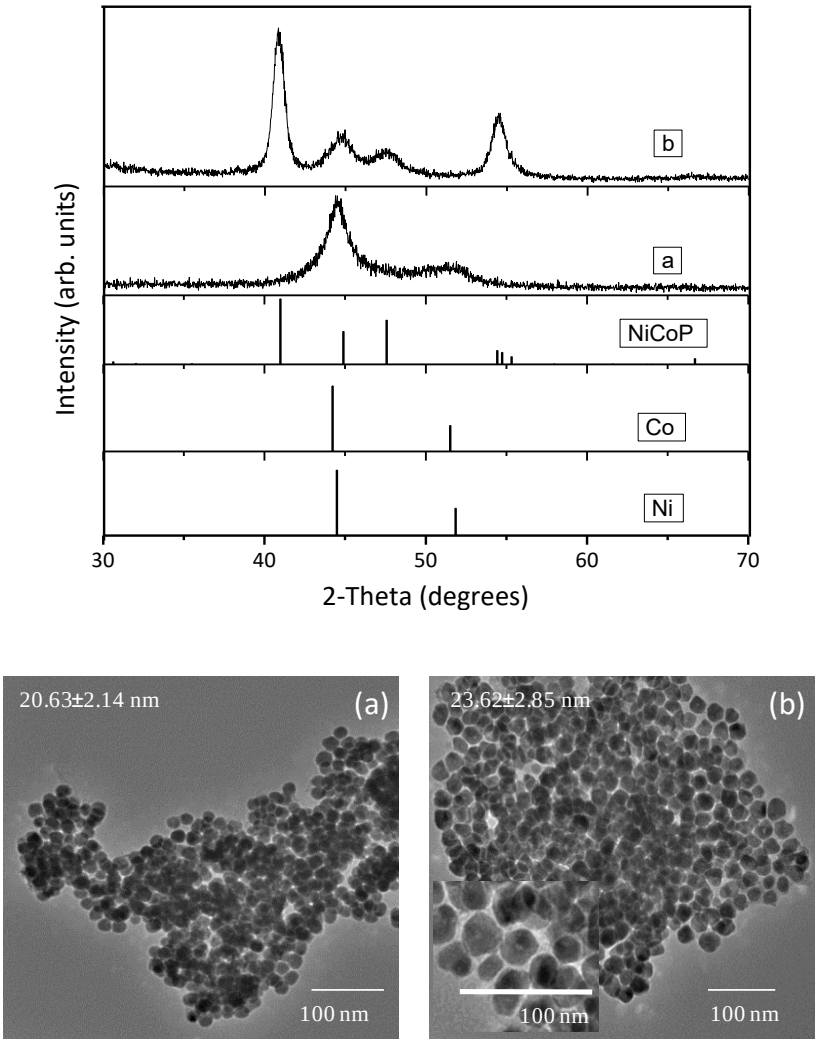

Figure 3.13. PXRD patterns (reference patterns for Ni, Co, and NiCoP are shown) and TEM Images of nanoparticles obtained from reactions (a) initially heated at 230 °C with TOP:M=1.12 for 7.5 h (b) followed by heating at 350 °C for 4.5 h after injection of an additional 20.2 mmol of TOP. The inset shows the enlarged image to highlight the hollow particles.

3.3.2.3 Further size-control by direct heating to the crystallization temperature

Based on the fact that the 230 °C step at short times does not produce well-formed nanoparticles, precursor particle formation likely occurs *en route* to heating to 350 °C. This led us to question whether the low temperature step is necessary or whether direct heating would be suitable to produce ternary phosphide nanoparticles. To test this hypothesis, the reaction mixture was heated directly to 350 °C with a high initial TOP:M=11.2 (10 mL TOP, Scheme 3.1). To

investigate whether any alloy precursor particles are formed at the initial stage of reaction or whether there is any growth in the particle size with the heating time, particles were isolated at different time intervals at 350 °C. As observed by PXRD, during the time interval 1.5-4.5 h at 350 °C, the phase of materials was consistent with crystalline NiCoP (Figure 3.14) and the average particle sizes were the same regardless of time intervals investigated, with a low degree of polydispersity, typically < ±10 % (Figure 3.14). The size of these particles was smaller (7-8 nm) compared to the particles observed in the approach with the intermediate heating step (ca 12 nm). We expect this is the case because the particle growth takes place in the presence of an excess of TOP which facilitates the stabilization of the surface of the particles, inhibiting the growth. If this is the case, it should be possible to increase the size of the product particles by decreasing the quantity of TOP employed. Accordingly, a direct heating reaction was conducted at 350 °C with 4 mL of TOP (TOP:M=4.48) (Scheme 3.1). As shown in Figure 3.15 the particles obtained index to NiCoP in the PXRD and are larger in size (ca 14-15 nm) compared to those obtained from TOP:M=11.2. A consequence of the reduced TOP is, once again, formation of hollows within the spherical NiCoP particles, which accounts for a portion of the increased particle diameter, in addition to the reduced surface stabilization.

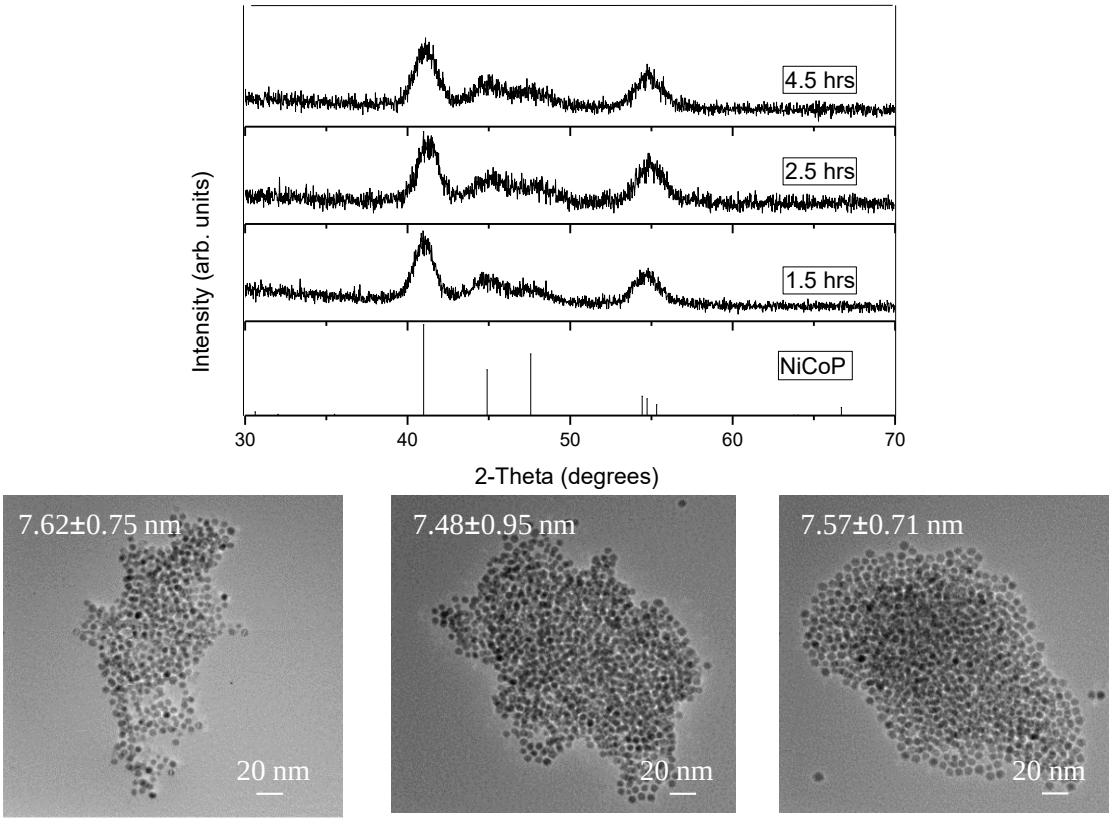

Figure 3.14. PXRD patterns (reference pattern for NiCoP is shown) and TEM images of products isolated from reactions directly heated to 350 ºC for different time intervals with TOP:M=11.2.

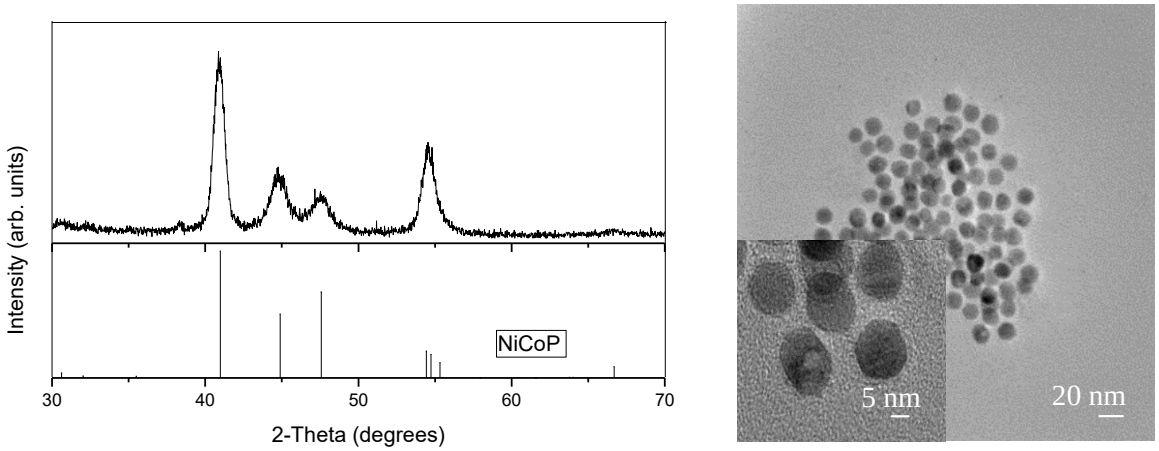

Figure 3.15. (a) PXRD pattern (reference pattern for NiCoP is shown) and (b) TEM image of nanoparticles obtained from reaction directly heating at 350 °C for 4.5 h with TOP:M=4.48

3.4 Conclusions

A solution-phase synthetic protocol is established for production of $Ni_{2-x}Co_xP$ nanoparticles in the range $x \leq 1.7$ as narrow polydispersity samples with control of size, shape, and morphology (dense vs. hollow particles). Composition modulation (x) in the product reflects the starting composition until the very Co-rich end is reached, at which point impurity phases become apparent. Increasing Co-concentration results in an increase in polydispersity and is accompanied by formation of voids within the solid particles due to the Kirkendall effect. A comprehensive study of the role of key parameters on particle formation and growth of the NiCoP phase reveals that precursor particles formed below the crystallization temperature act as templates for the final crystalline product. At low M:P ratios the precursor particles are amorphous metal phosphides of small size (< 10 nm) that transform to dense particles, whereas at high M:P ratios, the precursor particles are large (> 20 nm) crystalline NiCo alloy particles that transform to large hollow NiCoP particles. Formation of precursor particles by a moderate temperature soak is not *a priori* a requirement for NiCoP particle formation. Direct heating to the crystallization temperature also results in narrow polydispersity samples with size controllable by the M:P ratio. The ability to tune the particle size, composition and morphology in $Ni_{2-x}Co_xP$ opens the door to an understanding of how these factors impact the catalytic function, as described in Chapter 5.

CHAPTER 4 SYNTHESIS OF BINARY AND TERNARY RU-P PHASES AND EVALUATION OF OER CATALYTIC ACTIVITY OF $Ni_{2-x}Ru_xP$ NANOPARTICLES

4.1 Introduction

The oxygen evolution reaction (OER) is the most critical reaction in the water splitting process to produce clean H_2 fuel. Ru based phases have emerged as promising materials for OER. Despite the high catalytic activity of Ru metal, the high cost and scarcity impose limitations for using these catalysts for large-scale OER applications. One solution to this challenge is to dilute the noble metal in the catalyst with an Earth-abundant, inexpensive, but comparatively active metal. With respect to dilution of the noble metal component, the OER catalytic activity of Ni metal could be enhanced by Ru incorporation; the overpotential required to achieve a current density of $10 mA \cdot cm^{-2}$ could be reduced from 0.310 V to 0.280 V (in 5 M KOH) upon incorporation of 2.2 % Ru.[126] On the other hand, the native performance of RuO_2 can be further augmented by incorporation of Ni or Co, attributed to activation of proton donor-acceptor functionalities on the conventionally inactive bridge surface sites of rutile RuO_2.[127]

Recently transition metal phosphides both in binary and ternary phases have emerged as efficient catalysts in OER. To the best of our knowledge, there have been no reports evaluating Ru_2P or Ru-Ni-P ternary phases for OER; nor are syntheses available for discrete nanoparticles of such phases, which would enable such studies.

This chapter describes our attempts to prepare ruthenium phosphide and $Ni_{2-x}Ru_xP$ nanoparticles by colloidal routes along with the evaluation of the OER catalytic activity of these phases. All the synthesis and characterization of the materials were carried out by me and an undergraduate student I mentored, Quintin B. Cheek at Wayne State University, and OER measurements and interpretation of data were carried out by my lab mate Da Li.

4.2 Experimental

All the materials used in the syntheses and a description of the characterization techniques are described in chapter 2.

4.2.1 Attempt to synthesize Ru_xP_y nanoparticles by initial combination of $RuCl_3$ and TOP

All reactions were carried out under argon atmosphere using standard Schlenk line techniques. 100 mg of a Ru metal precursor was mixed with 5 mL (8.0 mmol) oleylamine, 2 mL (5.0 mmol) TOP and 10 mL octyl ether in a Schlenk flask fitted with a condenser. The flask was placed on a heating mantle connected to a temperature controller and the thermocouple was inserted between the flask and the heating mantle. The system was degassed at 110 °C for 45 min followed by purging with Ar for 20 min. The system temperature was raised to 260 °C. The initial reaction mixture (dark blue) turned dark greenish after degassing and turned dark with a brownish color when the temperature was increased to 260 °C. Finally, a translucent pale brown solution was obtained, from which no solid particles could be isolated by centrifugation.

4.2.2 Synthesis of Ru nanoparticles

100 mg of a Ru metal precursor was mixed with 5 mL (8.0 mmol) oleylamine, and 10 mL octyl ether in a Schlenk flask. The system was degassed at 110 °C for 45 min followed by purging with Ar for 20 min. The initial color of this solution was dark blue and after the degassing step at 110 °C the color changed to pale orange. The system temperature was raised to 260 °C in order to form the Ru nanoparticles at which point a darkening of the solution was observed. The reaction was heated for 1.5 h at 260 °C. After naturally cooling down to room temperature ethanol was added to the flask and the solution was centrifuged to isolate the precipitate. The precipitate was dispersed again in chloroform, sonicated for 5-10 min and reprecipitated with ethanol. This

sonication and precipitation process was carried out at least two times. A black precipitate was obtained as the final product.

4.2.3 Attempt to synthesize Ru_2P phase at elevated temperatures (350 °C)

For the above-prepared non-isolated Ru nanoparticles solution, the system temperature was raised to 350 °C followed by injecting 6 mL (15 mmol) of TOP. The mixture was heated at 350 °C for 4 h and the final product at room temperature was isolated with the same procedure given for Ru nanoparticles isolation.

4.2.4 Synthesis of $Ni_{2-x}Ru_xP$ nanoparticles

In a typical synthesis, the corresponding amount of Ru precursor, x mmol ($x \leq 2$), was combined with 5.0 mL (8.0 mmol) of oleylamine (coordinating ligand, reducing agent) and 10.0 mL of octyl ether (solvent) in a 200 mL Schlenk flask. The mixture was degassed at 110 °C for 45 min to remove any moisture or oxygen, followed by purging with argon for 20 min at this temperature. The temperature was then increased to 260 °C and maintained for 90 min. In a second flask, the corresponding amount of Ni precursor ($Ni(acac)_2$), 2-x mmol, was mixed with 5.0 mL octyl ether and 2.0 mL (5.0 mmol) of trioctylphosphine (TOP, P source) and this flask was also degassed at 110 °C for 20 min to remove any moisture or oxygen. The second degassed solution was then removed by a syringe, injected into the first flask at 260 °C, followed by further heating for 1.5 h. To avoid any spillage of the Ni precursor solution during injection, a syringe lock was used. Next, the temperature was set to 350 °C; as soon as the temperature started increasing, 8.0 mL (20 mmol) of TOP was injected, followed by heating for 4.0 h. After naturally cooling down to room temperature, the product was isolated with the same procedure given for Ru nanoparticles isolation.

4.2.5 Electrochemical Measurement

Ink Preparation: 50 mg of as-synthesized nanoparticles were mixed with Ketjen-300J carbon (C) (mass ratio, 2:1) in hexane and sonicated for 30 min to form C-NPs. The C-NPs were washed with hexane and reprecipitated by adding excess ethanol. An ink was prepared by mixing 15 mg of C-NPs, 1 mL of the 5 wt% Nafion solution, with a mixture of 2 mL ethanol, 1 mL isopropanol, and 1 mL nanopure water, followed by sonicating for at least 30 min.

Electrochemical Measurements: All the cyclic voltammograms were recorded using an EC epsilon potentiostat equipped with a rotating disc electrode (RDE). In a typical experiment a standard three electrode setup was employed using an Ag/AgCl reference electrode, a Pt wire auxiliary electrode, and a glassy carbon working electrode. The surface (surface area = 0.07 cm^2) of the glassy carbon electrode was modified by depositing 10 μL of nanoparticle ink onto the surface followed by drying under an infrared heat lamp for five minutes. The final catalyst loading is ~0.284 mg/cm^2 for all samples. OER polarization curves were obtained in 1 $mol \cdot L^{-1}$ KOH solution at a scan rate of 10 mV/s with the RDE operating at 1600 rpm. Potential was measured versus Ag/AgCl and converted to the reversible hydrogen electrode (RHE) by using Equation 1. The resistivity of the solution was determined using the iR compensation feature of the epsilon software and corrections were performed manually according to Equation 2.

$$E_{RHE} = E_{Ag/AgCl} + 0.197 + 0.059*pH \quad (1)$$

$$E_{RHE} = E_{Ag/AgCl} + 0.197 + 0.059*pH - iR \quad (2)$$

4.3 Results and Discussion

4.3.1 Synthesis of crystalline Ru_xP_y nanoparticles

In order to target solid solutions of Ni-Ru-P we sought first to modify our existing methodology, developed for Ni_2P,[16] and establish a compatible method for the Ru_2P end-product, a phase that has not been reported as discrete nanoparticles. The synthesis of Ni_2P nanoparticles occurs via formation of amorphous Ni_xP_y (or crystalline Ni) precursor particles that are subsequently converted to the final crystalline Ni_2P particles by heating to a high temperature (350 °C). The precursor particles act as templates for the final crystalline particles and the nature of these precursor particles (amorphous Ni_xP_y or crystalline Ni) is governed largely by the initial TOP:M ratio. Our initial approach to target Ru_2P sought to prepare amorphous Ru_xP_y precursor particles at moderate temperatures and transform them to crystalline Ru_2P via higher temperature processing. However, reaction of the Ru precursor ($RuCl_3$) with TOP in the presence of oleylamine at 260 °C (details in Section 4.2.1) did not lead to an isolable product, nor did continued heating at 350 °C (a brown solution was obtained in each case, from which a precipitate could not be achieved). As we were not successful in preparing Ru-P alloy precursor nanoparticles, we sought instead to employ Ru metal nanoparticles as precursors. Yang and coworkers reported the synthesis of Ru nanoparticles by reaction of $RuCl_3$ and oleylamine.[128] With slight modifications to this method (details in Section 4.2.2), Ru nanoparticles were produced at 260 °C. As shown in Figure 4.1(a), the PXRD pattern for this product revealed a series of broad peaks whose profile could be indexed to the peaks of hexagonal Ru nanoparticles, whereas the TEM revealed worm-like particles only a few nm in diameter.

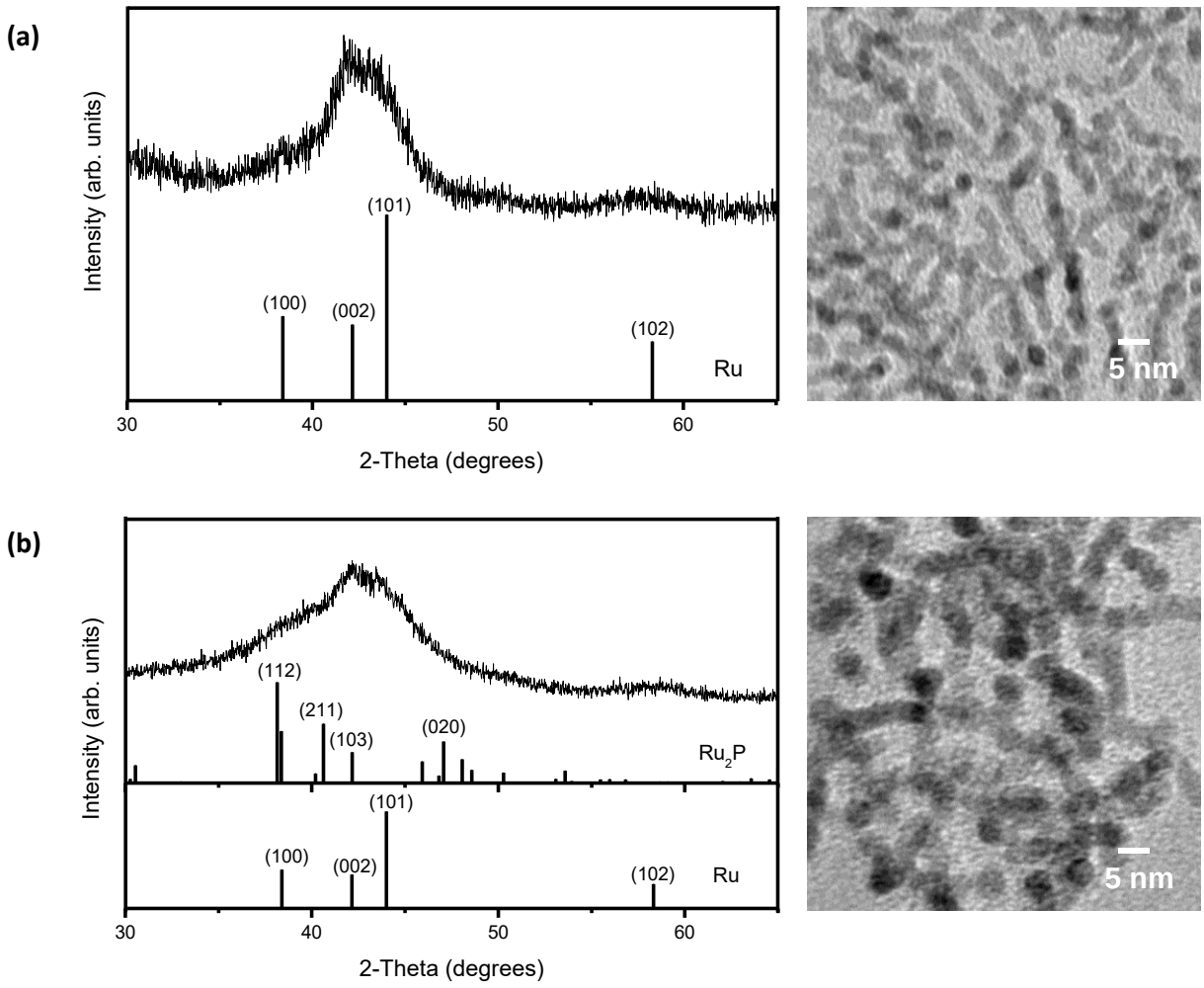

Figure 4.1. (a) PXRD pattern and TEM image corresponding to Ru nanoparticles isolated after heating at 260 °C for 1.5 h; (b) PXRD pattern and TEM image of product isolated by heating Ru nanoparticles at 350 °C for 4 h with 6 mL of TOP.

Next, reaction of pre-formed Ru nanoparticles with TOP was conducted at elevated temperatures (350 °C, 4 h) to access the Ru_2P phase (see Section 4.2.3). As shown in Figure 4.1(b), the PXRD pattern shows broader features than those observed for Ru, and these could be attributed equally well to Ru or Ru_2P. The product of phosphidation had a similar morphology to Ru nanoparticles; however, the particle sizes appear marginally larger by 1-2 nm and the EDS analysis revealed an M:P ratio very close to 2. These data suggest an amorphous Ru_2P phase may form. In an attempt to crystallize this phase, another reaction was carried out, heating for a longer time, 12

h, at 350 °C. As shown in Figure 4.2, the PXRD pattern is broader still, compared to the product heated for only 4 h, and the EDS data revealed an M:P ratio of 0.75, indicating even more P incorporation. The increased phosphidation with time is consistent with a study reported by Robinson and co-workers for Ni nanoparticles, where they reported a direct relationship between P incorporation with heating time and temperature.[123] These data suggest that Ru-P alloy phases can be prepared but remain amorphous at the temperatures we can access with our solvent system (~350 °C). Intriguingly a critical step to alloy formation appears to be heating without TOP during initial Ru nanoparticle formation; specifically, phosphidation and alloy formation does not appear to proceed by direct reaction of molecular or ionic Ru with TOP.

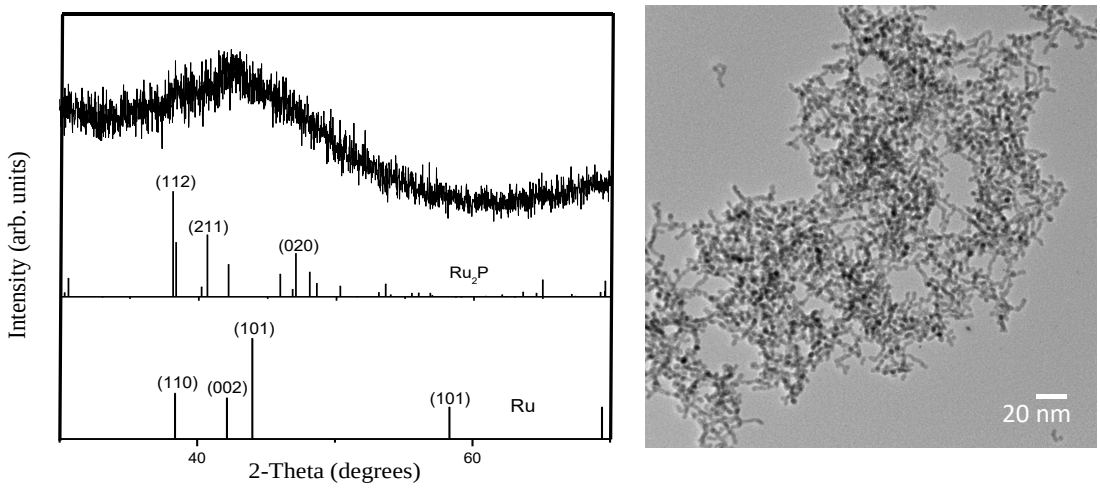

Figure 4.2. PXRD and TEM image of Ru nanoparticles heated at 350 °C for 12 h with 8 mL of TOP

As the materials prepared at 350 °C yielded an amorphous phase, we sought to access the crystalline phase of these Ru-P nanoparticles by annealing the isolated solid in a flowing Ar/H_2 mixture at 450 °C. In the case for amorphous Ru:P~2, when the material is heated for 1 h at 450 °C, Ru_2P phase is obtained, as shown in Figure 4.3(a).

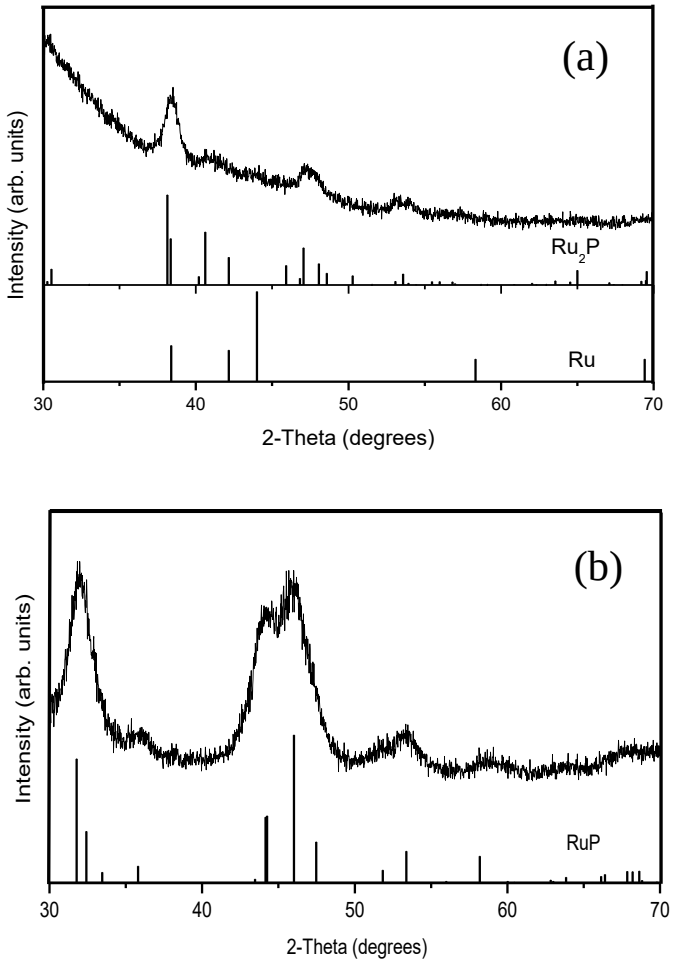

Figure 4.3. PXRD patterns of the product obtained by annealing the amorphous materials (a) Ru:P ~2 (b) Ru:P~1 with Ar/H_2 at 450 °C for 1 h

When the isolated amorphous solid with Ru:P~1 is annealed at 450 °C for 1 h under flowing Ar/H_2 the final product adopts the RuP phase (Figure 4.3(b)). These results suggest the crystalline phase-pure Ru-P phases could be accessed by annealing the solution-phase prepared amorphous materials with the correct Ru:P ratio.

4.3.2 Synthesis of $Ni_{2-x}Ru_xP$ nanoparticles

In previous work reported by the Brock group, crystalline CoMnP nanoparticles could be obtained despite the inaccessibility of the crystalline Mn_2P phase.[63] Inspired by this work, we sought to explore whether, despite the absence of crystallinity in the binary Ru-P systems studied, crystalline phases could be accessed by introduction of Ni. As a starting point, $Ni_{1.75}Ru_{0.25}P$ was chosen as a test composition. A protocol was developed to prepare $Ni_{2-x}Ru_xP$ nanoparticles based on reaction of Ru precursor particles with Ni and TOP (Scheme 4.1). The PXRD pattern of the x = 0.25 product (Figure 4.4) is similar to the pattern for Ni_2P; however the ICP-MS suggests Ru incorporation, consistent with the targeted composition (Table 4.1). In contrast to Ru metal nanoparticles, the TEM suggests the x=0.25 particles are spherical and form with a low polydispersity (Figure 4.6). As this approach was successful in preparing the $Ni_{1.75}Ru_{0.25}P$ composition, we sought to determine the maximum solubility of Ru in Ni_2P and generate a range of phases to test compositional effects on OER activity.

Scheme 4.1. Reaction protocol used for the synthesis of $Ni_{2-x}Ru_xP$ nanoparticles

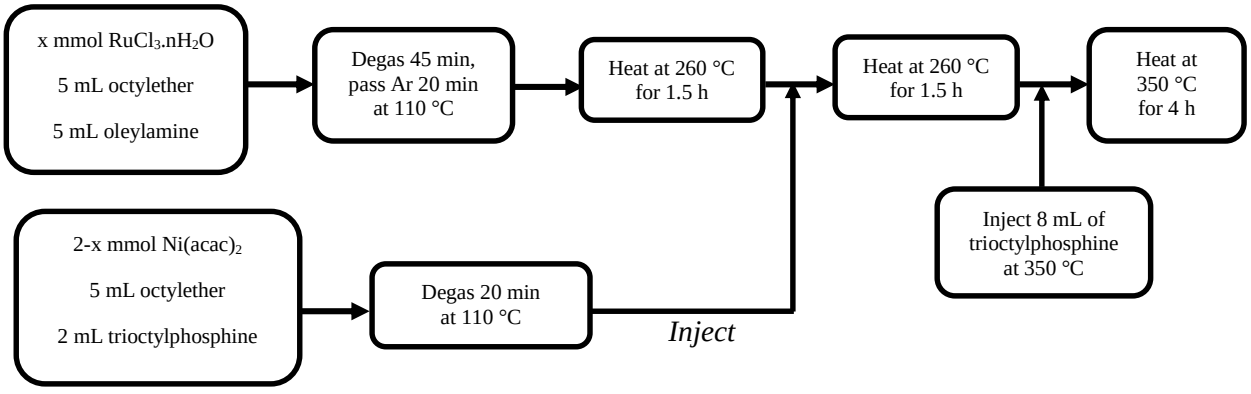

4.3.2.1 Structural and morphological changes of $Ni_{2-x}Ru_xP$ nanoparticles ($x \leq 1$)

A series of compositions $x \leq 1$ were targeted using the protocol outlined in Scheme 4.1. The compositions evaluated by ICP-MS are consistent with the targeted ratios employed in the synthesis (within ±20%) suggesting this method enables reasonable control over the composition (Table 4.1). For all compositions, ICP-MS shows a slight excess of P (10-30 mole %), which could be due to the excess surface bound TOP ligands not completely removed during the washing procedure.

Figure 4.4 shows the PXRD patterns for different values of x; as expected, for the very nickel rich x=0.1 composition, the peaks reflect the Fe_2P-type hexagonal Ni_2P structure. The most discernible change observed in PXRD patterns with increasing Ru amount is that while all peaks broaden to some extent, the (201) and (210) reflections broaden extensively relative to the (111) and (300)/(211) reflections. The broadening of these peaks for Ru-rich compositions might reflect the decreased crystallinity of these materials as observed when Ru_2P was targeted. Intriguingly there are not any Ru_2P-type reflections observed in any PXRD patterns for $x \leq 1$ (no peak at ca. 38° 2Θ that might correspond to the (112) reflection), despite the fact that NiRuP is reported to adopt the orthorhombic Ru_2P structure, suggesting we are accessing a metastable phase[129, 130]. Ni_2P and Ru_2P materials adopt hexagonal and orthorhombic crystal structures, respectively but are otherwise quite similar. Both possess two metal sites; tetrahedral (M1) and square pyramidal (M2) geometries defined by P atoms and in both structures the P atom is coordinated to nine M atoms forming a tricapped trigonal prismatic geometry. The two structures differ only in the way the subunits containing M(1) and M(2) metal sites pack in the structures, Ni_2P (hexagonal) and Ru_2P (zig-zag).[131-133] Presumably, the *chimie douce* synthetic conditions that enable access to discrete nanoparticles of $Ni_{2-x}Ru_xP$ also enable kinetic trapping of the metastable hexagonal NiRuP

phase.[17, 134] As Ru is incorporated, the (111) peak shifts to lower 2Θ angles, as expected based on the larger size of Ru relative to Ni (Figure 4.5).

Particle sizes were calculated for all compositions ($x \leq 1$) by applying the Scherrer equation to the most intense peak, around 41° 2θ, corresponding to the (111) plane of the Ni_2P structure. As shown in Table 4.1, crystallite sizes varied from 6-9 nm and there is an obvious trend in the size; with increasing the amount of Ru, the crystallite sizes decreased.

Table 4.1. Ni:Ru target and actual (as assessed by ICP-MS) metal ratios, crystallite sizes (by application of the Scherrer equation to PXRD), and particle sizes (by TEM) for different $Ni_{2-x}Ru_xP$ compositions.

Target Composition	Actual Composition (From ICP-MS)	Crystallite size (nm)	TEM size (nm)
$Ni_{1.9}Ru_{0.1}P$	$Ni_{1.91}Ru_{0.09}P_{1.1}$	8.7	10.18±1.34
$Ni_{1.75}Ru_{0.25}P$	$Ni_{1.79}Ru_{0.21}P_{1.2}$	7.6	8.18±0.98
$Ni_{1.67}Ru_{0.33}P$	$Ni_{1.71}Ru_{0.29}P_{1.3}$	6.7	7.01±0.92
$Ni_{1.5}Ru_{0.5}P$	$Ni_{1.55}Ru_{0.45}P_{1.2}$	6.6	6.88±0.68
$Ni_{1.25}Ru_{0.75}P$	$Ni_{1.33}Ru_{0.67}P_{1.3}$	6.3	6.05±0.82
$Ni_{1.0}Ru_{1.0}P$	$Ni_{1.08}Ru_{0.92}P_{1.2}$	5.9	5.20±0.72[a]

[a]Elongated particles were excluded from the size measurement

The morphology was evaluated using transmission electron microscopy (TEM) and images corresponding to each composition are shown in Figure 4.6. For very Ni-rich compositions, the materials exhibit a spherical morphology, but as the Ru amount is increased, the morphology shifts from spherical particles to elongated particles, reminiscent of Ru and Ru-P alloys (Figure 4.1). The particle sizes varied from 5-10 nm with an obvious decreasing trend upon increasing the amount of Ru (Table 4.1) mirroring what was observed in crystallite sizes calculated from PXRD data. As

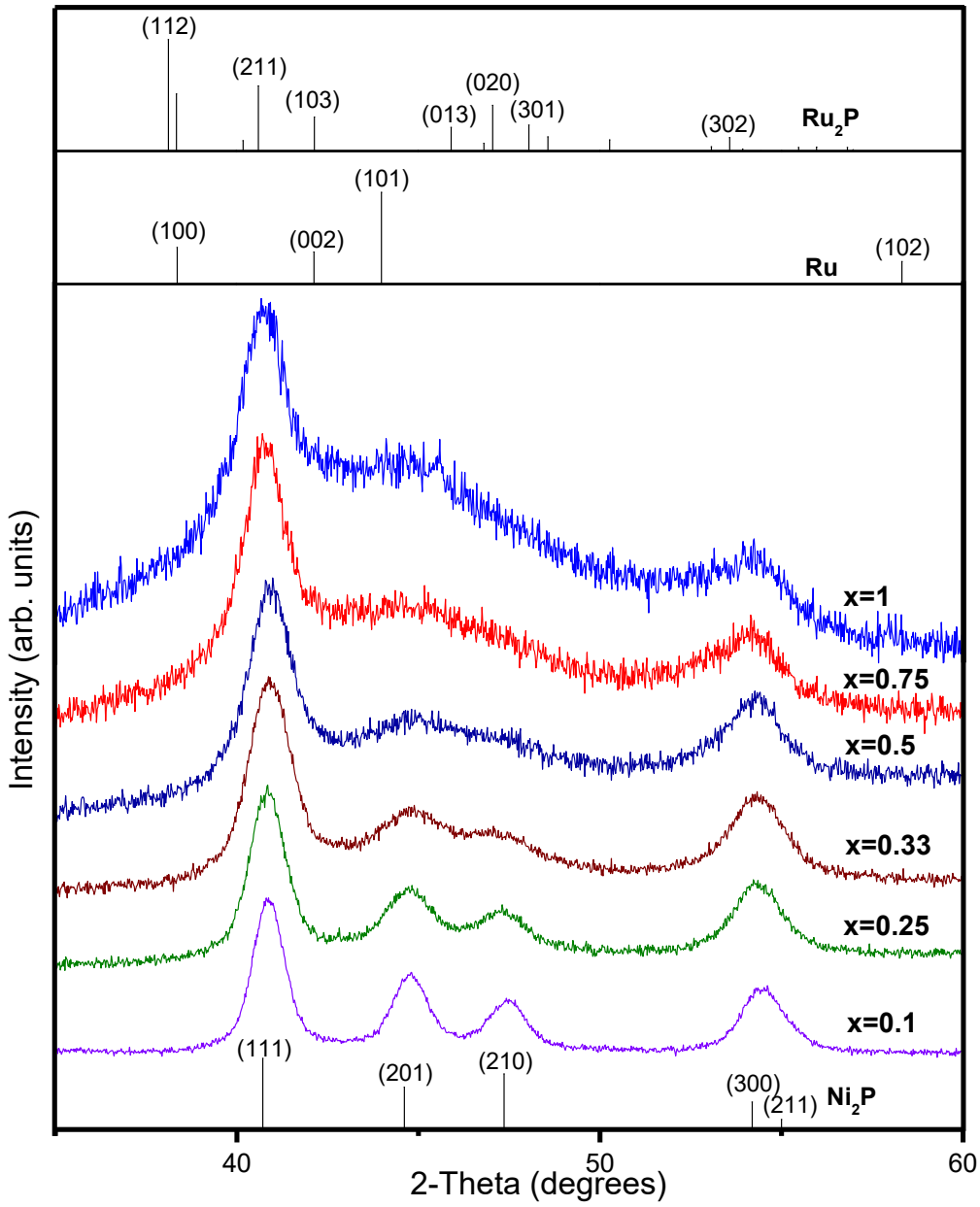

Figure 4.4. PXRD patterns for different targeted compositions of $Ni_{2-x}Ru_xP$. Reference patterns for Ni_2P, Ru_2P and Ru are shown for comparison. Magnified peaks for the (111) reflection (calibrated against a Si internal standard) of the calibrated patterns are shown in Figure 4.5.

shown in Figure 4.7, all compositions show narrow size distributions. Polydispersity (p) which is defined by p=σ/μ (σ is the standard deviation of sizes and μ is the mean size) is calculated for all compositions and varied <15%.[97] For x=1 the morphology of particles deviated from spherical; sizes were obtained based the more isotropic population of particles (insets of Figure 4.6).

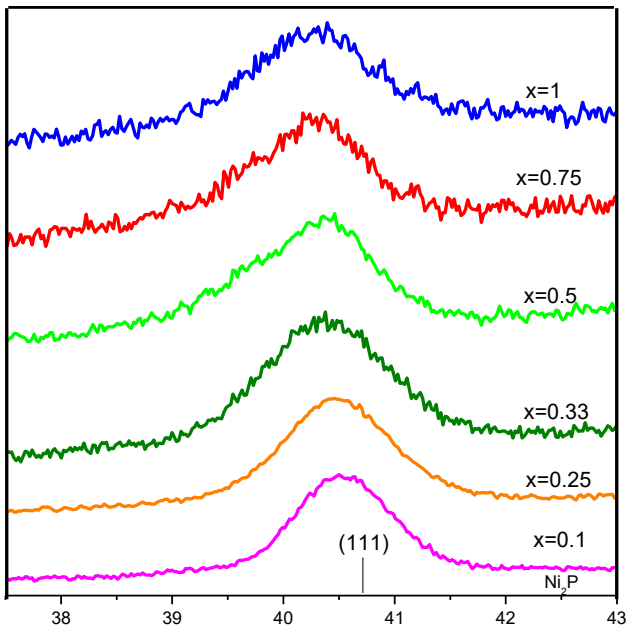

Figure 4.5. (111) reflection of PXRD patterns calibrated against Si as an internal standard

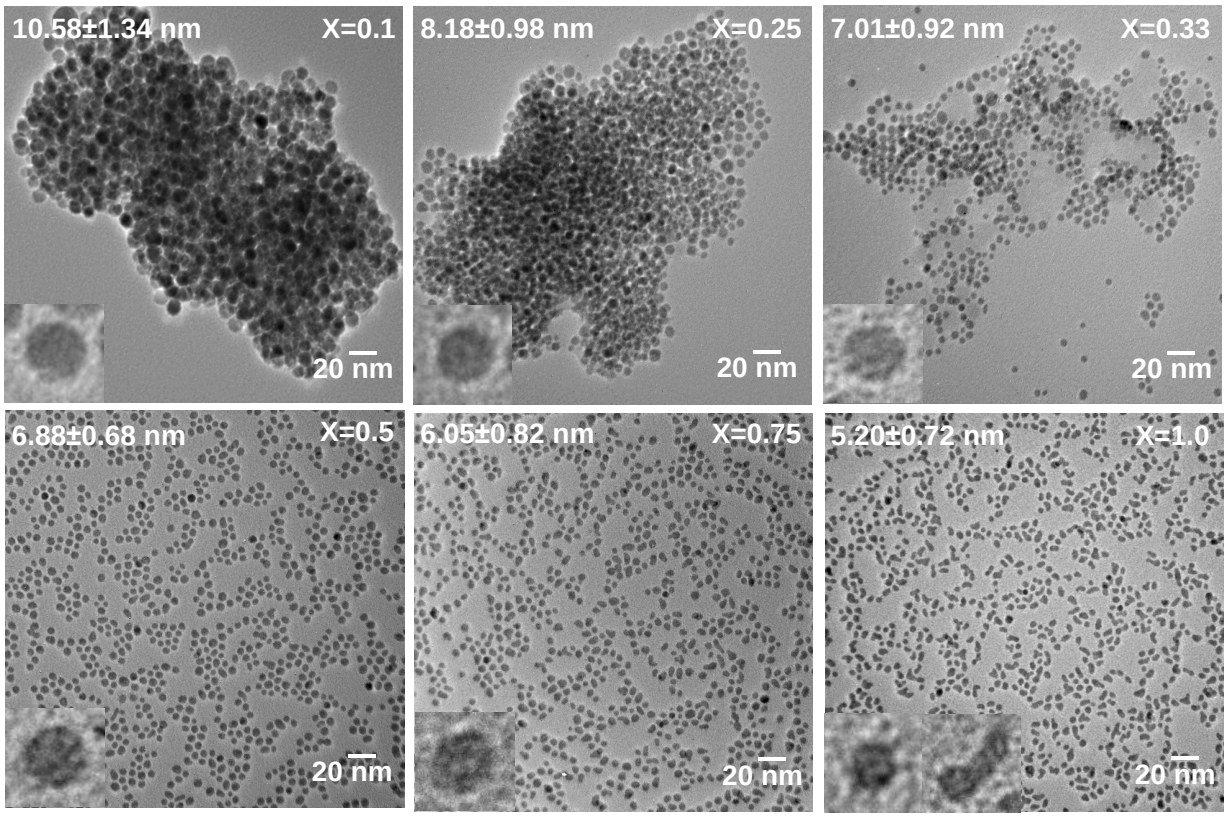

Figure 4.6. TEM images for $Ni_{2-x}Ru_xP$ nanoparticles (targeted compositions indicated, with sizes obtained from size histograms (see Figure 4.7)

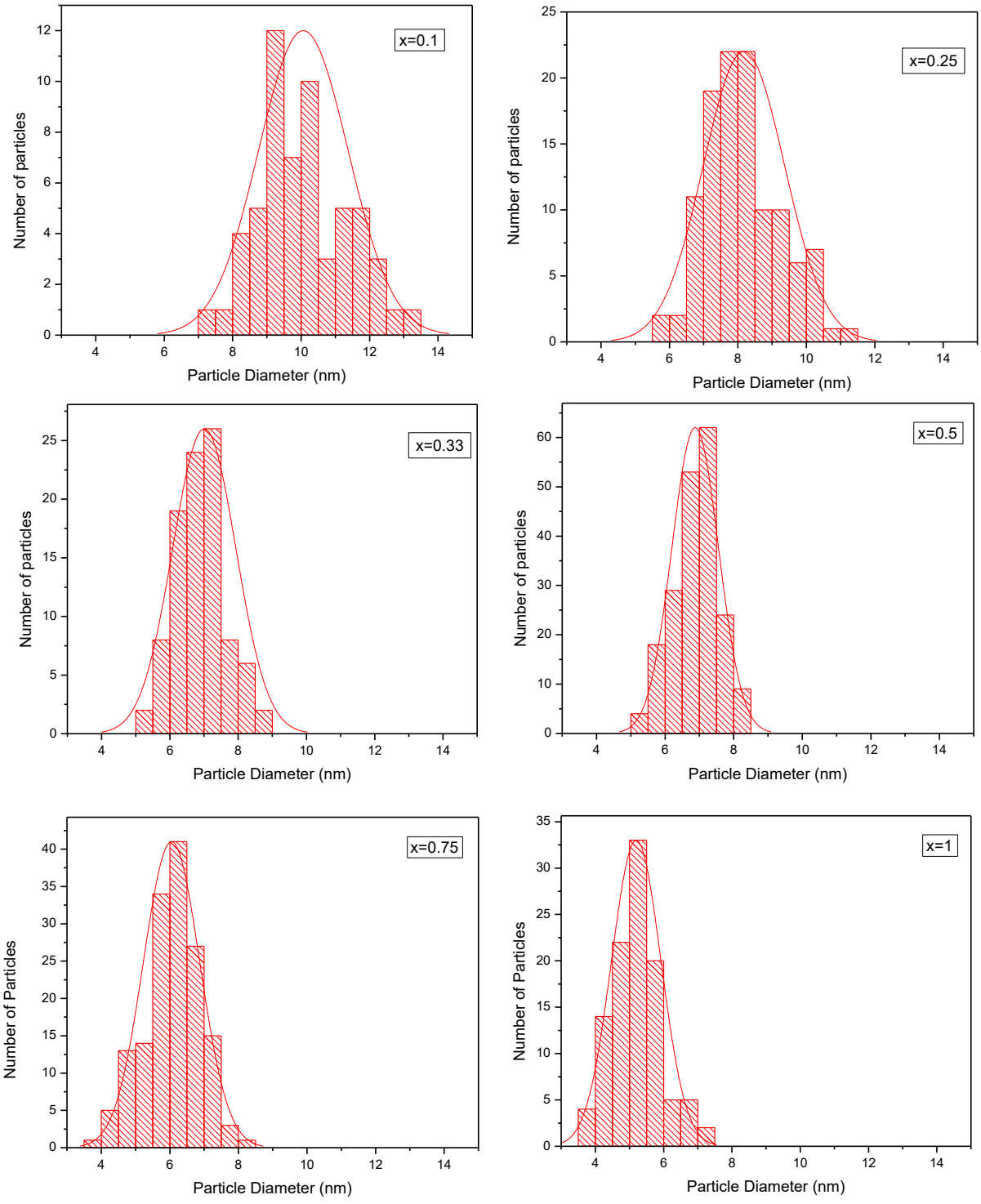

Figure 4.7. Particle size histograms for different $Ni_{2-x}Ru_xP$ compositions.

In order to further confirm the formation of a solid solution of the three components, line scanning and elemental mapping data were collected using scanning transmission electron microscopy (STEM). As shown in Figure 4.8 for a $Ni_{1.25}Ru_{0.75}P$ particle, all three elements are homogeneously distributed, consistent with formation of a solid solution between the three elements.

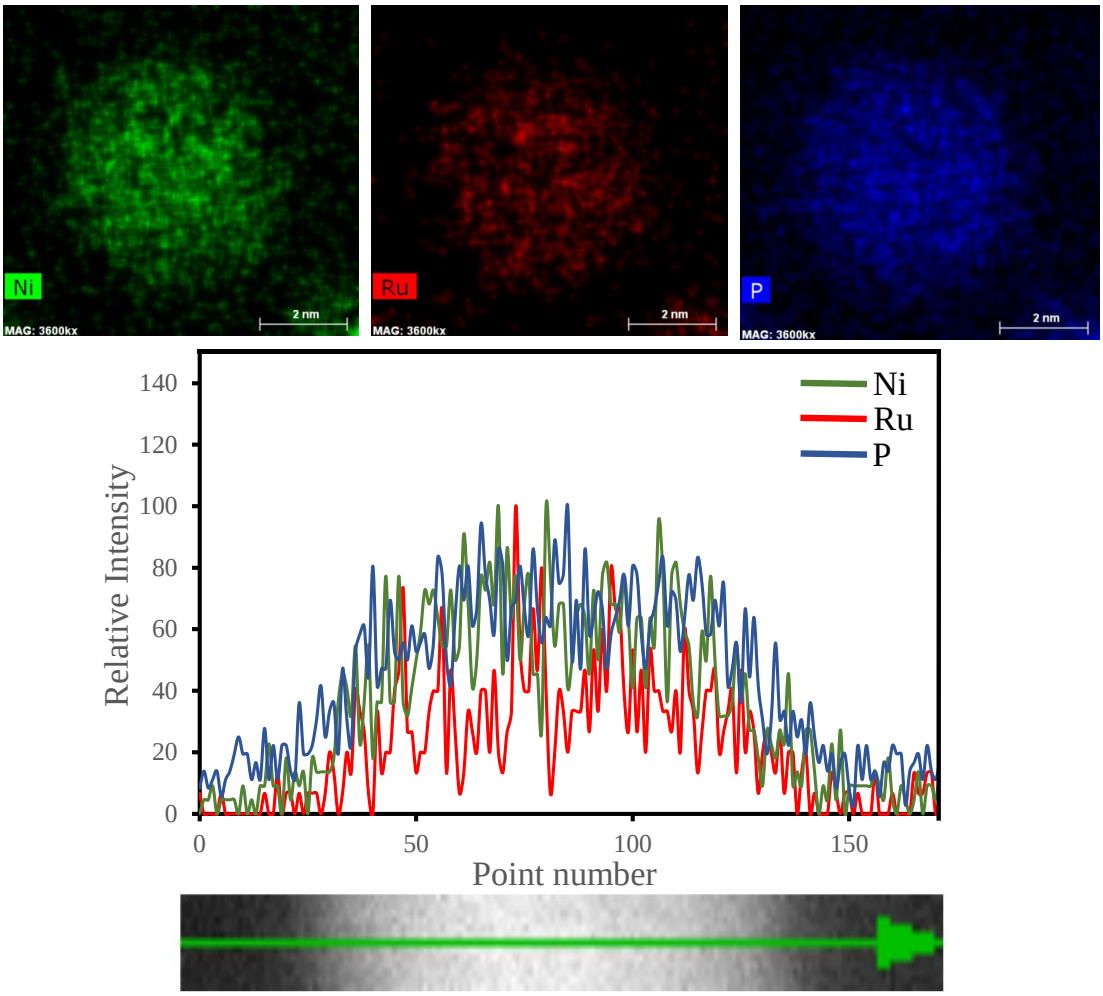

Figure 4.8. Elemental mapping and line scanning data for a $Ni_{1.25}Ru_{0.75}P$ particle.

4.3.2.2 Attempts to prepare Ru-rich compositions of $Ni_{2-x}Ru_xP$ nanoparticles (x>1)

Samples targeting compositions x>1 (x=1.25, x=1.5) were prepared according to Scheme 4.1. As shown in Figure 4.9, the PXRD patterns are indicative of amorphous phases without any discernible crystalline peaks that can be indexed to either Ni_2P or Ru_2P phases. As shown in the corresponding TEM images, the samples consist of worm-like particles, similar to the morphology for crystalline Ru nanoparticles and amorphous Ru_2P (Figure 4.1). ICP-MS data yielded compositions of $Ni_{0.82}Ru_{1.18}P_{1.4}$ and $Ni_{0.65}Ru_{1.35}P_{1.3}$ for x=1.25 and 1.5, respectively. Reflecting our ability to target the desired composition. We speculate that the reaction temperatures used in our system (limited by the solvent) are not sufficient to crystallize the Ru-rich $Ni_{2-x}Ru_xP$ phases.

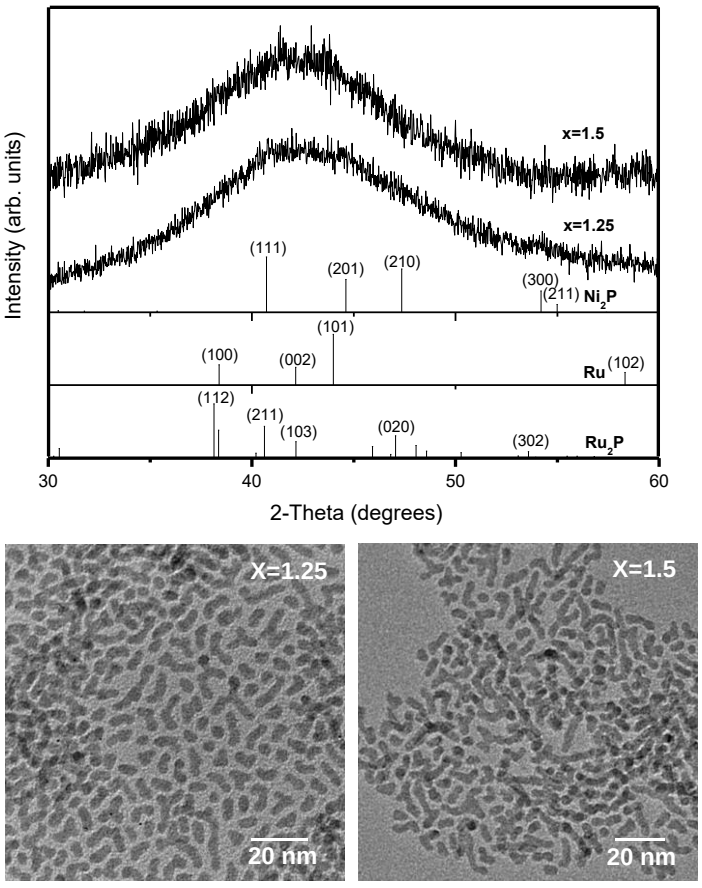

Figure 4.9. PXRD patterns and TEM images of Ru rich compositions (x=1.25, 1.5) prepared by the protocol given in Scheme 4.1

4.3.3 Oxygen evolution reaction (OER) catalytic activity of $Ni_{2-x}Ru_xP$ nanoparticles

To evaluate the effect of incorporating Ru on Ni_2P OER catalysts, catalytic activity was evaluated for selected $Ni_{2-x}Ru_xP$ compositions. Ni_2P nanocrystals were also prepared as benchmark catalysts using a published method[16] as are Ru:P~2 ($Ru_2P_{1.2}$) materials. Figure 4.10 shows the polarization curves obtained for different compositions in 1 M KOH solution. Overpotentials were calculated based on the voltage required to produce a current density of 10 mA/cm^2 for each composition. Ni_2P nanoparticles of ~11 nm in diameter (Figure 4.12) show an overpotential value of 0.44 V. This is somewhat lower than that reported in previous work by Pingwu Du and coworkers, for Ni_2P particles with sizes ranging from 20-50 nm (0.50 V for catalyst loading 0.1 mg/cm^2, 1.0 M KOH).[92] Intriguingly, Ru_2P, which we expected might be the most active catalyst based on activities demonstrated by RuO_2 and Ru metal, is the least active. It is not clear whether this is an effect of phosphidation, a consequence of the amorphous nature of Ru_2P, or both. For other $Ni_{2-x}Ru_xP$ compositions, we observed a decrease in overpotential with increasing the Ru amount and this trend was maintained up to x=0.75 (Figure 4.11) where the lowest overpotential value was obtained (0.34 V). This performance is comparable to that reported by Shu-Hong Yu and coworkers for RuO_2 (0.37 V), the state of the art catalyst, in 0.1 M KOH (although our data are collected at higher $[OH^-]$, 1.0 M).[135]

The presence of a "sweet spot" near the 50:50 Ni:Ru stoichiometry, where activity is maximized relative to the binary phases, may be due to synergism between the metal centers. Alternatively, assuming one metal is acting as the preferential catalytic site, the activity may be related to the site geometries, square pyramidal vs. tetrahedral, where the metals do not form true solid solutions but exhibit strong site preferences. Because there is a 1:1 ratio of the two sites, at $x \leq 1$ there is the possibility of complete site segregation of, for example, Ru on square pyramidal

sites, whereas for x>1, mixing of Ru over both sites is necessary. A third prospect, possibly in conjunction with heterogeneous site occupancies, is that the second metal may be acting to electronically activate the catalytic metal (via transfer of electron density). Additionally, under catalytic conditions, the surface is expected to oxidize (as noted in other phosphides), so the nature of the active catalyst is expected to have phosphate or hydroxide moieties.[91, 92, 136, 137]

While the data presented here is insufficient to assess the presence of synergism (both Ru and Ni playing an active role in a bimetallic catalytic site), or site preferences (non-homogeneous occupation of Ru and Ni in the square pyramidal or tetrahedral site), there are clear indications of electronic activation of Ni by Ru. In the Ni_2P polarization curve in Figure 6 there is a current maxima taking place around 1.52 V. This peak corresponds to the $Ni^{II}/Ni^{III/IV}$ oxidation of Ni, as reported in previous work. This peak was observed in all other compositions ($x \leq 1$) but shifts to lower potentials with increasing Ru. This observation suggests the redox properties of Ni are modified, making Ni easier to oxidize as Ru is incorporated. Since $Ni^{III/IV}$ is purported to be the active species for OER in $Ni(OH)_2$,[138] the ease Ni oxidation may be responsible for the lower overpotentials noted in Ru-incorporated materials.

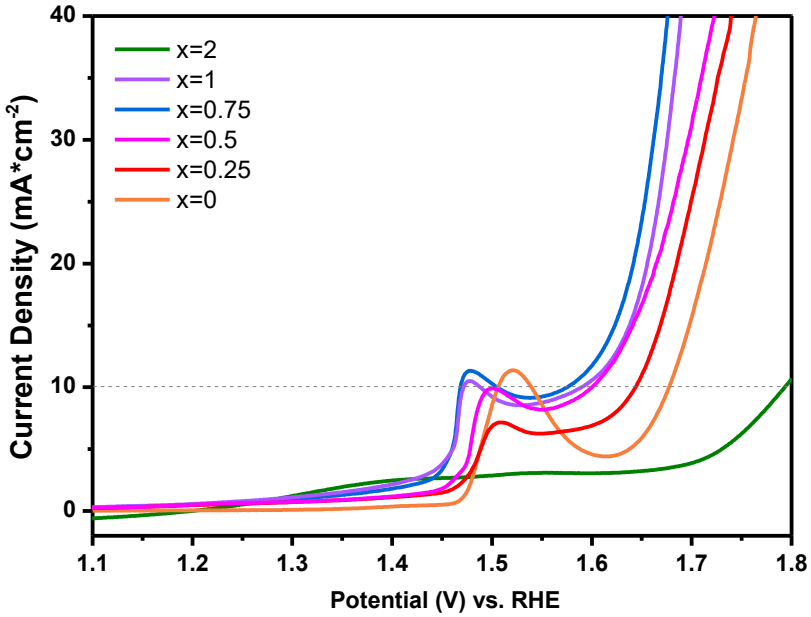

Figure 4.10. Polarization curves for different compositions of $Ni_{2-x}Ru_xP$ nanoparticles in 1.0 M KOH

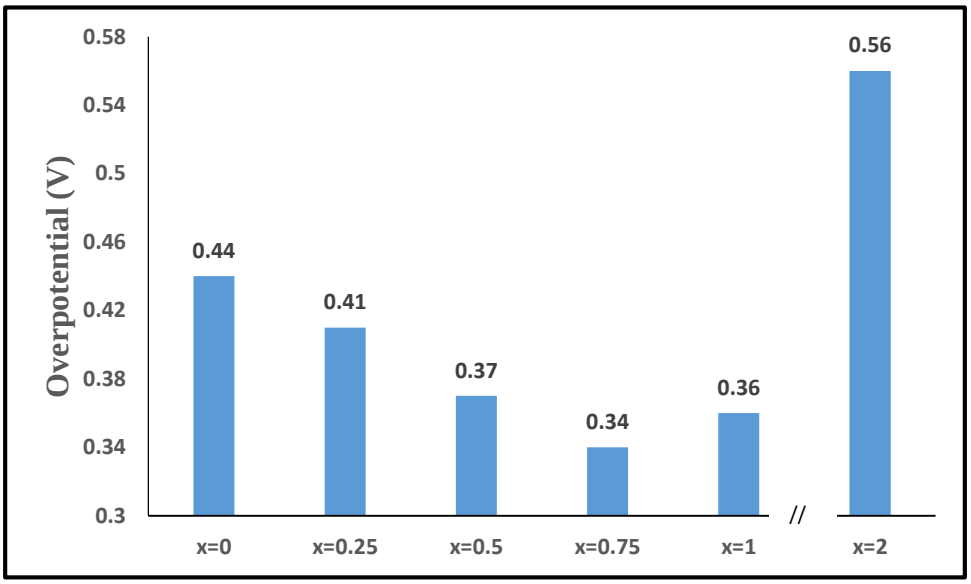

Figure 4.11. Change in overpotential (at 10 mA/cm^2) for different compositions of $Ni_{2-x}Ru_xP$ in 1.0 M KOH

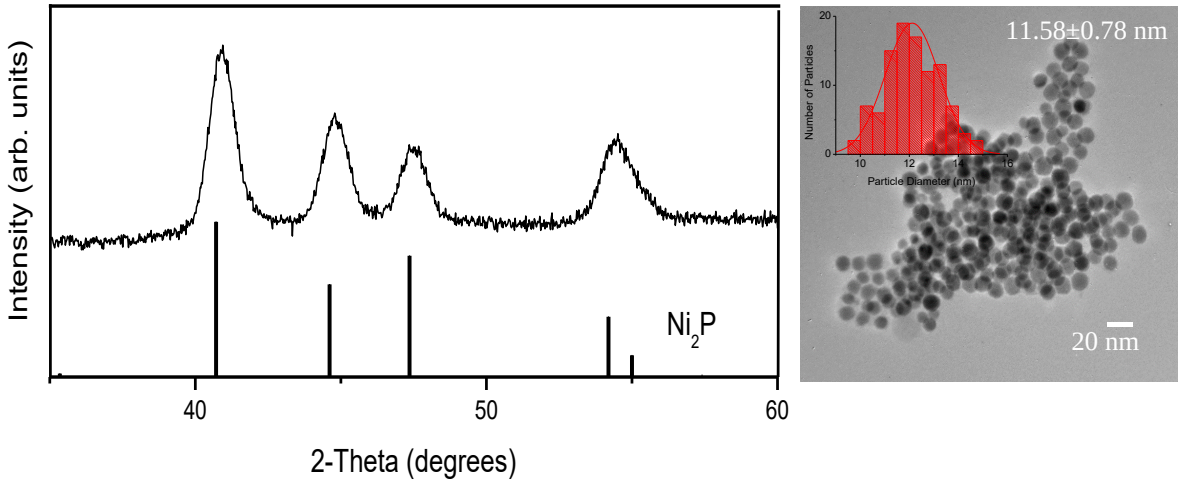

Figure 4.12. PXRD pattern and TEM image for Ni_2P particles prepared for OER catalytic testing.

4.4 Conclusions

Solution-phase arrested-precipitation reactions have been developed to prepare crystalline $Ni_{2-x}Ru_xP$ nanoparticles up to $x \leq 1$ as narrow polydispersity samples and with excellent composition control. There is a clear dependency of size (5-10 nm) and morphology (spherical vs elongated) on Ru concentration, and Ru-rich compositions ($x>1$) are amorphous. It was observed amorphous Ru_2P phase could be crystallized by annealing at high temperatures (450 ^oC). $Ni_{2-x}Ru_xP$ nanoparticles proved effective OER catalysts with optimum activity at $x=0.75$ (overpotential = 0.34 V, 1.0 M KOH). Although RuO_2 is considered to be a state-of-the-art catalyst, the Ru_2P phosphide, at least in our hands, exhibited the poorest performance (0.56 V) suggests that either the crystallinity of the materials plays a vital role in the catalytic activity, or electronic effects at high Ru loadings diminishes activity. It is clear that the redox characteristics of Ni metal are modified with the introduction of Ru, as has been observed in other bimetallic phosphides, $Ni_{2-x}Fe_xP$ and $Ni_{2-x}Co_xP$,[74, 139] contributing to the lower activation barrier for OER. Present studies are focused on elucidating site preferences in $Ni_{2-x}Ru_xP$ to discern whether the activity trends reflect

inhomogeneities in the site distributions, and crystallizing Ru-rich phases by reductive annealing to determine the contributions of structure and electronics to catalyst activity. The availability of $Ni_{2-x}Ru_xP$ nanoparticles opens the door for the composition-dependent study of other processes, such as hydrotreating studies, which are presently underway.

CHAPTER 5 PROBING HYDRODESULFURIZATION CATALYTIC ACTIVITY OF $NI_{2-X}M_XP$ (M=CO, RU) NANOPARTICLES ENCAPSULATED IN MESOPOROUS SILICA[3]

5.1 Introduction

With the increasing demand for low sulfur fuels, metal phosphides have become widely studied as catalysts in hydrodesulfurization (HDS) process. Recently, research has focused on bimetallic ternary phosphides to obtain better activity via the synergetic interaction of two metals. The Bussell group reported that ternary phosphides of Ni_2P incorporating a small amount of Co or Fe show better HDS catalytic activity compared to the binary counterparts when prepared by the TPR method on Silica.[69, 71] However, the inhomogeneous nature of the TPR prepared materials is disadvantageous for understanding how surface characteristics and size contribute to the activity. The Brock group reported the evaluation of size- dependent HDS catalytic activity of Ni_2P nanoparticles prepared by solution phase routes. In this study it was revealed when the nanoparticles are incorporated onto a support by the common incipient wetness method they undergo significant sintering under HDS conditions. As a remedy, an approach was developed to encapsulate nanoparticles in a mesoporous silica matrix that could retain the size and phase of the particles.[54] This enabled size-dependent studies of HDS catalytic activity.

In the present study HDS catalytic activity for Ni-rich $Ni_{2-x}Co_xP$ and $Ni_{2-x}Ru_xP$ compositions encapsulated in mesoporous silica was evaluated. Preparation of nanoparticles, encapsulation in the silica matrix, and characterization of encapsulated materials for phase, morphology, and surface area was done by me at Wayne State University. Further characterization of the catalyst and evaluation of HDS catalytic activity was carried out by the group of Prof. Mark E Bussell at Western Washington University.

[3] Portions of the text in this chapter were reprinted or adapted with permission from: Surface Science. 2016, 648, 126-135

5.2 Experimental

5.2.1 Preparation of $Ni_{2-x}Co_xP$ and $Ni_{2-x}Ru_xP$ nanoparticles

Nanoparticles were prepared as described in Chapter 3 and 4.

5.2.2 Encapsulation of nanoparticles in mesoporous silica

As-prepared nanoparticles were dispersed in 5 mL of chloroform and added drop-wise to 20 mL of an aqueous 0.1 M CTAB solution. This solution was heated at 75-80 °C in order to evaporate all the chloroform while phase transfer of the nanoparticles from the organic to the aqueous phase takes place. The resultant dispersion was diluted to a final volume of 150 mL with nanopure water and 2.5 mL of 1 M NaOH was added, followed by drop wise injection of 4.6 mL of TEOS to initiate the base-catalyzed polymerization. The reaction was completed within 20 -30 minutes and the silica particles were isolated by centrifugation. The isolated product was washed with water and methanol three times to remove residual NaOH and ethanol formed as the by-product. The purified product was dried in an active vacuum overnight. The dried product was calcined in air at 425 °C for 2-3 h to remove the CTAB. The oxide material formed during calcination was converted back to the phosphide by treatment with PPh_3 (or NaH_2PO_2) placed up-stream in a furnace under active flow of 5% H_2/Ar at 400 °C.

Scheme 5.1. Protocol for the encapsulation of nanoparticles in mesoporous silica

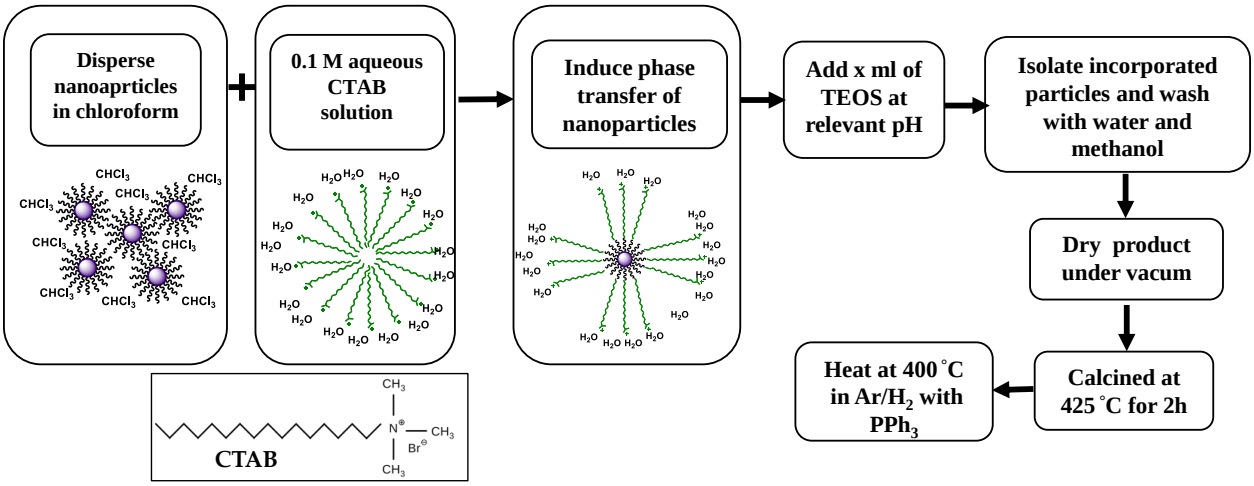

5.2.3 Characterization of the catalyst

The metal phosphide loadings (wt%) of the encapsulated samples were evaluated using ICP-MS based on the total metal content (assuming a 2:1 stoichiometry of metal:P) by ICP-MS (Agilent 7700). The samples (2 mg) were digested in concentrated nitric acid (5 mL) over 3-4 days and diluted 48x with nano pure water. A series of external standards were used for calibration over the relevant concentration range. Surface area and pore size distributions for encapsulated silica samples were collected using a Micromeritics Tristar II surface area/porosimeter. All samples were degassed for 16 h at 423 K under N_2 flow before the analysis. Surface areas were calculated based on the Brunauer – Emmett- Teller (BET) multimolecular adsorption method and pore size distributions were obtained by the Barrett- Joyner- Halenda (BJH) method. Carbon monoxide (CO) pulsed chemisorption measurements were also obtained using a Micromeritics Autochem 2950 instrument equipped with a thermal conductivity detector. Approximately 0.1000 g of catalyst was degassed in 60 mL/min Ar at room temperature for 30 min. Prior to the measurements, the samples were reduced in a 60 mL/min flow of 10.0 mol% H_2/Ar (Praxair) by heating (10 K/h) from room

temperature to 673 K and holding at this temperature for 1 h. The catalyst samples were then degassed in 60 mL/min He at 673 K for 30 min prior to the chemisorption measurement. The CO chemisorption measurements were performed by pulsing a 10.0 mol% CO/He mixture (0.6080 mL loop volume) into 60 mL/min of He flowing over the catalyst sample, which was held at 273 K. Pulsing was carried out until the peak areas of three consecutive pulses remained unchanged, after which the chemisorption capacity was calculated.

The IR spectroscopic experiments were conducted in an ion pumped (110 L/s) ultra-high vacuum (UHV) system that has a base pressure of ~ 5 x 10^{-9} Torr. The UHV system, which has been described in detail elsewhere,[140] includes a high-pressure cell outfitted with CaF_2 windows that can be isolated from the main chamber. The system is equipped with a Mattson RS-1 FTIR spectrometer outfitted with a narrow-band MCT detector; the high pressure cell is situated in the sample compartment of the spectrometer and IR spectra are collected in transmission mode. Catalyst samples were mounted in the UHV system following the procedure described previously.[140] Briefly, ~10 mg of the catalyst was pressed at 14 MPa into a nickel metal mesh (50 x 50 mesh size, 0.002 in. wire diameter); the area of the pressed samples was ~0.80 cm^2. A chromel-alumel thermocouple was spot-welded to the nickel mesh in order to monitor the temperature of the sample. This assembly was then mounted onto a sample holder equipped with resistive heating. Following mounting in the UHV system, the catalyst samples were evacuated overnight to a pressure $\leq 10^{-8}$ Torr. The catalyst samples were then reduced *in situ* in 100 Torr H_2 for 30 min at four different temperatures of 475, 575, 650 and 700 K. In order to remove weakly bonded species from the surface of the reduced catalysts, the high pressure cell was then evacuated and the sample heated to the reduction temperature for 1 min.

Transmission FTIR spectra were acquired in the 4000-1000 cm^{-1} range by collecting 128 scans at 2 cm^{-1} resolution. To eliminate the contributions of gas phase CO in the IR spectra, the sample spectrum was ratioed against a spectrum acquired using a blank nickel mesh mounted in the sample holder in the presence of 1.0 or 5.0 Torr CO. Following pretreatment and degassing, the catalyst sample was cooled to room temperature at a pressure of ~ 1 x 10^{-8} Torr and a background IR spectrum was acquired. IR spectra of adsorbed CO were then collected at 298 K while the catalyst sample was in the presence of 1.0 and 5.0 Torr CO, and then in UHV following evacuation of the gas phase CO. The IR spectra presented in the figures were prepared by subtracting the background IR spectrum obtained prior to CO exposure from the IR spectrum acquired after CO exposure.

Following HDS measurements, samples of the catalysts were collected for X-ray diffraction and bulk carbon and sulfur analyses. Upon completion an HDS experiment, the flow of liquid feed was stopped while maintaining the H_2 gas flow for 1 h at the reaction temperature. The reactor was then cooled to room temperature, depressurized, and then purged with 60 mL/min He for 30 min. The system was then opened and allowed to sit for a minimum of 3 h to permit the slow exposure of the catalyst to ambient air. Bulk carbon and sulfur analyses of HDS-tested catalyst samples were carried out using a LECO SC-144DR Sulfur and Carbon Analyzer. Approximately 0.10 g of catalyst was transferred into a ceramic boat, which was then loaded into a furnace where the sample was combusted in an oxygen-rich environment at ~1625 K for 3 min. Combusted carbon (CO_2) and sulfur (SO_2) that evolved from the catalyst sample was quantified via IR detection and reported as wt% C and S. An additional ~0.05 g sample of the HDS-tested catalysts was used to acquire an X-ray diffraction pattern as described above.

5.2.4 HDS activity measurements

HDS activity measurements were carried out using a fixed-bed, continuous flow reactor operating at a total pressure of 3.0 MPa and temperatures in the range 548-648 K. The reactor feed consisted of a decalin solution containing 3000 ppm DBT (1000 ppm 4,6-DMDBT) and 500 ppm dodecane, with the latter used as an internal standard for gas chromatographic analysis of the reactor effluent. The liquid feed (5.4 mL/h) was injected into a 100 mL/min flow of hydrogen and vaporized in-line prior to entry into the reactor. Approximately 0.15 g of catalyst (16-20 mesh size) was diluted with quartz sand to a total volume of 5 mL and loaded into a reactor tube having a diameter of 1.1 cm and length of 40 cm. The reactor temperature was measured with a thermocouple mounted axially in the reactor tube that was in direct contact with the catalyst bed. Encapsulated catalysts were pretreated by heating from room temperature to 673 K in 1 h in a 60 mL/min flow of H_2 and held at this temperature for 2 h, then cooled to room temperature in continued H_2 flow. The He (Airgas, 99.999 mol%) and H_2 (Airgas, 99.999 mol%) were passed through molecular sieve and O_2 removal traps prior to use.

Following pressurization of the reactor with H_2 to 3 MPa, the catalyst was heated to 548 K in 100 mL/min H_2 over 30 min after which the flow of liquid feed was begun. The reactor was stabilized for approximately 12 h prior to sampling the reactor effluent at 30 min intervals over 2 h. The catalyst temperature was then raised 25 K, the reactor stabilized for 3 h, followed by sampling of the reactor effluent at 30 min intervals for 2 h. This procedure was repeated until sampling at the maximum catalyst temperature (648 K) was completed. The samples of the liquid reactor effluent from the three types of HDS activity measurements were analyzed off-line using a gas chromatograph (Agilent 6890N) equipped with an HP-5 column and a flame ionization detector.

5.3 Results and Discussion

5.3.1 Evaluation of DBT HDS catalytic activity of $Ni_{2-x}Co_xP$ nanoparticles

5.3.1.1 Characteristics of the encapsulated $Ni_{2-x}Co_xP$ catalysts

Three different targeted compositions (x=0.08, 0.25, 0.5) of $Ni_{2-x}Co_xP$ were synthesized[21] and as shown in Figure 5.1 these materials adopt Ni_2P structure with nearly monodisperse particles. Before the catalytic testing these particles were encapsulated in a mesoporous silica matrix to maintain the stability under HDS conditions. Encapsulated materials were further characterized for phase and morphology. As shown in Figure 5.2, after the encapsualation all compostions retain the Ni_2P structure type with no evident impurities. The crystallite size calculated from Scherrer equation varies from 11-13 nm as shown in Table 5.1.

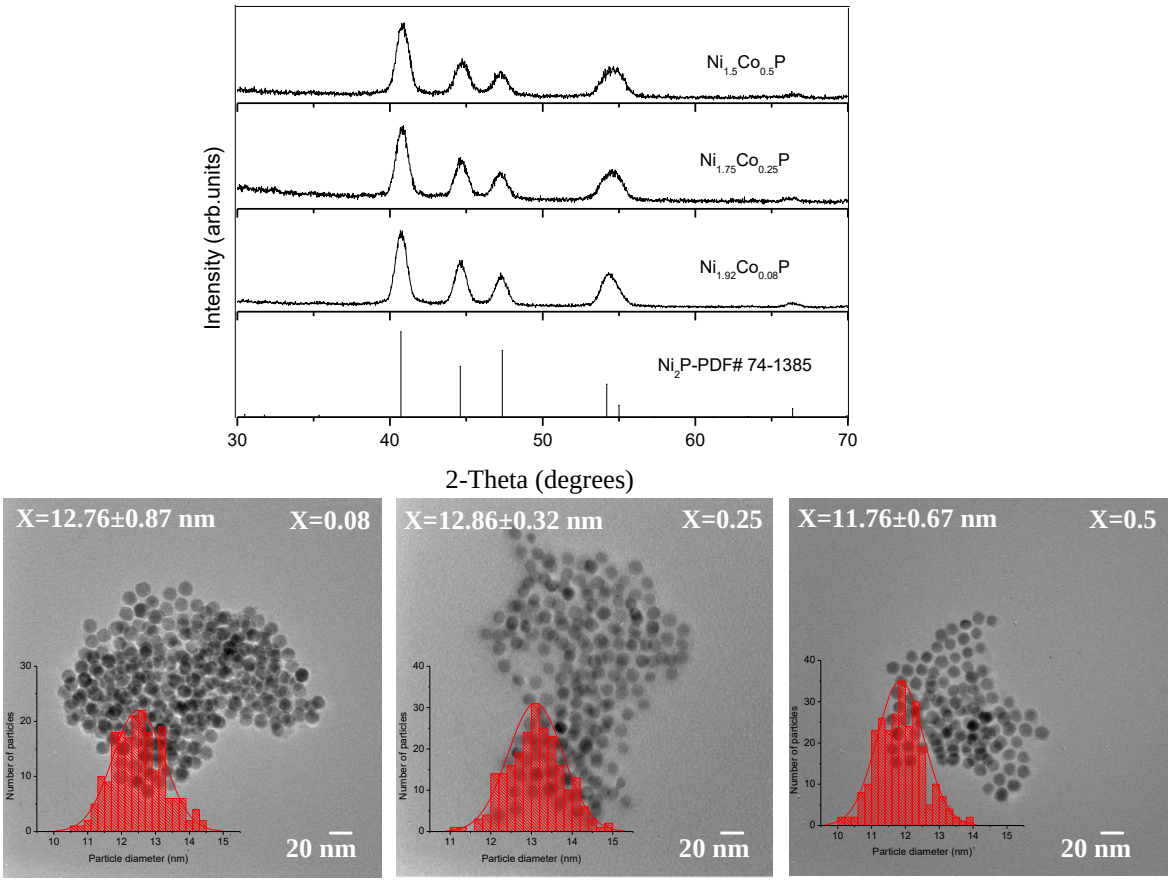

Figure 5.1. PXRD patterns and TEM images of the as prepared $Ni_{2-x}Co_xP$ nanoparticles for HDS catalytic testing. Insets show particle size distributions

The TEM images of the encapsulated materials in Figure 5.2 show the dispersion of nanoparticles (small dark spheres) in the mesoporous silica matrix. High resolution TEM (HRTEM) images for as-prepared nanoparticles are shown as insets in each TEM image. Lattice planes were observed for all compositions, indicating the crystalline nature of these materials and d-spacing for the observed lattice planes was approximately 0.5 nm. This corresponds to the (100) set of planes in the Ni_2P structure. The Miller indices were assigned for observed facets of a particle with the $Ni_{1.5}Co_{0.5}P$ composition. As shown in Figure 5.3, the (001) plane is exposed on the surface of the particle. This is purported to be the crystallite plane of Ni_2P that is most active for HER and HDS proposed by DFT studies.[141, 142] The surface area and pore size distribution analysis for each sample were evaluated before testing for the catalytic activity. Figure 5.4 illustrates nitrogen physisorption isotherms and pore size distributions (calculated from adsorption branch of the isotherm) for tested samples. The BET surface areas and average pore sizes for the $Ni_{2-x}Co_xP@mSiO_2$ nanocatalysts are given in Table 5.1. The surface areas of the nanocatalysts are over 400 m^2/g, suggesting the high porosity of the SiO_2 matrix surrounding the nanoparticles. The average pore diameters exist in the range 3.4-5.3 nm. The pore size of the material is a critical factor; too small pores might inhibit the molecule accessing the catalyst surface and too large pores might not able to trap the catalyst inside the silica matrix.

The catalyst loading (mass %) of these silica encapsulated samples were evaluated using ICP-MS. Metal phosphide loading for all compositions vary in the range 10-12 wt% of the silica sample (Table 5.1).

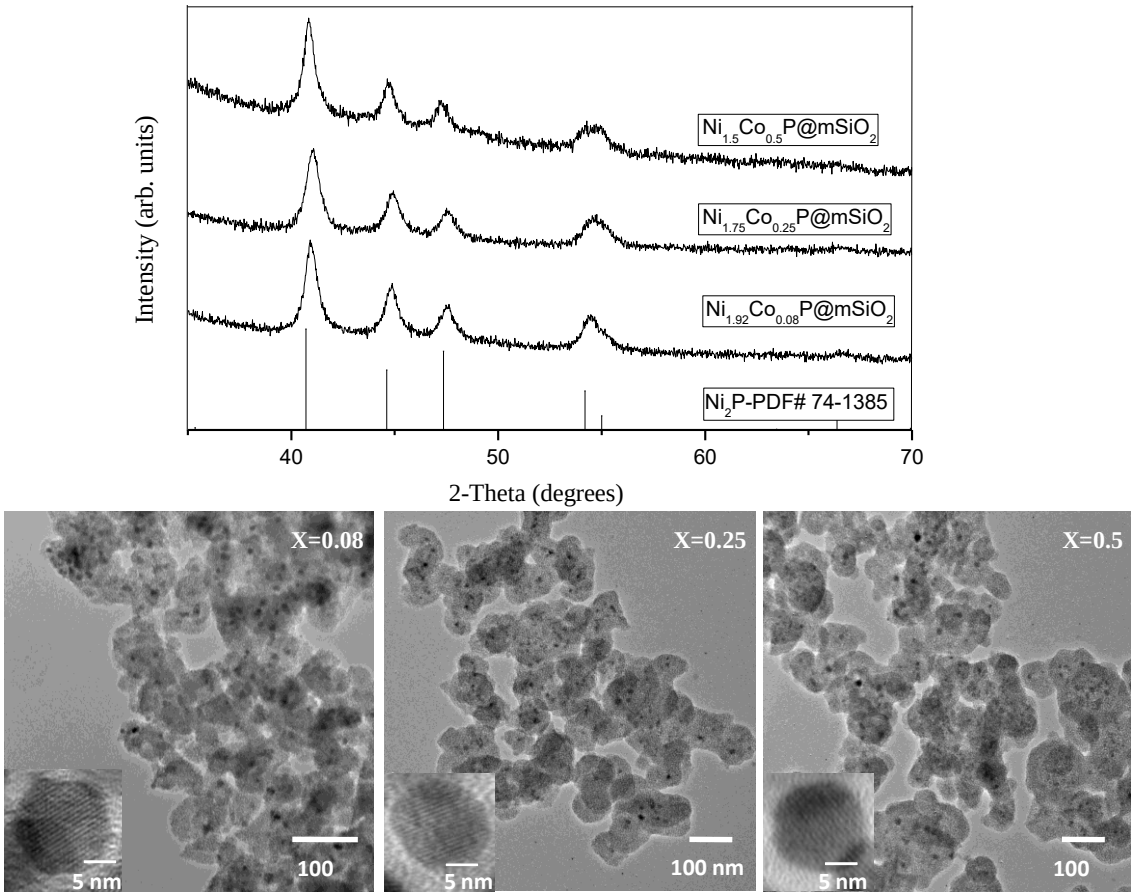

Figure 5.2. PXRD patterns and TEM images of the encapsulated nanoparticles. Insets show HRTEM image for a representative particle for each composition with lattice fringes

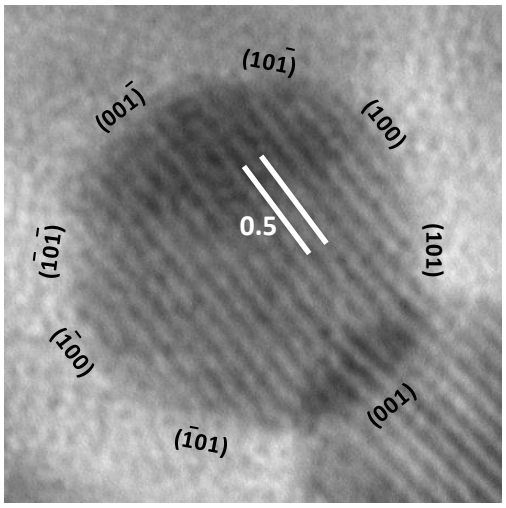

Figure 5.3. HRTEM image of a $Ni_{1.5}Co_{0.5}P$ nanoparticle showing lattice fringes corresponding to exposed (100) planes with 0.5 nm spacing and the {100}, {001} and {101} sets of facets.

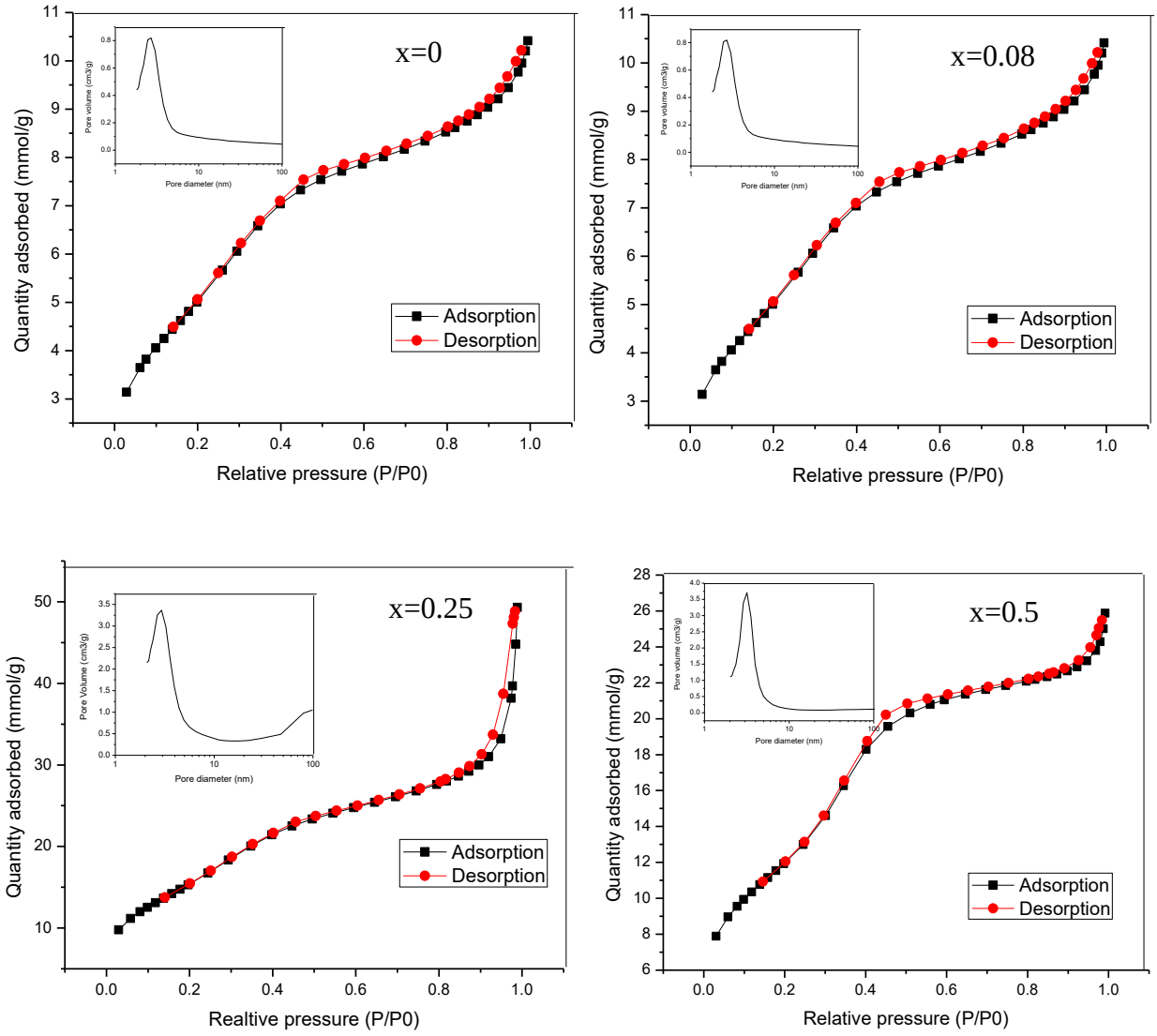

Figure 5.4. Nitrogen adsorption-desorption isotherms for the $Ni_{2-x}Co_xP@mSiO_2$ nanocatalysts. The inset depicts the pore size distribution calculated from the adsorption branch of the isotherm.

Table 5.1. Physicochemical data for the $Ni_{2-x}Co_xP@mSiO_2$ nanocatalysts

Nanocatalyst	Metal phosphide Loading (wt%)	Bulk Composition	Average Crystallite Size (nm)	BET Surface Area (m^2/g)	BJH average pore diameter (nm)
$Ni_2P@mSiO_2$	10.5	$Ni_{2.00}P_{1.08}$	12	410	3.5
$Ni_{1.92}Co_{0.08}P@mSiO_2$	11.2	$Ni_{1.89}Co_{0.11}P_{1.10}$	13	938	5.3
$Ni_{1.75}Co_{0.25}P@mSiO_2$	9.80	$Ni_{1.72}Co_{0.28}P_{1.06}$	11	1270	5.3
$Ni_{1.50}Co_{0.50}P@mSiO_2$	11.6	$Ni_{1.46}Co_{0.54}P_{1.12}$	13	903	3.4

CO can be used as a probe molecule to assess the accessibility of molecules to the catalyst surface. All the compositions show CO chemisorption capacities indicating some exposure of the catalyst surface, despite the presence of a mesoporous silica shell around the nanoparticles (Table 5.2). These chemisorption capacities can be used as a measure of the number of active sites present on the catalyst surface. As shown in Table 5.2, except for the $Ni_{1.92}Co_{0.08}P@mSiO_2$ nanocatalyst, the CO chemisorption capacities exhibited a decreasing trend with increased Co content. These results are consistent with trends in O_2 chemisorption capacities reported previously for TPR-prepared $Ni_{2-x}Co_xP/SiO_2$ catalysts.[71]

Table 5.2. Dibenzothiophene HDS catalytic data for the $Ni_{2-x}Co_xP@mSiO_2$ nanocatalysts

Nanocatalyst	CO Chemisorption Capacity (μmol/g)	DBT HDS Activity (nmol DBT/g·s)	TOF (s^{-1})
$Ni_2P@mSiO_2$	17	89	0.0052
$Ni_{1.92}Co_{0.08}P@mSiO_2$	25	117	0.0047
$Ni_{1.75}Co_{0.25}P@mSiO_2$	13	85	0.0065
$Ni_{1.50}Co_{0.50}P@mSiO_2$	9	79	0.0088

To evaluate the electronic nature of the active sites of the catalysts, IR spectra of adsorbed CO on the nanocatalysts (T = 298 K, P_{CO} = 1.0 Torr) were collected and are shown in Figure 5.5. The IR spectrum corresponding to CO on the $Ni_2P@mSiO_2$ sample is similar to the spectrum reported previously for a Ni_2P/SiO_2 catalyst (T=298 K, P_{CO} = 5.0 Torr).[143] Two peaks are apparent at 2097 and 2202 cm^{-1} that are assigned to CO terminally bonded on surface Ni and P sites, respectively. A slight rise in the background is discernable at ~1915 cm^{-1} that is associated with CO bridge bonded to Ni sites; this mode of CO adsorption is suppressed on Ni_2P as surface P atoms disrupt adjacent Ni sites needed for the formation of bridge-bonded CO species. The IR spectrum of adsorbed CO provides conclusive evidence that Ni and P sites on the encapsulated Ni_2P nanoparticles are accessible to molecules from the gas phase. Evacuation of the CO gas results in the disappearance of the ν_{CO} assigned to CO adsorbed on P sites, but the ν_{CO} absorbance assigned to CO terminally bonded to Ni sites persists. The IR spectrum of adsorbed CO on the $Ni_{1.50}Co_{0.50}P@mSiO_2$ nanocatalyst shows evidence for a second absorbance in the form of a shoulder in the 2040-2060 cm^{-1} region that may be indicative of CO adsorption on surface Co sites on this sample.[118] Incorporation of Co into the Ni_2P lattice to form $Ni_{2-x}Co_xP$ results in a shift of the ν_{CO} absorbance for Ni terminally bonded CO to lower wavenumbers (2097 $\rightarrow$ 2089 cm^{-1}) , with the extent of the shift dependent on the amount of Co in the bimetallic phosphide phase. This shift with increasing the amount of Co is consistent with electronic donation from Co to Ni in the nanocatalysts. Increased electron density on Ni sites would enable increased backbonding between Ni and the CO molecule, resulting in a weakening of the CO bond. Oyama and coworkers observed a similar trend in ν_{CO} absorbances for a series of $Ni_{2-x}Fe_xP/SiO_2$ catalysts and came to a similar conclusion.[74] Shifts observed for XPS binding energies and XANES absorption edges for bulk Ni_{2-}

$_{x}Co_{x}P$ materials are also consistent with a slight transfer of electron density from Co to Ni in these bimetallic phosphides.[119]

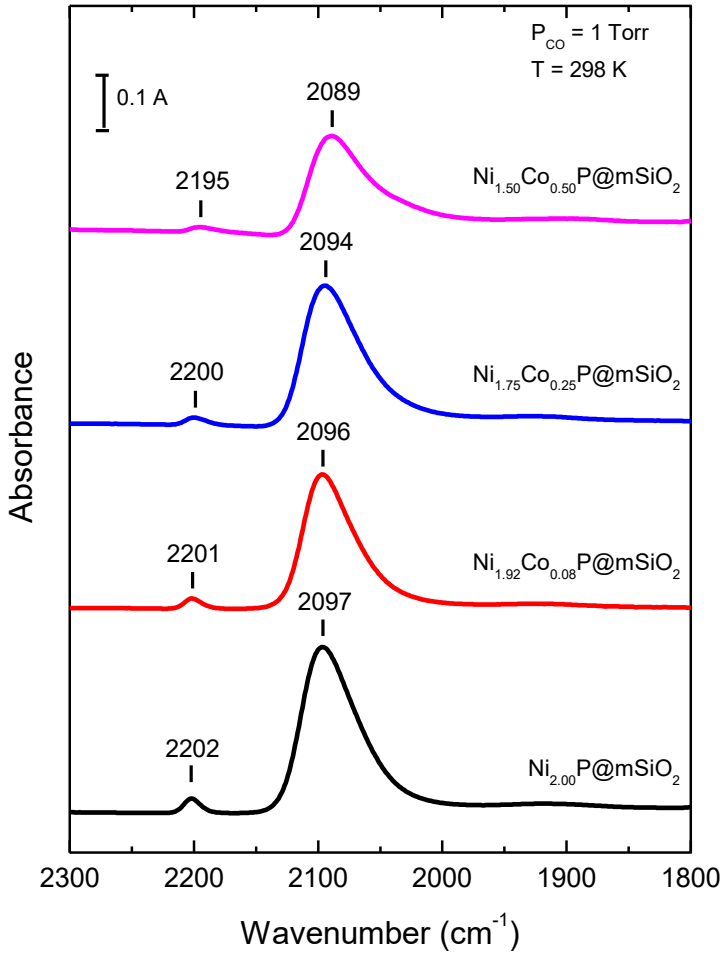

Figure 5.5. Infrared spectra of adsorbed CO on $Ni_{2-x}Co_{x}P@mSiO_2$ nanocatalysts

5.3.1.2 HDS catalytic activity and selectivity of $Ni_{2-x}Co_{x}P@mSiO_2$ catalysts

Dibenzothiophene conversions as a function of reaction temperature are plotted in Figure 5.7 for the $Ni_{2-x}Co_{x}P@mSiO_2$ nanocatalysts over the temperature range 548-648 K. The $Ni_{2-x}Co_{x}P@mSiO_2$ nanocatalysts exhibit measureable DBT conversions at or above 548 K, confirming earlier findings that the active sites on the nanoparticle surfaces are accessible to the reactant molecules. The DBT HDS activities (calculated based on DBT conversion to hydrocarbon products) at 623 K for all of the $Ni_{2-x}Co_{x}P@mSiO_2$ nanocatalysts investigated are listed in Table

5.2. The $Ni_{1.92}Co_{o0.08}P@mSiO_2$ nanocatalyst was the most active (on a mass catalyst basis) of the different compositions investigated; in general, the DBT conversions and HDS activities decreased with increasing Co content. At 623 K, the $Ni_{1.92}Co_{0.08}P@mSiO_2$ was 31% more active for DBT HDS than $Ni_2P@mSiO_2$ when the activities are normalized on a mass of catalyst basis. This result is consistent with a study of $Ni_{2-x}Co_xP/SiO_2$ catalysts in which a $Ni_{1.92}Co_{0.08}P/SiO_2$ catalyst prepared from a P-enriched precursor (P/(Ni+Co) = 0.80) was the most active catalyst for thiophene HDS, with an activity 34% higher than that of Ni_2P/SiO_2 catalyst prepared from a precursor having P/Ni = 0.80.[71] A similar finding was observed for unsupported phases, as a nominal composition of Ni_2 $Co_{0.08}P$ was found to have an activity 67% higher than that of Ni_2P for the HDS of 4,6-DMDBT.[72] In both studies, it was concluded that the small amount of Co in the bulk and supported $Co_{0.08}Ni_2P$ resulted in surface enrichment in P; this enrichment may due to a restructuring of the surface of the metal phosphide particles that results in a higher proportion of Ni in M(2) sites than in Ni_2P. The $Ni_{1.92}Co_{0.08}P@mSiO_2$ nanocatalyst had a significantly higher CO chemisorption capacity than $Ni_2P@mSiO_2$ (25 vs. 17 μmol/g) that could be a result of a surface restructuring that yields more exposed Ni sites at the surface of the nanoparticles. With increased Co content, the HDS activities and CO chemisorption capacities of the $Ni_{2-x}Co_xP@mSiO_2$ nanocatalysts decrease monotonically as the surface concentration of Co increases, which mirrors the trend observed for silica-supported $Ni_{2-x}Co_xP/SiO_2$ catalysts prepared by the TPR method.[71]

The DBT HDS turnover frequencies (TOFs), calculated using the CO chemisorption capacities as the measure of active site densities, are listed in Table 5.2 and plotted in Figure 5.7 as a function of Co content. For the calculation of the TOFs, only one molecule of CO adsorbed per Ni site is assumed. The TOFs exhibit an increasing trend as the amount of Co in the $Ni_{2-x}Co_xP$

nanoparticles increases, which is the opposite trend observed for the HDS activities. Thus, while the HDS activities (on a mass basis) decrease with increasing Co content, the CO chemisorption capacities decrease more quickly, resulting in the increasing trend for the TOFs. The nanocatalyst with the highest Co content $Ni_{1.50}Co_{0.50}P@mSiO_2$ has the highest TOFs of 0.0088 s^{-1}. This TOF is nearly twice the value for $Ni_2P@mSiO_2$ (0.0052 s^{-1}). Increased electron density on Ni sites, as observed by our IR studies, may facilitate key steps in the HDS process such as the dissociation of H_2 and the adsorption of organosulfur molecules.[74]

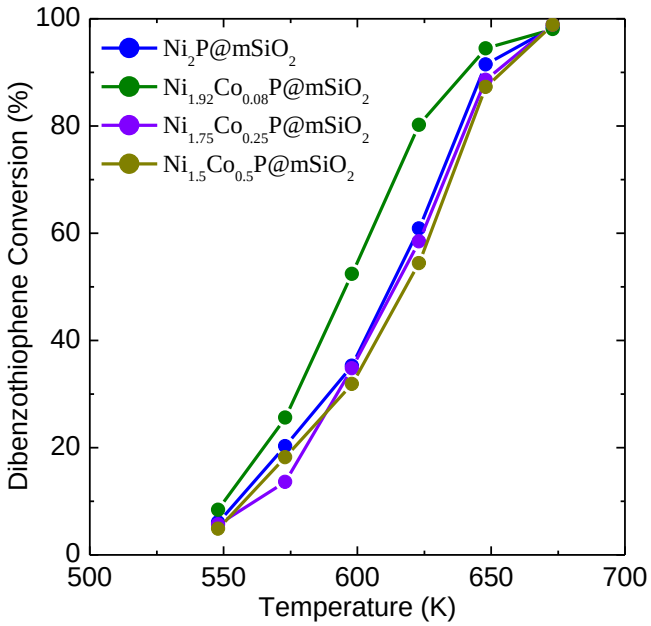

Figure 5.6. Dibenzothiophene HDS conversion vs. temperature for $Ni_{2-x}Co_xP@mSiO_2$ nanocatalysts

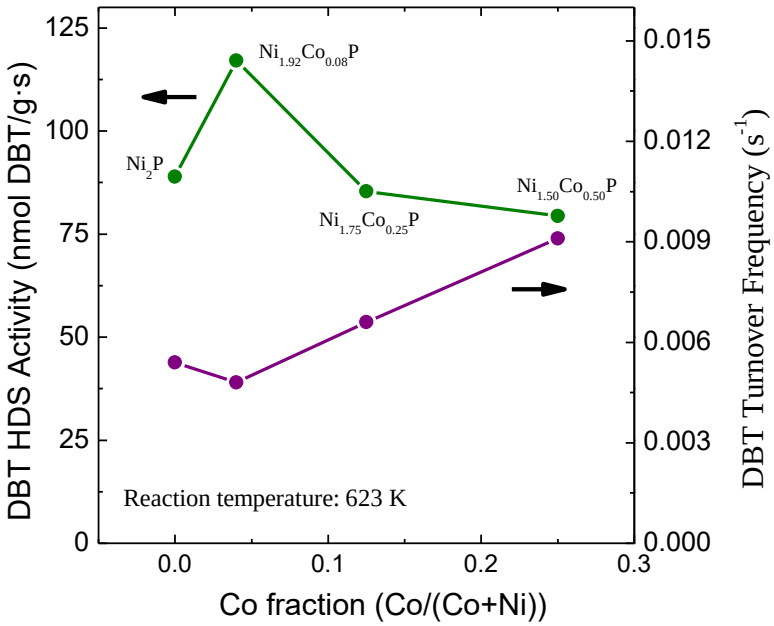

Figure 5.7. Dibenzothiophene HDS TOFs vs. Co content for $Ni_{2-x}Co_xP@mSiO_2$ nanocatalysts.

There are two pathways by which sulfur removal can take place in the HDS of DBT, as shown in Scheme 5.2. This reaction network was determined from a study that used a sulfided Co-Mo catalyst supported on Al_2O_3.[144] The direct desulfurization (DDS) pathway involves hydrogenolysis of the C-S bonds directly, not disturbing the aromatic rings and produces biphenyl (BP) as the final product. In the hydrogenation pathway (HYD) one or both aromatic rings are hydrogenated prior to the C-S bond hydrogenolysis and produce cyclohexylbenzene (CHB) and bicyclohexane (BCH) as final products. The DBT HDS product selectivities as a function of reaction temperature for $Ni_2P@mSiO_2$ and $Ni_{1.5}Co_{0.5}P@mSiO_2$ nanocatalysts are plotted in Figure 5.8 (a) and (b), and the selectivities for all of the compositions at 623 K are listed in Table 5.3. Regardless of the amount of Co the major product for all of the nanocatalysts investigated was BP, which is consistent with results reported previously for TPR-prepared Ni_2P/SiO_2 and $Ni_{1.97}Fe_{0.03}P/SiO_2$ catalysts.[69] As shown for a $Ni_2P@SiO_2$ nanocatalyst in Figure 5.6, the BP selectivity was consistently ~80% over the entire temperature range 548-648 K. The only significant changes in the product selectivity

with temperature are for partially hydrogenated tetrahydrodibenzothiophene (4H-DBT) and CHB. 4H-DBT comprises ~10% of the products at 548 K, but reduces to zero by 648 K. In contrast, CHB product selectivity increases with temperature, occupying 5% at 548 K and increasing to 18% of the products by 648 K. BCH, the fully hydrogenated product maintains consistent selectivity accounting for less than 3% of the products at all temperatures. As shown in Figure 5.8(b) the $Ni_{1.5}Co_{0.5}P@mSiO_2$ composition follow the same trend in product selectivity for all temperatures. As shown in Table 5.3 regardless of the amount of Co, all compositions consist of a similar proportion of products at 623 K.

Scheme 5.2. Dibenzothiophene HDS reaction network

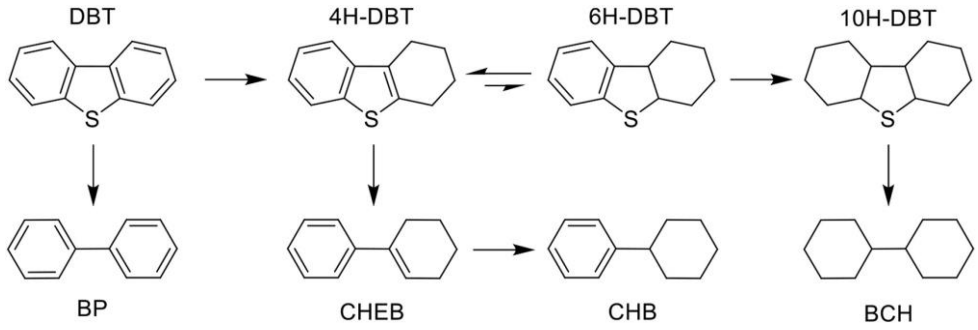

Table 5.3. Dibenzothiophene HDS product selectivities at 623 K for different $Ni_{2-x}Co_xP@mSiO_2$ catalysts

Catalyst	4H-DBT	BP	CHB	BCH
$Ni_2P@mSiO_2$	1.6	80.5	17.3	0.7
$Ni_{1.92}Co_{0.08}P@mSiO_2$	1.7	80.8	16.6	0.9
$Ni_{1.75}Co_{0.25}P@mSiO_2$	1.4	80.2	17.6	0.8
$Ni_{1.50}Co_{0.50}P@mSiO_2$	2.4	79.7	17.2	0.7

Further with respect to catalyst characterization, post-HDS tested samples were evaluated for size, sulfur and carbon content. As shown is Figure 5.9 PXRD patterns for the tested samples show sizes similar to the pre-HDS catalysts without any obvious impurities, indicating the stability of encapsulated particles under HDS conditions. As shown in Table 5.4 a minimal amount of sulfur has incorporated during HDS testing suggesting the strong resistance of these catalysts to convert to metal sulfides in sulfur-rich feed

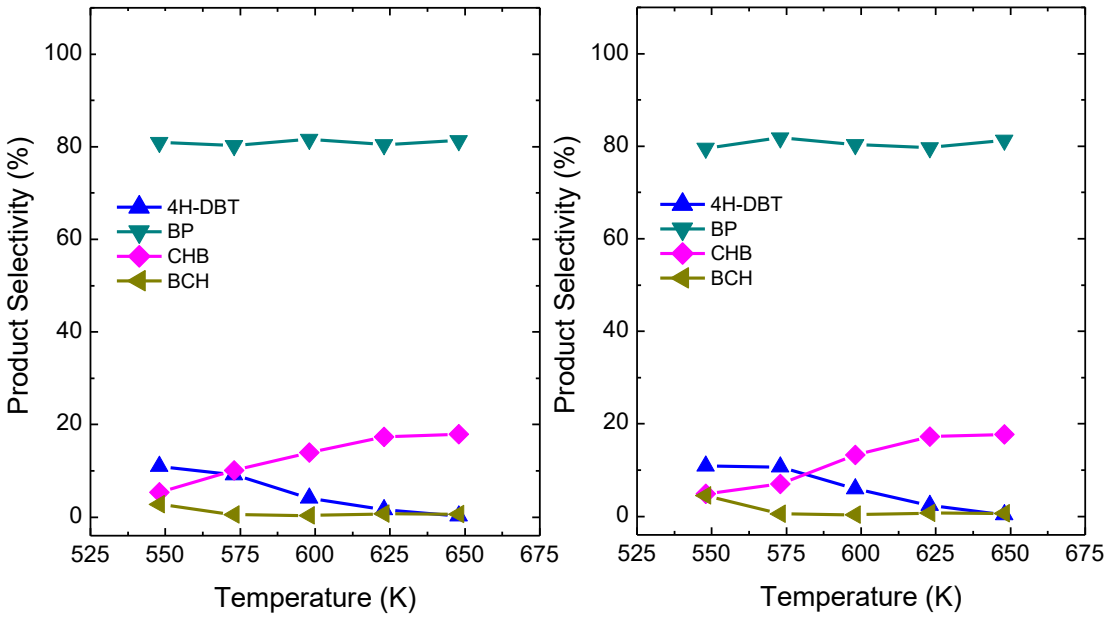

Figure 5.8. Dibenzothiophene HDS product selectivities vs. temperature for (a) $Ni_2P@mSiO_2$ and (b) $Ni_{1.50}Co_{0.50}P@mSiO_2$ nanocatalyst.

Table 5.4. Carbon and sulfur analyses for post HDS catalysts

Catalyst	Wt% Carbon	Wt% Sulfur	S/M mole ratio
$Ni_2P@mSiO_2$	1.183	0.122	0.029
$Ni_{1.92}Co_{0.08}P@mSiO_2$	0.893	0.114	0.024
$Ni_{1.75}Co_{0.25}P@mSiO_2$	1.058	0.132	0.032
$Ni_{1.50}Co_{0.50}P@mSiO_2$	1.793	0.145	0.029

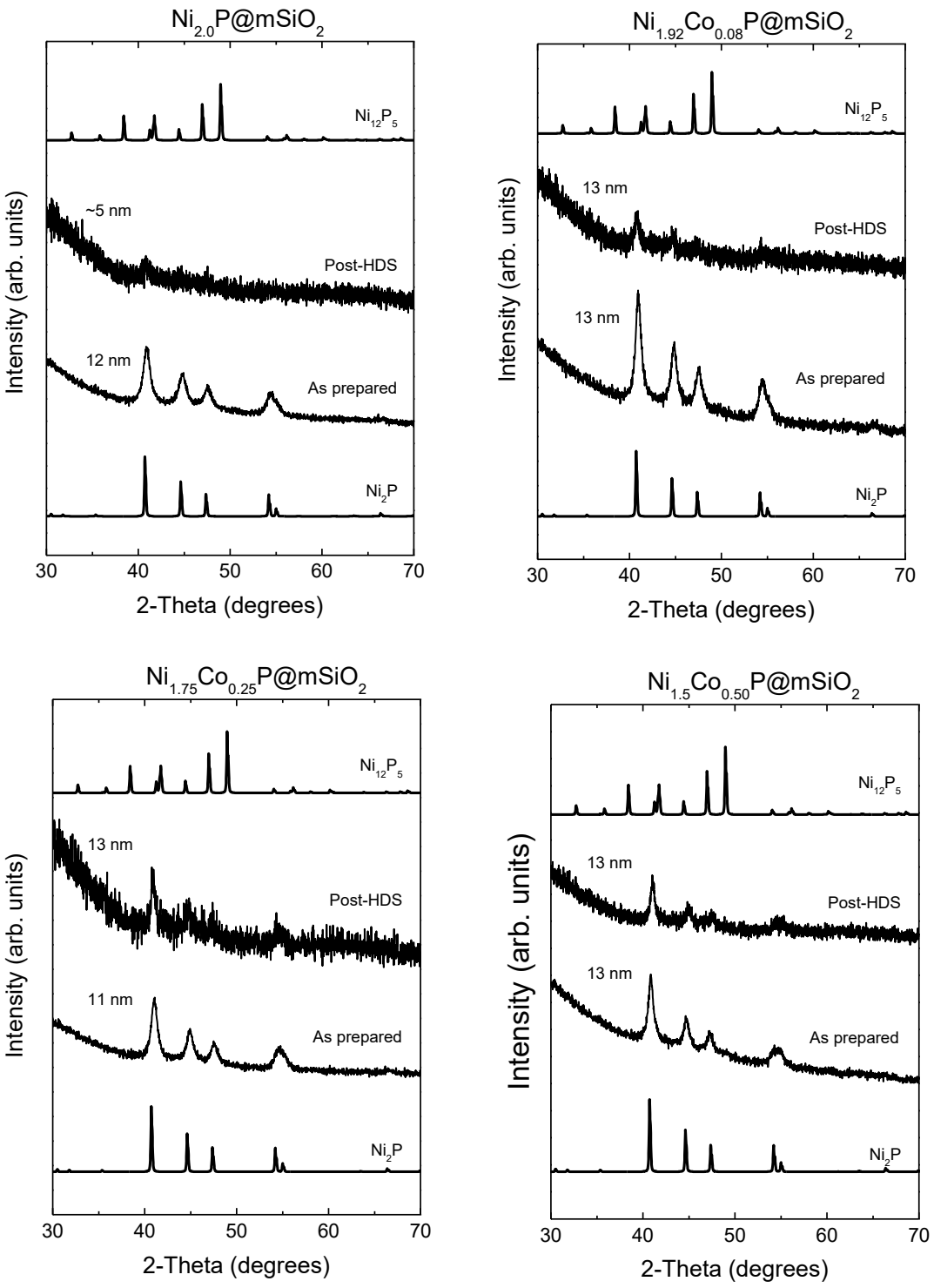

Figure 5.9. PXRD patterns for the post-HDS tested catalysts

5.3.2 Evaluation of 4,6-DMDBT HDS catalytic activity of $Ni_{2-x}Ru_xP$ nanoparticles

5.3.2.1 Encapsulation of $Ni_{2-x}Ru_xP$ nanoparticles in mesoporous silica

Three compositions of $Ni_{2-x}Ru_xP$ nanoparticles (x=0.1, 0.25, 0.5) were selected and the same procedure given in Section 5.2.2 for $Ni_{2-x}Co_xP$ nanoparticles was followed for the encapsulation process, except in this case sodium hypophosphite (NaH_2PO_2) was used as the P source in the reduction step. In an elemental analysis of these encapsulated materials it was revealed the amount of carbon added to the catalyst during the reduction step is little higher with PPh_3 compared to NaH_2PO_2 (Table 5.5). Accordingly, NaH_2PO_2 was adopted as the P source in the reduction step for $Ni_{2-x}Ru_xP$ materials.

Table 5.5. Carbon analysis for the material reduced with two different P sources

P source	C (wt %)
PPh_3	**1.57**
NaH_2PO_2	**0.37**

During the reduction step for $Ni_{2-x}Ru_xP$ materials it was revealed that depending on the composition, the final phase is very sensitive to the amount of P source used, in contrast what was observed for Ni_2P and $Ni_{2-x}Co_xP$ materials. In the case for x=0.1, absence of the P source resulted in $Ni_{12}P_5$ phase as an impurity and about 0.5 g of NaH_2PO_2 was required to get rid of this impurity phase. For x=0.25 composition, 0.1 g of phosphite was sufficient to get rid of the $Ni_{12}P_5$ phase. In the presence of a higher amount of phosphite (0.5 g), RuP_2 phase was observed as an impurity. For x=0.5 composition no P source was required to produce phase pure materials and in the presence of a very tiny amount of P source (0.1 g) RuP_2 was observed as an impurity. These data suggest the loss of phosphorus during calcination and reduction steps was strongly compositional

dependent and the redox properties of the metals are modified due to the metallic interaction in ternary phase.

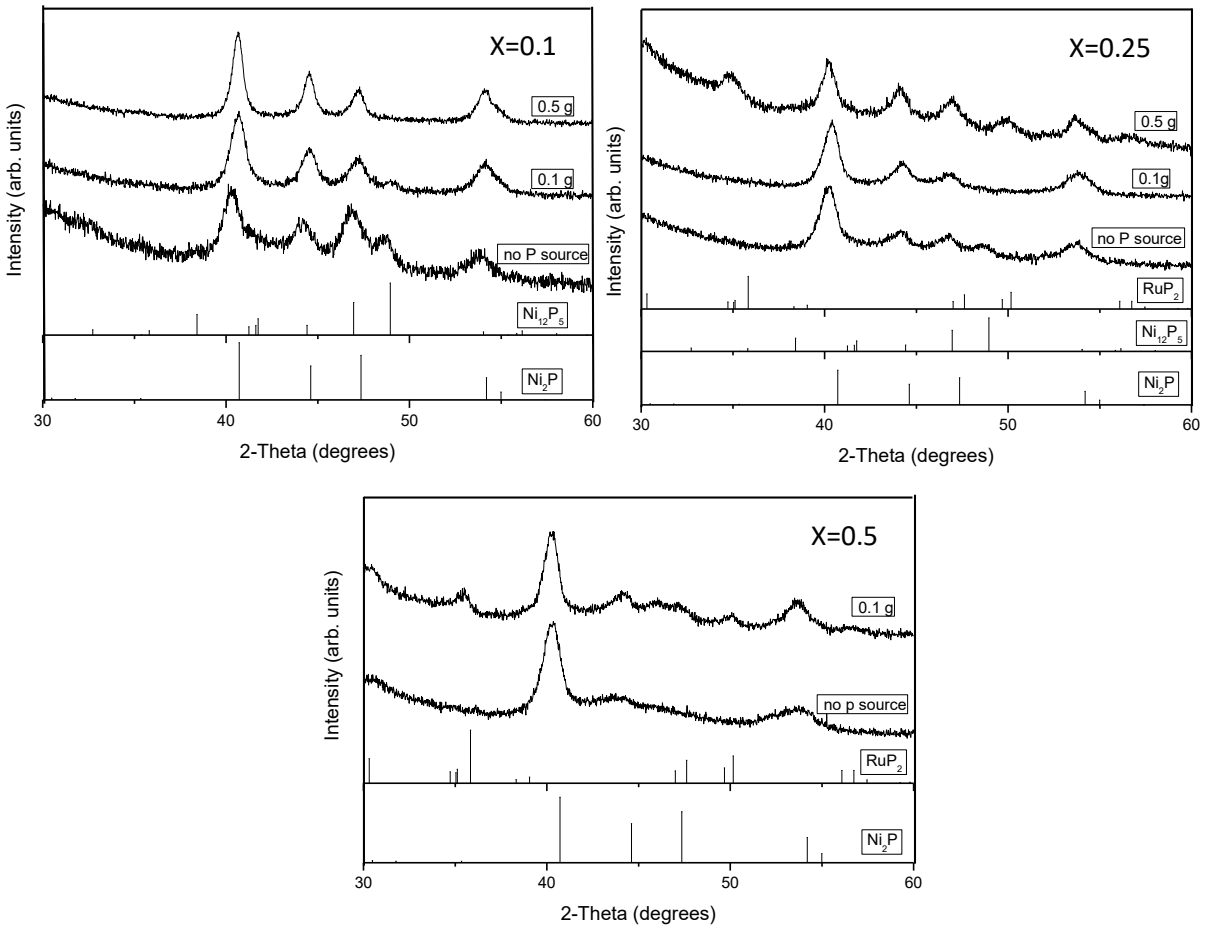

Figure 5.10. PXRD patterns for the encapsulated $Ni_{2-x}Ru_xP$ materials reduced with different amounts of P source

5.3.2.2 Characterization of the encapsulated $Ni_{2-x}Ru_xP$ catalysts

The encapsulated nanoparticles were analyzed for phase, morphology, surface area and pore size. Figure 5.11 shows the PXRD patterns of the encapsulated materials adopting the Ni_2P structure. From the TEM images it was evident the nanoparticles (dark spheres) evenly dispersed in the silica matrix. From the PXRD patterns the particle sizes were calculated and vary in the size range 9-11 nm. All compositions show large surface area (900-1100 m^2/g) with pore sizes lie in

the range 3-3.2 nm. ICP-MS was used to analyze the weight loading of the catalyst and the data are given in Table 5.6. Chemisorption capacities were evaluated using CO as the probe molecule and values varied from 23-31 μmol/g without a clear trend as a function of composition.

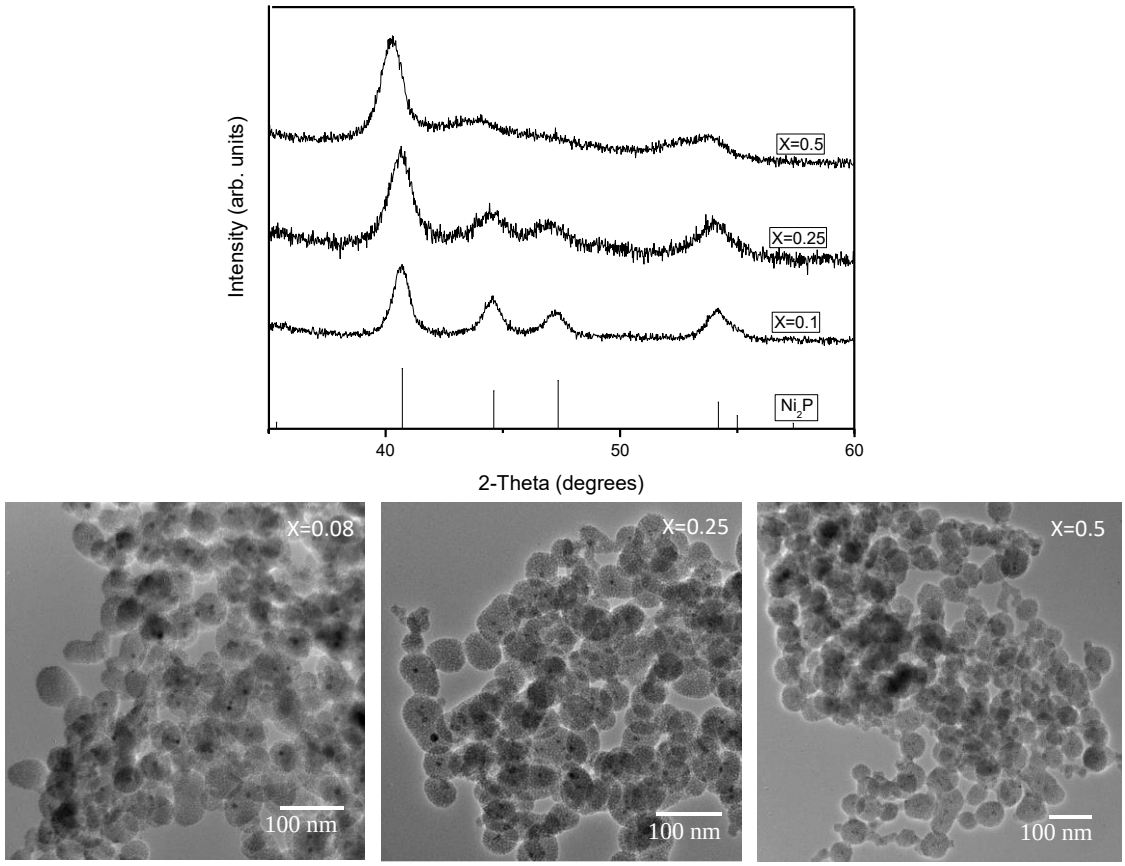

Figure 5.11. PXRD patterns and TEM images of the encapsulated $Ni_{2-x}Ru_xP$ nanoparticles.

Table 5.6. Physicochemical data for the $Ni_{2-x}Ru_xP@mSiO_2$ nanocatalysts

Composition	Crystallite size (nm)	BET surface area (m^2/g)	Pore diameter (nm)	Sample loading (wt%)	CO chemisorption capacity (μmol/g)
Ni_2P	10	1086	3.1	8.8	31
$Ni_{1.9}Ru_{0.1}P$	11	877	3.2	9.4	27
$Ni_{1.75}Ru_{0.25}P$	9	1043	3.0	7.9	23
$Ni_{1.5}Ru_{0.5}P$	9	921	3.2	9.1	30

5.3.3 4,6-DMDBT HDS catalytic activity and product selectivity of $Ni_{2-x}Ru_xP$ nanoparticles

4.6-DMDBT (a refractory sulfur compound) HDS catalytic activity was evaluated for the encapsulated materials and conversions normalized on a mass catalyst basis (10 wt%) for different temperatures (510-630 K) are given in Figure 5.12. Surprisingly we observed conversion decreases smoothly with increasing Ru content except for $Ni_{1.75}Ru_{0.25}P$. The highest conversion is shown by Ni_2P for all temperatures, while the highest Ru incorporated (x=0.5) composition shows very low activity relative to other compositions despite its higher chemisorption capacity.

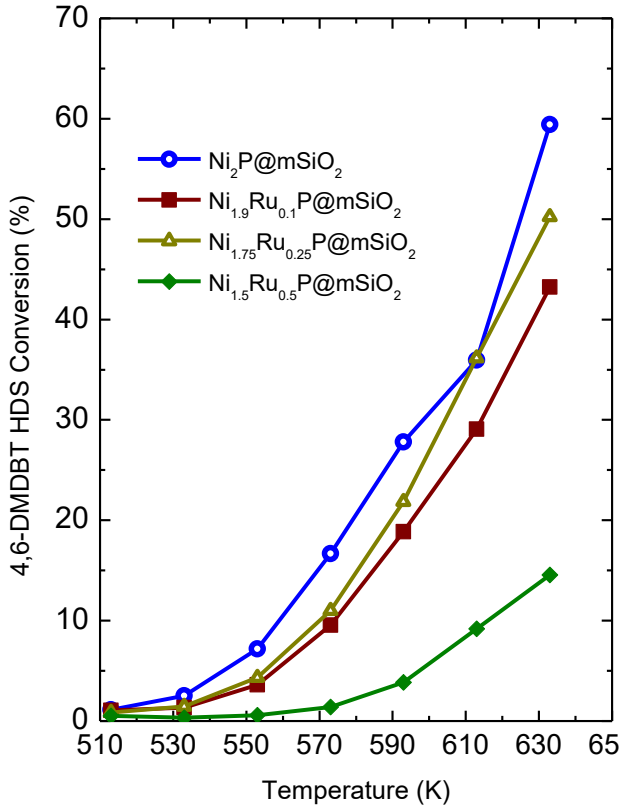

Figure 5.12. 4,6-dimethyldibenzothiophene HDS conversion vs T for $Ni_{2-x}Co_xP@mSiO_2$ nanocatalysts

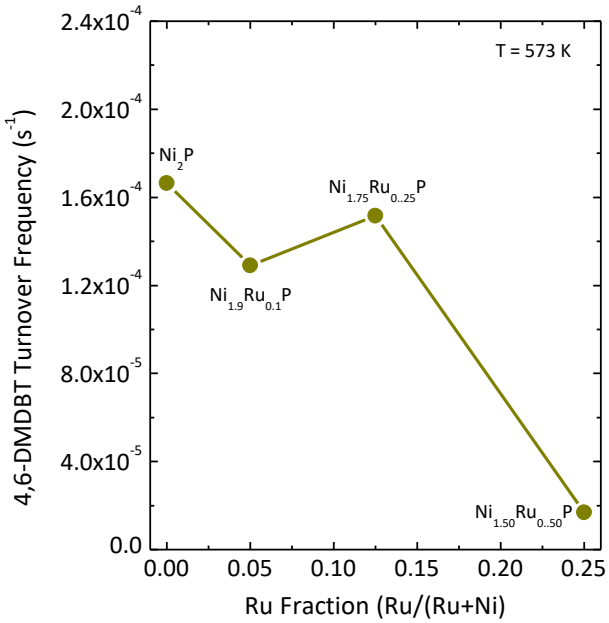

Figure 5.13. 4,6-dimethyldibenzothiophene HDS TOFs vs. Ru content for $Ni_{2-x}Ru_xP$@$mSiO_2$ nanocatalysts.

Figure 5.13 shows the turnover frequency (TOFs) values calculated based on activity (at 573 K) and chemisorption capacities given in Table 5.6. Since the chemisorption values are pretty similar for all compositions the trend in TOFs for 4,6-DMDBT mirrors the HDS activity. The trend we observed for TOFs of $Ni_{2-x}Ru_xP$ compositions is very different from what we observed for our $Ni_{2-x}Co_xP$ and $Ni_{2-x}Fe_xP$ systems although those studies were performed on less refractory DBT.[139]

Scheme 5.3. Different HDS pathways for 4,6-DMDBT molecule (DDS vs HYD)

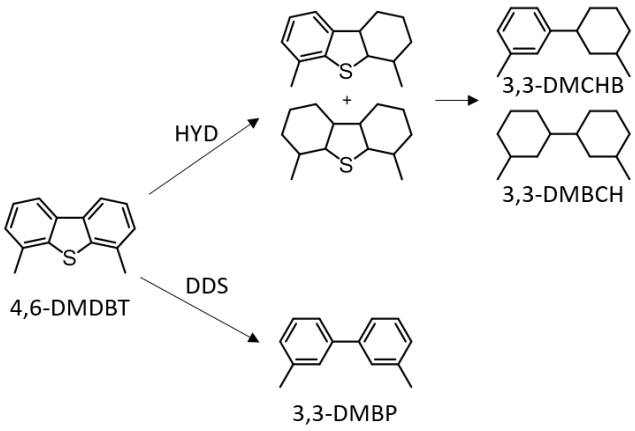

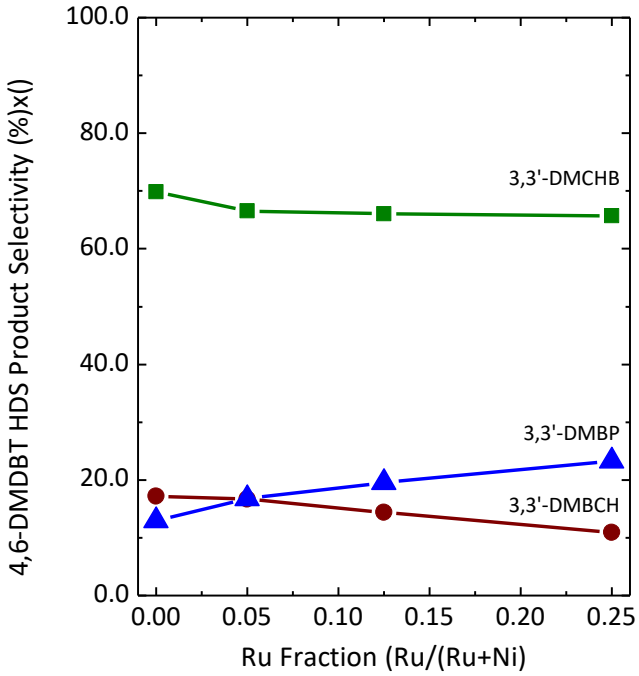

Figure 5.14. 4,6-DMDBT HDS product selectivities vs. Ru content

Figure 5.14 shows the product selectivity of 4,6-DMDBT for different $Ni_{2-x}Ru_xP$ compositions. The predominant product for all compositions is the partially hydrogenated product 3,3´-DMCHB which is produced via the HYD pathway (Scheme 5.1). As the Ru content increases the selectivity towards 3,3´-DMBP (DDS product) increases. As the activity decreases with increasing Ru, selectivity data might suggest that HDS via the HYD pathway is negatively affected by the addition of Ru.

5.4 Conclusions

Some selected compositions of $Ni_{2-x}Co_xP$ nanoparticles encapsulated in mesoporous silica were investigated as a model system for probing hydrodesulfurization (HDS) reaction over bimetallic phosphides. On a mass of catalyst basis, the highest DBT HDS activity was observed for a $Ni_{1.92}Co_{0.08}P@mSiO_2$ nanocatalyst, consistent with the results reported for TPR prepared silica-supported $Ni_{2-x}Co_xP$ catalysts. While the overall trend of HDS activity decreased with increasing Co content, the opposite trend was observed for TOFs, calculated based on CO

chemisorption capacity and activity. Higher TOFs could be attributed to the higher electron density present in Co-rich materials resulted by charge density transfer from Co to Ni. The DBT product selectivity of $Ni_{2-x}Co_xP@mSiO_2$ nanocatalysts changed only slightly due to Co incorporation, and the DDS is the preferable pathway for all compositions.

Some preliminary data were obtained for HDS of 4,6-DMDBT of $Ni_{2-x}Ru_xP@mSiO_2$ nanoparticles and surprisingly we observed the 4,6-DMDBT catalytic activity decreases with the introduction of noble metal Ru. While 3-3´-DMCHB produced via HYD pathway is the predominant product for all compositions, there is a clear dependency of DDS pathway on composition. Further studied are needed to probe the effect of composition on activity and selectivity for $Ni_{2-x}Ru_xP@mSiO_2$ catalysts. Overall, the nanoparticles encapsulated in mesoporous silica exhibited excellent phase stability and resistance to sintering and sulfur poisoning, indicating that these catalysts provide ideal robust model systems for probing the impact of particle size, shape and composition on hydrodesulfurization.

CHAPTER 6 CONCLUSIONS AND PROSPECTUS

6.1 Conclusions

The continued demand for low sulfur-containing diesel fuels combined with a switch to crude oil sources with higher impurity concentrations is driving the search for new approaches geared towards removing sulfur efficiently in the refining of fossil fuels. Hydrodesulfurization (HDS) is the standard industrial process for sulfur removal, and Ni (Co) promoted sulfided molybdenum is the state-of-the-art catalyst. However, the lamellar structure of sulfided molybdenum restricts the performance of these catalysts.[66] Additionally, as a solution to the anticipated energy crisis related to the depletion of fossil fuel sources and global warming associated with emission of green-house gases, production of renewable energy by water splitting has drawn much attention in recent times.[77] This electrocatalytic water splitting process requires an efficient catalyst to reduce the overpotential needed for the oxygen evolution reaction (OER) step. Metal phosphides have been studied as catalysts in both HDS and OER processes and recently attention has shifted to focus on ternary phases of metal phosphides to achieve synergy by the interaction of the two metals. An additional advantage of this approach is the ability to dilute highly active scarce metals with Earth-abundant, inexpensive metals while retaining (or even improving) activity. Synthetic methodologies are required to produce novel materials and simultaneously, in order to assess the impact of active site density on activity of these catalysts, preparation methods should produce discrete, phase-pure, and nearly monodisperse nanoparticles.

Solution-phase arrested precipitation reactions provide excellent control over size, shape and composition of nanoparticles. In this dissertation research, both ternary compositions $Ni_{2-x}Co_xP$ and $Ni_{2-x}Ru_xP$ could be prepared as nearly monodisperse samples ($Ni_{2-x}Co_xP$, $x \leq 1.7$, size 9-14 nm with S.D <20 % and $Ni_{2-x}Ru_xP$, $x \leq 1$, size 5-10 nm with S.D<15 %) with excellent composition control. It was also observed that different synthetic levers can be used to control the nature of

ternary phosphide nanoparticles. Specifically in the NiCoP system, with varying the metal:P ratio, temperature and heating rate, the morphology (dense vs hollow), size (7-25 nm) and composition of nanoparticles could be controlled. The ability to tune the size of nanoparticles opens the door to carry out size-dependent catalytic studies.

In the synthesis of ternary phosphide nanoparticles, it was evident that a single general approach could not be applied for the synthesis of any metal composition. For the Ni-Co-P system both metal precursors were added at the outset of the reaction in the presence of TOP. But in the Ni-Ru-P system first Ru particles have to be prepared and the Ni precursor and TOP subsequently added. The redox chemistry of the metal precursor is presumed to depend on the ligand environment. For example, both Ni and Co acac precursors were able to be reduced in the presence of TOP in the reaction medium. However, the $RuCl_3$ precursor is not susceptible to reduction in the presence of TOP and no nanoparticles could be isolated if TOP was used at the outset.

From catalytic studies, synergism was clearly observed. For the Ni-Co-P system the highest DBT HDS catalytic activity on a mass catalyst basis was observed for the $Ni_{1.92}Co_{0.08}P$ composition whereas for the Ni-Ru-P system the highest OER catalytic activity with respect to overpotential was observed for the $Ni_{1.25}Co_{0.75}P$ composition. The electronic interaction between the two metals in the ternary phosphide nanoparticles was clearly evidenced from catalytic data. The nature of this interaction depends on the properties of the metals and these interactions change the redox properties of the metals. From the IR spectroscopic studies of CO adsorbed on the catalyst surface, it was evident that Ni sites in Co-rich phases have higher electron density, which could be attributed to the electron density transfer from the Co metal. The higher density of electrons present on the Ni sites facilitates the HDS process, which involves H_2 and S adsorption steps. In the case of the Ni-Ru-P system, from the OER polarization curves we observed that

formation of an Ni oxidized species ($Ni^{II/III}$), purported to be the active species for OER, is facilitated with the introduction of Ru, resulting in higher OER catalytic activity. The change in redox characteristics of metals in ternary phosphides was further evidenced in the post reduction step of the encapsulated $Ni_{2-x}Ru_xP$ materials. In contrast to the Ni-Co-P system, in the Ni-Ru-P materials the final phase was sensitive to the amount of P source used. With the preliminary studies we have for HDS of Ni-Ru-P system, we can predict the lower activity for Ru incorporated materials might be related to the highly oxidizing nature of the Ni metal in Ni-Ru-P materials, which is responsible for the OER activity, in contrast to the highly reducing nature of Ni in Ni-Co-P materials. The presence of a sweet spot especially for the OER catalytic activity might suggest other than the electronic interaction of two metals, other factors such as site occupancy (tetrahedral vs square pyramidal) have an impact on the catalytic activity.

It is demonstrated that encapsulated materials are ideal model catalysts to study the impact of active site density on activity of these materials. The robust nature of these catalysts, which maintain good size and shape stability under harsh HDS conditions, suggests the ability of these systems for systematic catalytic studies (probing the role of particle size, shape and composition) for modeling of better hydrotreating catalysts.

6.2 Prospectus

6.2.1 Size dependent HDS catalytic studies of ternary phosphide nanoparticles

As we were able to tune the particle size and encapsulated systems are robust under HDS conditions, size dependent HDS catalytic studied have to be carried out to study the impact of active site density on catalytic performance. As it has been reported before in HDS studies, the site occupancy of metals (M(1) and M(2)) depends on the size of the particles,[70] thus it is worthy to study the impact of the different sizes of particles on both HDS activity and selectivity.

6.2.2 Determine the site occupancy of different metals in ternary phase using X-ray absorption studies

Hexagonal Ni_2P structure has two metal sites; M(1) tetrahedral and M(2) square pyramidal. There could be a composition dependent occupancy of metals on these sites as evidenced before by EXAFS and Mössbauer spectroscopy studies for TPR prepared materials.[69, 74] By studying the site occupancy of solution-phase prepared Ni-Co-P and Ni-Ru-P nanoparticles composition-dependent catalytic activity can be explained in detail with respect to the site occupancy.

6.2.3 XPS studies to probe the surface nature of encapsulated nanoparticles

As the surface characteristics are the most important characteristic for catalytic behavior the surface nature of the encapsulated materials should be probed with a surface sensitive technique such as XPS to probe the surface state and composition of each element encapsulated in mesoporous silica. These data can be compared with the XPS data for the as prepared particles to understand the surface modifications undergone during the encapsulation process.

6.2.4 Catalytic properties of ternary phosphide nanoparticles for other applications

Hydrodeoxygenation (HDO) is an important hydrotreating catalytic process in the production of bio fuel from the pyrolysis of biomass. This process can be used to remove oxygen from biofuel that results in low energy density, high viscosity, low volatility and thermal instability.[33] Transition metal phosphides have been used as catalysts in this process and in a study reported by the Bussell group Ru_2P has shown the best performance for furan HDO, while Ni_2P is showing a considerable activity (Ru_2P/SiO_2 activity 12390 mmol furan/g.s while Ni_2P/SiO_2 activity 1610 mmol furan/g.s) .[145] It will be interesting to study the HDO performance of a ternary phase comprising both Ru and Ni metals in the phosphide lattice.

Further as shown in Appendix A we can access the phase pure crystalline Ru_xP_y phases. These encapsulated materials could be tested for HDO activity and compare the performance with TPR prepared materials.

These ternary phosphides ($Ni_{2-x}CoxP$ and $Ni_{2-x}CoxP$) can be tested for photocatalytic water splitting specially for hydrogen evolution reaction (HER). As reported in previous studies, to increase the efficiency of energy conversion the phosphide nanoparticles could be mixed with a semiconducting material to build a hybrid composite and study photocatalytic HER.[146]

APPENDIX A PREPARATION OF ENCAPSUALTED CRYSTALLINE Ru_xP_y NANOPARTICLES

In previous work reported by the Brock group, it was revealed that crystalline, discrete Pd_5P_2 nanoparticles could be prepared by thermal treatment of amorphous Pd_xP_y particles encapsulated in mesoporous silica.[147] Hence, encapsulated materials were able to be directly used for hydro-treating catalytic studies. A similar approach was followed for the Ru-P phase materials reported here. First, the amorphous material with Ru:P~2 was encapsulated in mesoporous silica (Section 5.2.2) and directly reduced under Ar/H_2 at 450 °C as this temperature was sufficient to crystallize the as-prepared nanoparticles. As shown in Figure A1(a) the material heated for 1 h at 450 °C remains amorphous in contrast to what is observed for as-prepared materials (Figure 4.3(a)). Accordingly, a higher temperature was used. When another portion of the encapsulated material was heated at 500 °C with 1 g of PPh_3 and as shown in Figure A1(b) appearance of peaks corresponding to Ru_2P phase was observed. As this product was not phase pure Ru_2P, the same portion was further heated to 550 °C without a P source. In this case as shown in Figure A1(c) mostly crystalline products were obtained and in addition to Ru_2P phase impurity phases which could be indexed to Ru or RuP were observed. These results suggested that crystalline Ru-P phases could be achieved as encapsulated materials at high temperatures, but to obtain phase-pure Ru_2P, adjustments in the Ru:P ratio is required.

Thus, as the next step, as prepared Ru nanoparticles (with no P) were encapsulated in mesoporous silica and directly annealed at 550 °C in the presence of 1g of PPh_3. To evaluate the effect of calcination, another portion of the same encapsulated material was calcined in air at 425

°C for 2 h prior to the reduction step. As shown in figure A2(a) the directly reduced material with 1 g of PPh_3 shows the peaks corresponding to Ru_2P phase only, suggesting phase-pure Ru_2P phase can be obtained through this approach. The material calcined and reduced with 1 g of PPh_3 shows Ru metal as an impurity phase in the PXRD pattern in addition to the Ru_2P phase (Figure A2(b)).

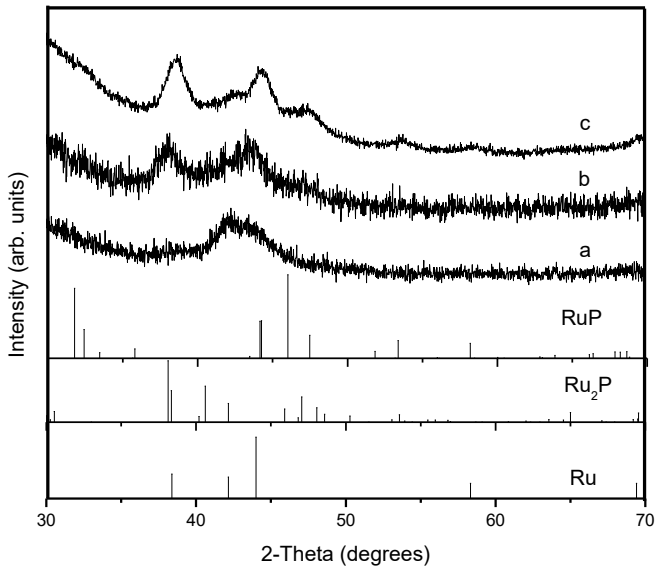

Figure A1. PXRD patterns of the encapsulated amorphous Ru:P~2 materials annealed in reducing environment under different conditions (a) annealed 450 °C for 1 h (b) annealed 500 °C for 2 h with 1 g of PPh_3 (c) product from (b) step further annealed 550 °C for 2 h with no P source

In order to prepare encapsulated crystalline RuP phase, amorphous phase materials with Ru:P~1 was encapsulated in silica and heat treated under reducing conditions. As shown in Figure A3(a) the material directly reduced with 1 g of PPh_3 shows broad peaks, which can be indexed to the RuP phase. In contrast the calcined material, subsequently reduced with 1 g of PPh_3 shows the crystalline peaks corresponding to the phase pure RuP (Figure A3(b)). These data clearly show phase pure Ru-P phases could be achieved as encapsulated materials and calcination step has a huge impact on the resultant phase.

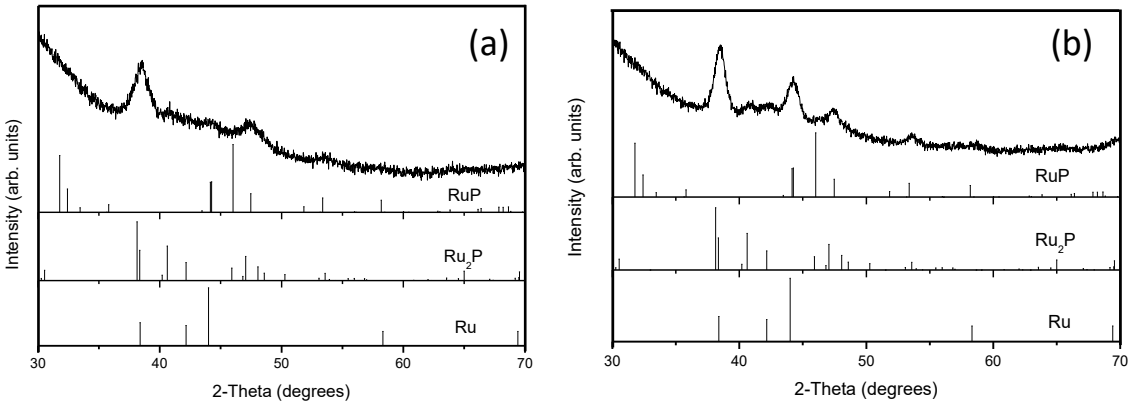

Figure A2. PXRD patterns of the encapsulated Ru nanoparticles annealed in reducing environment under different conditions (a) as encapsulated material directly reduced at 550 °C for 2 h with 1 g PPh_3 (b) encapsulated material first calcined at 425 °C for 2 h and then reduced at 550 °C for 2 h with 1 g PPh_3

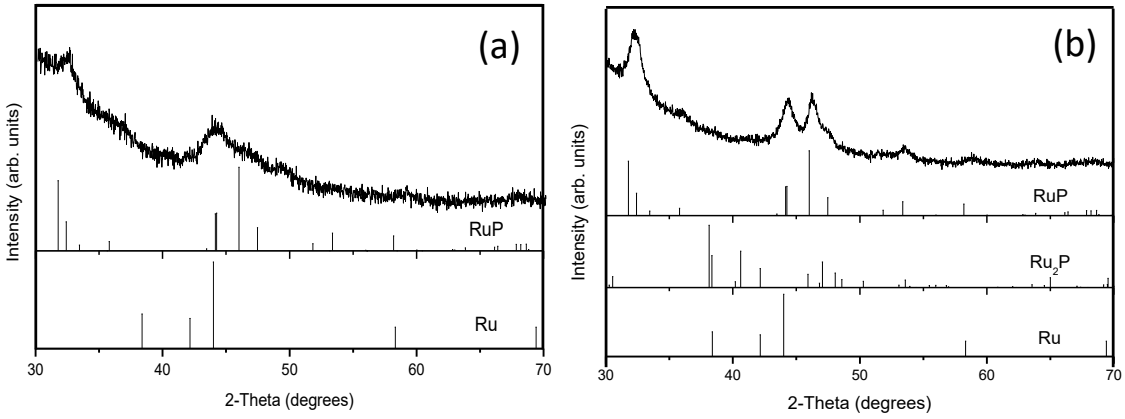

Figure A3. PXRD patterns of the encapsulated amorphous Ru:P~1 nanoparticles annealed in reducing environment under different conditions (a) as encapsulated material directly reduced at 550 °C for 2 h with 1 g PPh3 (b) encapsulated material first calcined at 425 °C for 2 h and then reduced at 550 °C for 2 h with 1 g PPh_3

APPENDIX B PERMISSION/LICENCE AGREEMENT FOR COPYRIGHT MATERIALS

ELSEVIER LICENSE
TERMS AND CONDITIONS

Sep 06, 2016

This Agreement between Don Ruchira Liyanage ("You") and Elsevier ("Elsevier") consists of your license details and the terms and conditions provided by Elsevier and Copyright Clearance Center.

License Number	3942861176992
License date	Sep 06, 2016
Licensed Content Publisher	Elsevier
Licensed Content Publication	Surface Science
Licensed Content Title	Probing hydrodesulfurization over bimetallic phosphides using monodisperse $Ni_{2-x}M_xP$ nanoparticles encapsulated in mesoporous silica
Licensed Content Author	Samuel J. Danforth,D. Ruchira Liyanage,Asha Hitihami-Mudiyanselage,Boris Ilic,Stephanie L. Brock,Mark E. Bussell
Licensed Content Date	June 2016
Licensed Content Volume Number	648
Licensed Content Issue Number	n/a
Licensed Content Pages	10
Start Page	126
End Page	135
Type of Use	reuse in a thesis/dissertation
Portion	full article
Format	electronic
Are you the author of this Elsevier article?	Yes
Will you be translating?	No
Order reference number	
Title of your thesis/dissertation	Synthesis and Characterization of Transition Metal Phosphide Nanoparticles for Catalytic Applications: Model Catalysts for Hydrodesulfurization and Electrocatalysts for the Oxygen Evolution Reaction
Expected completion date	Oct 2016

Estimated size (number of pages)	140
Elsevier VAT number	GB 494 6272 12
Requestor Location	Don Ruchira Liyanage 4747 Anthony Wayne Dr DETROIT, MI 48201 United States Attn: Don Ruchira Liyanage
Total	0.00 USD

Title: Mössbauer spectroscopy investigation and hydrodesulfurization properties of iron–nickel phosphide catalysts
Author: Amy F. Gaudette,Autumn W. Burns,John R. Hayes,Mica C. Smith,Richard H. Bowker,Takele Seda,Mark E. Bussell
Publication: Journal of Catalysis
Publisher: Elsevier
Date: 25 May 2010

Logged in as:
Don Ruchira Liyanage
Account #: 3001060518
LOGOUT

Order Completed
Thank you for your order.

This Agreement between Don Ruchira Liyanage ("You") and Elsevier ("Elsevier") consists of your license details and the terms and conditions provided by Elsevier and Copyright Clearance Center.

Your confirmation email will contain your order number for future reference.

Get the printable license.

License Number	3945440973550
License date	Sep 10, 2016
Licensed Content Publisher	Elsevier
Licensed Content Publication	Journal of Catalysis
Licensed Content Title	Mössbauer spectroscopy investigation and hydrodesulfurization properties of iron–nickel phosphide catalysts
Licensed Content Author	Amy F. Gaudette,Autumn W. Burns,John R. Hayes,Mica C. Smith,Richard H. Bowker,Takele Seda,Mark E. Bussell
Licensed Content Date	25 May 2010
Licensed Content Volume	272
Licensed Content Issue	1
Licensed Content Pages	10
Type of Use	reuse in a thesis/dissertation
Portion	figures/tables/illustrations
Number of figures/tables/illustrations	1
Format	electronic
Are you the author of this Elsevier article?	No

Will you be translating?	No
Order reference number	
Original figure numbers	Fig. 2.
Title of your thesis/ dissertation	Synthesis and Characterization of Transition Metal Phosphide Nanoparticles for Catalytic Applications: Model Catalysts for Hydrodesulfurization and Electrocatalysts for the Oxygen Evolution Reaction
Expected completion date	Oct 2016
Estimated size (number of pages)	140
Elsevier VAT number	GB 494 6272 12
Requestor Location	Don Ruchira Liyanage 4747 Anthony Wayne Dr 4747 Anthony Wayne Dr DETROIT, MI 48201 United States
Total	Attn: Don Ruchira Liyanage 0.0 USD

ORDER MORE CLOSE WINDOW

REFERENCES

1. Alivisatos, A. P. Perspectives on the Physical Chemistry of Semiconductor Nanocrystals. *J. Phys. Chem.* **1996,** 100, 13226-13239.

2. Alivisatos, A. P. Semiconductor Clusters, Nanocrystals, and Quantum Dots. *Science* **1996,** 271, 933.

3. Leslie-Pelecky, D. L.; Rieke, R. D. Magnetic Properties of Nanostructured Materials. *Chem. Mater*. **1996,** 8, 1770-1783.

4. Eustis, S.; El-Sayed, M. A. Why Gold Nanoparticles Are More Precious Than Pretty Gold: Noble Metal Surface Plasmon Resonance and Its Enhancement of the Radiative and Nonradiative Properties of Nanocrystals of Different Shapes. *Chem. Soc. Rev.* **2006,** 35, 209-217.

5. Sun, Y.; Xia, Y. Gold and Silver Nanoparticles: A Class of Chromophores with Colors Tunable in the Range from 400 to 750 nm. *Analyst* **2003,** 128, 686-691.

6. Valden, M.; Lai, X.; Goodman, D. W. Onset of Catalytic Activity of Gold Clusters on Titania with the Appearance of Nonmetallic Properties. *Science* **1998,** 281, 1647-1650.

7. Rao, C.; Kulkarni, G.; Thomas, P. J.; Edwards, P. P. Size-Dependent Chemistry: Properties of Nanocrystals. *Chem.-Eur. J.* **2002,** 8, 28-35.

8. El-Sayed, M. A. Small Is Different: Shape-, Size-, and Composition-Dependent Properties of Some Colloidal Semiconductor Nanocrystals. *Acc. Chem. Res.* **2004,** 37, 326-333.

9. Burda, C.; Chen, X.; Narayanan, R.; El-Sayed, M. A. Chemistry and Properties of Nanocrystals of Different Shapes. *Chem. Rev.* **2005,** 105, 1025-1102.

10. Huynh, W. U.; Dittmer, J. J.; Alivisatos, A. P. Hybrid Nanorod-Polymer Solar Cells. *Science* **2002,** 295, 2425-2427.

11. Michalet, X.; Pinaud, F. F.; Bentolila, L. A.; Tsay, J. M.; Doose, S.; Li, J. J.; Sundaresan, G.; Wu, A. M.; Gambhir, S. S.; Weiss, S. Quantum Dots for Live Cells, in Vivo Imaging, and Diagnostics. *Science* **2005,** 307, 538-544.

12. Talapin, D. V.; Lee, J.-S.; Kovalenko, M. V.; Shevchenko, E. V. Prospects of Colloidal Nanocrystals for Electronic and Optoelectronic Applications. *Chem. Rev.* **2010,** 110, 389-458.

13. Brock, S. L.; Perera, S. C.; Stamm, K. L. Chemical Routes for Production of Transition-Metal Phosphides on the Nanoscale: Implications for Advanced Magnetic and Catalytic Materials. *Chem.–Eur. J.* **2004,** 10, 3364-3371.

14. Brock, S. L.; Senevirathne, K. Recent Developments in Synthetic Approaches to Transition Metal Phosphide Nanoparticles for Magnetic and Catalytic Applications. *J.Solid State Chem.* **2008,** 181, 1552-1559.

15. Muthuswamy, E.; Kharel, P. R.; Lawes, G.; Brock, S. L. Control of Phase in Phosphide Nanoparticles Produced by Metal Nanoparticle Transformation: Fe_2P and FeP. *ACS Nano* **2009,** 3, 2383-2393.

16. Muthuswamy, E.; Savithra, G. H. L.; Brock, S. L. Synthetic Levers Enabling Independent Control of Phase, Size, and Morphology in Nickel Phosphide Nanoparticles. *ACS Nano* **2011,** 5, 2402-2411.

17. Senevirathne, K.; Tackett, R.; Kharel, P. R.; Lawes, G.; Somaskandan, K.; Brock, S. L. Discrete, Dispersible Mnas Nanocrystals from Solution Methods: Phase Control on the Nanoscale and Magnetic Consequences. *ACS Nano* **2009,** 3, 1129-1138.

18. Zhang, Y.; Regmi, R.; Liu, Y.; Lawes, G.; Brock, S. L. Phase-Coexistence and Thermal Hysteresis in Samples Comprising Adventitiously Doped MnAs Nanocrystals: Programming of Aggregate Properties in Magnetostructural Nanomaterials. *ACS Nano* **2014,** 8, 6814-6821.

19. Hettiarachchi, M. A.; Abdelhamid, E.; Nadgorny, B.; Brock, S. L. Synthesis of Colloidal MnSb Nanoparticles: Consequences of Size and Surface Characteristics on Magnetic Properties. *J, Mater. Chem., C* **2016,** 4, 6790-6797.

20. Hitihami-Mudiyanselage, A.; Arachchige, M. P.; Seda, T.; Lawes, G.; Brock, S. L. Synthesis and Characterization of Discrete $Fe_xNi_{2-X}P$ Nanocrystals ($0 < X < 2$): Compositional Effects on Magnetic Properties. *Chem. Mater.* **2015,** 27, 6592-6600.

21. Liyanage, D. R.; Danforth, S. J.; Liu, Y.; Bussell, M. E.; Brock, S. L. Simultaneous Control of Composition, Size, and Morphology in Discrete $Ni_{2-X}Co_xP$ Nanoparticles. *Chem. Mater.* **2015,** 27, 4349-4357.

22. Li, D.; Arachchige, M. P.; Kulikowski, B.; Lawes, G.; Seda, T.; Brock, S. L. Control of Composition and Size in Discrete $Co_xFe_{2-X}P$ Nanoparticles: Consequences for Magnetic Properties. *Chem. Mater.* **2016,** 28, 3920-3927.

23. Murray, C. B.; Norris, D. J.; Bawendi, M. G. Synthesis and Characterization of Nearly Monodisperse CdE (E = Sulfur, Selenium, Tellurium) Semiconductor Nanocrystallites. *J. Am. Chem. Soc.* **1993,** 115, 8706-8715.

24. Guzelian, A. A.; Katari, J. E. B.; Kadavanich, A. V.; Banin, U.; Hamad, K.; Juban, E.; Alivisatos, A. P.; Wolters, R. H.; Arnold, C. C.; Heath, J. R. Synthesis of Size-Selected, Surface-Passivated InP Nanocrystals. *J. Phys. Chem.* **1996,** 100, 7212-7219.

25. Yu, W. W.; Wang, Y. A.; Peng, X. Formation and Stability of Size-, Shape-, and Structure-Controlled CdTe Nanocrystals: Ligand Effects on Monomers and Nanocrystals. *Chem. Mater.* **2003,** 15, 4300-4308.

26. Klimov, V. I., *Nanocrystal Quantum Dots*. CRC Press: 2010.

27. Souza, D.; Pralong, V.; Jacobson, A.; Nazar, L. A Reversible Solid-State Crystalline Transformation in a Metal Phosphide Induced by Redox Chemistry. *Science* **2002,** 296, 2012-2015.

28. Sun, M.; Liu, H.; Qu, J.; Li, J. Earth-Rich Transition Metal Phosphide for Energy Conversion and Storage. *Adv. Energy. Mater.* **2016,** 6, 1600087.

29. Carenco, S.; Portehault, D.; Boissière, C.; Mézailles, N.; Sanchez, C. Nanoscaled Metal Borides and Phosphides: Recent Developments and Perspectives. *Chem. Rev.* **2013,** 113, 7981-8065.

30. Xie, R.; Battaglia, D.; Peng, X. Colloidal InP Nanocrystals as Efficient Emitters Covering Blue to near-Infrared. *J. Am. Chem. Soc.* **2007,** 129, 15432-15433.

31. Xiao, P.; Chen, W.; Wang, X. A Review of Phosphide-Based Materials for Electrocatalytic Hydrogen Evolution. *Adv. Energy Mater.* **2015,** 5, 1500985.

32. Suzuki, N.; Horie, T.; Kitahara, G.; Murase, M.; Shinozaki, K.; Morimoto, Y. Novel Noble-Metal-Free Electrocatalyst for Oxygen Evolution Reaction in Acidic and Alkaline Media. *Electrocatal.* **2016,** 7, 115-120.

33. Zhao, H. Y.; Li, D.; Bui, P.; Oyama, S. T. Hydrodeoxygenation of Guaiacol as Model Compound for Pyrolysis Oil on Transition Metal Phosphide Hydroprocessing Catalysts. *Appl. Catal., A* **2011,** 391, 305-310.

34. Prins, R.; Bussell, M. E. Metal Phosphides: Preparation, Characterization and Catalytic Reactivity. *Catal. Lett.* **2012,** 142, 1413-1436.

35. Blanchard, P. E. R.; Grosvenor, A. P.; Cavell, R. G.; Mar, A. X-Ray Photoelectron and Absorption Spectroscopy of Metal-Rich Phosphides M_2P and M_3P (M = Cr−Ni). *Chem. Mater.* **2008,** 20, 7081-7088.

36. Oyama, S. T. Novel Catalysts for Advanced Hydroprocessing: Transition Metal Phosphides. *J. Catal.* **2003,** 216, 343-352.

37. Lu, Y.; Tu, J.-P.; Xiong, Q.-Q.; Xiang, J.-Y.; Mai, Y.-J.; Zhang, J.; Qiao, Y.-Q.; Wang, X.-L.; Gu, C.-D.; Mao, S. X. Controllable Synthesis of a Monophase Nickel Phosphide/Carbon (Ni_5P_4/C) Composite Electrode via Wet-Chemistry and a Solid-State Reaction for the Anode in Lithium Secondary Batteries. *Adv. Funct. Mater.* **2012,** 22, 3927-3935.

38. Su, H. L.; Xie, Y.; Li, B.; Liu, X. M.; Qian, Y. T. A Simple, Convenient, Mild Solvothermal Route to Nanocrystalline Cu_3P and Ni_2P. *Solid State Ionics* **1999,** 122, 157-160.

39. Xie, Y.; Su, H. L.; Qian, X. F.; Liu, X. M.; Qian, Y. T. A Mild One-Step Solvothermal Route to Metal Phosphides (Metal=Co, Ni, Cu). *J.Solid State Chem.* **2000,** 149, 88-91.

40. Barry, B. M.; Gillan, E. G. Low-Temperature Solvothermal Synthesis of Phosphorus-Rich Transition-Metal Phosphides. *Chem. Mater.* **2008,** 20, 2618-2620.

41. Sawhill, S. J.; Phillips, D. C.; Bussell, M. E. Thiophene Hydrodesulfurization over Supported Nickel Phosphide Catalysts. *J. Catal.* **2003,** 215, 208-219.

42. Molina, R.; Poncelet, G. A-Alumina-Supported Nickel Catalysts Prepared from Nickel Acetylacetonate: A TPR Study. *J. Catal.* **1998,** 173, 257-267.

43. Reiche, M. A.; Maciejewski, M.; Baiker, A. Characterization by Temperature Programmed Reduction. *Catal. Today* **2000,** 56, 347-355.

44. Perera, S. C.; Tsoi, G.; Wenger, L. E.; Brock, S. L. Synthesis of MnP Nanocrystals by Treatment of Metal Carbonyl Complexes with Phosphines: A New, Versatile Route to Nanoscale Transition Metal Phosphides. *J.Am. Chem. Soc.* **2003,** 125, 13960-13961.

45. Park, J.; Koo, B.; Yoon, K. Y.; Hwang, Y.; Kang, M.; Park, J.-G.; Hyeon, T. Generalized Synthesis of Metal Phosphide Nanorods via Thermal Decomposition of Continuously Delivered Metal−Phosphine Complexes Using a Syringe Pump. *J.Am. Chem. Soc.* **2005,** 127, 8433-8440.

46. Perera, S. C.; Fodor, P. S.; Tsoi, G. M.; Wenger, L. E.; Brock, S. L. Application of De-Silylation Strategies to the Preparation of Transition Metal Pnictide Nanocrystals: The Case of FeP. *Chem. Mater.* **2003,** 15, 4034-4038.

47. Park, J.; Koo, B.; Hwang, Y.; Bae, C.; An, K.; Park, J.-G.; Park, H. M.; Hyeon, T. Novel Synthesis of Magnetic Fe_2P Nanorods from Thermal Decomposition of Continuously Delivered Precursors Using a Syringe Pump. *Angew. Chem. Int. Ed.* **2004,** 43, 2282-2285.

48. Zhang, H.; Ha, D.-H.; Hovden, R.; Kourkoutis, L. F.; Robinson, R. D. Controlled Synthesis of Uniform Cobalt Phosphide Hyperbranched Nanocrystals Using Tri-n-Octylphosphine Oxide as a Phosphorus Source. *Nano. Lett.* **2011,** 11, 188-197.

49. Ha, D.-H.; Moreau, L. M.; Bealing, C. R.; Zhang, H.; Hennig, R. G.; Robinson, R. D. The Structural Evolution and Diffusion During the Chemical Transformation from Cobalt to Cobalt Phosphide Nanoparticles. *J. Mater. Chem.* **2011,** 21, 11498-11510.

50. Henkes, A. E.; Vasquez, Y.; Schaak, R. E. Converting Metals into Phosphides: A General Strategy for the Synthesis of Metal Phosphide Nanocrystals. *J.Am. Chem. Soc.* **2007,** 129, 1896-1897.

51. Yin, Y.; Rioux, R. M.; Erdonmez, C. K.; Hughes, S.; Somorjai, G. A.; Alivisatos, A. P. Formation of Hollow Nanocrystals through the Nanoscale Kirkendall Effect. *Science* **2004,** 304, 711-714.

52. Chiang, R.-K.; Chiang, R.-T. Formation of Hollow Ni_2P Nanoparticles Based on the Nanoscale Kirkendall Effect. *Inorg. Chem.* **2006,** 46, 369-371.

53. Carenco, S.; Portehault, D.; Boissière, C.; Mézailles, N.; Sanchez, C. 25th Anniversary Article: Exploring Nanoscaled Matter from Speciation to Phase Diagrams: Metal Phosphide Nanoparticles as a Case of Study. *Adv, Mater.* **2014,** 26, 371-390.

54. Layan Savithra, G. H.; Muthuswamy, E.; Bowker, R. H.; Carrillo, B. A.; Bussell, M. E.; Brock, S. L. Rational Design of Nickel Phosphide Hydrodesulfurization Catalysts: Controlling Particle Size and Preventing Sintering. *Chem. Mater.* **2013,** 25, 825-833.

55. Carenco, S.; Boissière, C.; Nicole, L.; Sanchez, C.; Le Floch, P.; Mézailles, N. Controlled Design of Size-Tunable Monodisperse Nickel Nanoparticles. *Chem. Mater.* **2010,** 22, 1340-1349.

56. Li, D.; Senevirathne, K.; Aquilina, L.; Brock, S. L. Effect of Synthetic Levers on Nickel Phosphide Nanoparticle Formation: Ni_5P_4 and NiP_2. *Inorg. Chem.* **2015,** 54, 7968-7975.

57. Callejas, J. F.; Read, C. G.; Roske, C. W.; Lewis, N. S.; Schaak, R. E. Synthesis, Characterization, and Properties of Metal Phosphide Catalysts for the Hydrogen-Evolution Reaction. *Chem. Mater.* **2016,** 28, 6017-6044.

58. Fruchart, R.; Roger, A.; Senateur, J. P. Crystallographic and Magnetic Properties of Solid Solutions of the Phosphides M_2P, M = Cr, Mn, Fe, Co, and Ni. *J. Appl. Phys.* **1969,** 40, 1250-1257.

59. Yoon, K. Y.; Jang, Y.; Park, J.; Hwang, Y.; Koo, B.; Park, J.-G.; Hyeon, T. Synthesis of Uniform-Sized Bimetallic Iron–Nickel Phosphide Nanorods. *J.Solid State Chem.* **2008,** 181, 1609-1613.

60. Ye, E.; Zhang, S.-Y.; Lim, S. H.; Bosman, M.; Zhang, Z.; Win, K. Y.; Han, M.-Y. Ternary Cobalt–Iron Phosphide Nanocrystals with Controlled Compositions, Properties, and Morphologies from Nanorods and Nanorice to Split Nanostructures. *Chem.-Eur. J.* **2011,** 17, 5982-5988.

61. Colson, A. C.; Whitmire, K. H. Synthesis of $Fe_{2-X}Mn_xp$ Nanoparticles from Single-Source Molecular Precursors. *Chem. Mater.* **2011,** 23, 3731-3739.

62. Mendoza-Garcia, A.; Zhu, H.; Yu, Y.; Li, Q.; Zhou, L.; Su, D.; Kramer, M. J.; Sun, S. Controlled Anisotropic Growth of Co-Fe-P from Co-Fe-O Nanoparticles. *Angew. Chem.* **2015,** 127, 9778-9781.

63. Li, D.; Baydoun, H.; Verani, C. N.; Brock, S. L. Efficient Water Oxidation Using CoMnP Nanoparticles. *J. Am. Chem. Soc.* **2016,** 138, 4006-4009.

64. Knudsen, K. G.; Cooper, B. H.; Topsøe, H. Catalyst and Process Technologies for Ultra Low Sulfur Diesel. *Appl. Catal., A* **1999,** 189, 205-215.

65. Pawelec, B.; Navarro, R. M.; Campos-Martin, J. M.; Fierro, J. L. Towards near Zero-Sulfur Liquid Fuels: A Perspective Review. *Catal. Sci. Tech.* **2011,** 1, 23-42.

66. Topsøe, H.; Clausen, B. S.; Massoth, F. E., *Hydrotreating Catalysis*. Springer: 1996.

67. Gates, B. C.; Topsøe, H. Reactivities in Deep Catalytic Hydrodesulfurization: Challenges, Opportunities, and the Importance of 4-Methyldibenzothiophene and 4,6-Dimethyldibenzothiophene. *Polyhedron* **1997,** 16, 3213-3217.

68. Shafi, R.; Hutchings, G. J. Hydrodesulfurization of Hindered Dibenzothiophenes: An Overview. *Catal. Today* **2000,** 59, 423-442.

69. Gaudette, A. F.; Burns, A. W.; Hayes, J. R.; Smith, M. C.; Bowker, R. H.; Seda, T.; Bussell, M. E. Mössbauer Spectroscopy Investigation and Hydrodesulfurization Properties of Iron–Nickel Phosphide Catalysts. *J. Catal.* **2010,** 272, 18-27.

70. Oyama, S. T.; Lee, Y.-K. The Active Site of Nickel Phosphide Catalysts for the Hydrodesulfurization of 4,6-DMDBT. *J. Catal.* **2008,** 258, 393-400.

71. Burns, A. W.; Gaudette, A. F.; Bussell, M. E. Hydrodesulfurization Properties of Cobalt–Nickel Phosphide Catalysts: Ni-Rich Materials Are Highly Active. *J. Catal.* **2008,** 260, 262-269.

72. Abu, I. I.; Smith, K. J. The Effect of Cobalt Addition to Bulk MoP and Ni_2P Catalysts for the Hydrodesulfurization of 4, 6-Dimethyldibenzothiophene. *J. Catal.* **2006,** 241, 356-366.

73. Ted Oyama, S.; Zhao, H.; Freund, H.-J.; Asakura, K.; Włodarczyk, R.; Sierka, M. Unprecedented Selectivity to the Direct Desulfurization (DDS) Pathway in a Highly Active FeNi Bimetallic Phosphide Catalyst. *J. Catal.* **2012,** 285, 1-5.

74. Zhao, H.; Oyama, S. T.; Freund, H.-J.; Włodarczyk, R.; Sierka, M. Nature of Active Sites in Ni_2P Hydrotreating Catalysts as Probed by Iron Substitution. *Appl. Catal., B* **2015,** 164, 204-216.

75. Senevirathne, K.; Burns, A. W.; Bussell, M. E.; Brock, S. L. Synthesis and Characterization of Discrete Nickel Phosphide Nanoparticles: Effect of Surface Ligation Chemistry on Catalytic Hydrodesulfurization of Thiophene. *Adv. Funct. Mater.* **2007,** 17, 3933-3939.

76. Song, H.; Dai, M.; Song, H.-L.; Wan, X.; Xu, X.-W.; Jin, Z.-S. A Solution-Phase Synthesis of Supported Ni_2P Catalysts with High Activity for Hydrodesulfurization of Dibenzothiophene. *J. Mol. Catal. A: Chem.* **2014,** 385, 149-159.

77. Kudo, A.; Miseki, Y. Heterogeneous Photocatalyst Materials for Water Splitting. *Chem. Soc. Rev.* **2009,** 38, 253-278.

78. Lewis, N. S.; Nocera, D. G. Powering the Planet: Chemical Challenges in Solar Energy Utilization. *Proc. Natl. Acad. Sci. USA* **2006,** 103, 15729-15735.

79. Fabbri, E.; Habereder, A.; Waltar, K.; Kotz, R.; Schmidt, T. J. Developments and Perspectives of Oxide-Based Catalysts for the Oxygen Evolution Reaction. *Catal. Sci. Tech.* **2014,** 4, 3800-3821.

80. Man, I. C.; Su, H.-Y.; Calle-Vallejo, F.; Hansen, H. A.; Martínez, J. I.; Inoglu, N. G.; Kitchin, J.; Jaramillo, T. F.; Nørskov, J. K.; Rossmeisl, J. Universality in Oxygen Evolution Electrocatalysis on Oxide Surfaces. *ChemCatChem* **2011,** 3, 1159-1165.

81. Rossmeisl, J.; Qu, Z. W.; Zhu, H.; Kroes, G. J.; Nørskov, J. K. Electrolysis of Water on Oxide Surfaces. *J. Electroanal. Chem.* **2007,** 607, 83-89.

82. Lee, Y.; Suntivich, J.; May, K. J.; Perry, E. E.; Shao-Horn, Y. Synthesis and Activities of Rutile IrO_2 and RuO_2 Nanoparticles for Oxygen Evolution in Acid and Alkaline Solutions. *J. Phys. Chem. Lett.* **2012,** 3, 399-404.

83. Mamaca, N.; Mayousse, E.; Arrii-Clacens, S.; Napporn, T. W.; Servat, K.; Guillet, N.; Kokoh, K. B. Electrochemical Activity of Ruthenium and Iridium Based Catalysts for Oxygen Evolution Reaction. *Appl. Catal., B* **2012,** 111–112, 376-380.

84. Reier, T.; Oezaslan, M.; Strasser, P. Electrocatalytic Oxygen Evolution Reaction (OER) on Ru, Ir, and Pt Catalysts: A Comparative Study of Nanoparticles and Bulk Materials. *ACS Catal.* **2012,** 2, 1765-1772.

85. Paoli, E. A.; Masini, F.; Frydendal, R.; Deiana, D.; Schlaup, C.; Malizia, M.; Hansen, T. W.; Horch, S.; Stephens, I. E. L.; Chorkendorff, I. Oxygen Evolution on Well-Characterized Mass-Selected Ru and RuO_2 Nanoparticles. *Chem. Sci.* **2015,** 6, 190-196.

86. Cherevko, S.; Geiger, S.; Kasian, O.; Kulyk, N.; Grote, J.-P.; Savan, A.; Shrestha, B. R.; Merzlikin, S.; Breitbach, B.; Ludwig, A.; Mayrhofer, K. J. J. Oxygen and Hydrogen Evolution Reactions on Ru, RuO_2, Ir, and IrO_2 Thin Film Electrodes in Acidic and Alkaline Electrolytes: A Comparative Study on Activity and Stability. *Catal. Today* **2016,** 262, 170-180.

87. Zong, R.; Thummel, R. P. A New Family of Ru Complexes for Water Oxidation. *J. Am. Chem. Soc.* **2005,** 127, 12802-12803.

88. Duan, L.; Bozoglian, F.; Mandal, S.; Stewart, B.; Privalov, T.; Llobet, A.; Sun, L. A Molecular Ruthenium Catalyst with Water-Oxidation Activity Comparable to That of Photosystem II. *Nat. Chem.* **2012,** 4, 418-423.

89. Shi, Y.; Zhang, B. Recent Advances in Transition Metal Phosphide Nanomaterials: Synthesis and Applications in Hydrogen Evolution Reaction. *Chem. Soc. Rev.* **2016,** 45, 1529-1541.

90. Popczun, E. J.; McKone, J. R.; Read, C. G.; Biacchi, A. J.; Wiltrout, A. M.; Lewis, N. S.; Schaak, R. E. Nanostructured Nickel Phosphide as an Electrocatalyst for the Hydrogen Evolution Reaction. *J. Am. Chem. Soc.* **2013,** 135, 9267-9270.

91. Chang, J.; Xiao, Y.; Xiao, M.; Ge, J.; Liu, C.; Xing, W. Surface Oxidized Cobalt-Phosphide Nanorods as an Advanced Oxygen Evolution Catalyst in Alkaline Solution. *ACS Catal.* **2015,** 5, 6874-6878.

92. Han, A.; Chen, H.; Sun, Z.; Xu, J.; Du, P. High Catalytic Activity for Water Oxidation Based on Nanostructured Nickel Phosphide Precursors. *Chem. Commun.* **2015,** 51, 11626-11629.

93. Stern, L.-A.; Feng, L.; Song, F.; Hu, X. Ni_2P as a Janus Catalyst for Water Splitting: The Oxygen Evolution Activity of Ni_2P Nanoparticles. *Energy Environ. Sci.* **2015,** 8, 2347-2351.

94. Li, J.; Li, J.; Zhou, X.; Xia, Z.; Gao, W.; Ma, Y.; Qu, Y. Highly Efficient and Robust Nickel Phosphides as Bifunctional Electrocatalysts for Overall Water-Splitting. *ACS Appl. Mater. Interfaces* **2016,** 8, 10826-10834.

95. Liu, M.; Li, J. Cobalt Phosphide Hollow Polyhedron as Efficient Bifunctional Electrocatalysts for the Evolution Reaction of Hydrogen and Oxygen. *ACS Appl. Mater. Interfaces* **2016,** 8, 2158-2165.

96. Read, C. G.; Callejas, J. F.; Holder, C. F.; Schaak, R. E. General Strategy for the Synthesis of Transition Metal Phosphide Films for Electrocatalytic Hydrogen and Oxygen Evolution. *ACS Appl.Mater. Interfaces* **2016,** 8, 12798-12803.

97. Mobarok, M. H.; Luber, E. J.; Bernard, G. M.; Peng, L.; Wasylishen, R. E.; Buriak, J. M. Phase-Pure Crystalline Zinc Phosphide Nanoparticles: Synthetic Approaches and Characterization. *Chem. Mater.* **2014,** 26, 1925-1935.

98. Libin, Y.; Honglan, Q.; Chengxiao, Z.; Xuping, S. An Efficient Bifunctional Electrocatalyst for Water Splitting Based on Cobalt Phosphide. *Nanotechnology* **2016,** 27, 23LT01.

99. Mendoza-Garcia, A.; Su, D.; Sun, S. Sea Urchin-Like Cobalt-Iron Phosphide as an Active Catalyst for Oxygen Evolution Reaction. *Nanoscale* **2016,** 8, 3244-3247.

100. West, A. R.; West, C., *Basic Solid State Chemistry*. John Wiley & Sons New York: **1999**.

101. West, A. R., *Solid State Chemistry and Its Applications*. John Wiley & Sons: **2007**.

102. Pecharsky, V. K.; Zavalij, P. Y., *Fundamentals of Powder Diffraction and Structural Characterization of Materials*. Springer: **2009.**

103. Cullity, B. D. Elements of X-Ray Diffraction. **2001**.

104. Williams, D. B.; Carter, C. B., The Transmission Electron Microscope. In *Transmission Electron Microscopy*, Springer: **1996.**

105. Howe, J.; Fultz, B., Transmission Electron Microscopy and Diffractometry of Materials. In Springer, Berlin: **2001.**

106. Goodhew, P. J.; Humphreys, J.; Beanland, R., *Electron Microscopy and Analysis*. CRC Press: **2000.**

107. Webb, P. A.; Orr, C., *Analytical Methods in Fine Particle Technology*. Micromeritics Instrument Corp: **1997.**

108. Wagner, J. M., *X-Ray Photoelectron Spectroscopy*. Nova Science Publishers: **2010.**

109. Ding, L.; Shu, Y.; Wang, A.; Zheng, M.; Li, L.; Wang, X.; Zhang, T. Preparation and Catalytic Performances of Ternary Phosphides NiCoP for Hydrazine Decomposition. *Appl. Catal., A* **2010,** 385, 232-237.

110. Lu, A.; Chen, Y.; Li, H.; Dowd, A.; Cortie, M. B.; Xie, Q.; Guo, H.; Qi, Q.; Peng, D.-L. Magnetic Metal Phosphide Nanorods as Effective Hydrogen-Evolution Electrocatalysts. *Int. J. Hydrogen. Energy* **2014,** 39, 18919-18928.

111. Aiken Iii, J. D.; Lin, Y.; Finke, R. G. A Perspective on Nanocluster Catalysis: Polyoxoanion and $(n\text{-}C_4H_9)^{4n+}$ Stabilized Ir(0)∼300 Nanocluster 'Soluble Heterogeneous Catalysts'. *J. Mol. Catal. A: Chem.* **1996,** 114, 29-51.

112. Sénateur, J. P.; Rouault, A.; L'Héritier, P.; Krumbügel-Nylund, M. A.; Fruchart, R.; Fruchart, D.; Convert, P.; Roudaut, E. La Selectivite Des Substitutions Dans Les Phases Mm'p Etude De L'ordre Par Diffraction Neutronique Dans Nicop. *Mater. Res. Bull.* **1973,** 8, 229-238.

113. Huheey, J. E.; Keiter, E. A.; Keiter, R. L.; Medhi, O. K., *Inorganic Chemistry: Principles of Structure and Reactivity*. Pearson Education India: **2006.**

114. Maeda, Y.; Takashima, Y. Mössbauer Studies of FeNiP and Related Compounds. *J. Inorg. Nucl. Chem* **1973,** 35, 1963-1969.

115. Korányi, T. I. Phosphorus Promotion of Ni (Co)-Containing Mo-Free Catalysts in Thiophene Hydrodesulfurization. *Appl. Catal., A* **2003,** 239, 253-267.

116. Briggs, D.; Seah, M. P. Practical Surface Analysis by Auger and X-Ray Photoelectron Spectroscopy. *D. Briggs, & M. P. Seah,(Editors), John Wiley & Sons, Chichester* **1983**.

117. Sawhill, S. J.; Layman, K. A.; Van Wyk, D. R.; Engelhard, M. H.; Wang, C.; Bussell, M. E. Thiophene Hydrodesulfurization over Nickel Phosphide Catalysts: Effect of the Precursor Composition and Support. *J. Catal.* **2005,** 231, 300-313.

118. Burns, A. W.; Layman, K. A.; Bale, D. H.; Bussell, M. E. Understanding the Relationship between Composition and Hydrodesulfurization Properties for Cobalt Phosphide Catalysts. *Appl. Catal., A* **2008,** 343, 68-76.

119. Blanchard, P. E. R.; Grosvenor, A. P.; Cavell, R. G.; Mar, A. Effects of Metal Substitution in Transition-Metal Phosphides $(Ni_{1-X}M_X)_2P$ (M = Cr, Fe, Co) Studied by X-Ray Photoelectron and Absorption Spectroscopy. *J. Mater. Chem.* **2009,** 19, 6015-6022.

120. Anderson, N. C.; Hendricks, M. P.; Choi, J. J.; Owen, J. S. Ligand Exchange and the Stoichiometry of Metal Chalcogenide Nanocrystals: Spectroscopic Observation of Facile Metal-Carboxylate Displacement and Binding. *J.Am. Chem. Soc.* **2013,** 135, 18536-18548.

121. Seo, W. S.; Shim, J. H.; Oh, S. J.; Lee, E. K.; Hur, N. H.; Park, J. T. Phase- and Size-Controlled Synthesis of Hexagonal and Cubic CoO Nanocrystals. *J.Am. Chem. Soc.* **2005,** 127, 6188-6189.

122. Wang, J.; Johnston-Peck, A. C.; Tracy, J. B. Nickel Phosphide Nanoparticles with Hollow, Solid, and Amorphous Structures. *Chem. Mater.* **2009,** 21, 4462-4467.

123. Moreau, L. M.; Ha, D.-H.; Bealing, C. R.; Zhang, H.; Hennig, R. G.; Robinson, R. D. Unintended Phosphorus Doping of Nickel Nanoparticles During Synthesis with TOP: A Discovery through Structural Analysis. *Nano Lett.* **2012,** 12, 4530-4539.

124. Nam, K. M.; Shim, J. H.; Ki, H.; Choi, S.-I.; Lee, G.; Jang, J. K.; Jo, Y.; Jung, M.-H.; Song, H.; Park, J. T. Single-Crystalline Hollow Face-Centered-Cubic Cobalt Nanoparticles from Solid Face-Centered-Cubic Cobalt Oxide Nanoparticles. *Angew. Chem. Int. Ed.* **2008,** 47, 9504-9508.

125. D. Li, Y.; Q. Li, L.; W. Liao, H.; R. Wang, H. Preparation of Pure Nickel, Cobalt, Nickel-Cobalt and Nickel-Copper Alloys by Hydrothermal Reduction. *J. Mater. Chem.* **1999,** 9, 2675-2677.

126. Miao, H. J.; Piron, D. Electrodeposition of Ni-Transition Alloys for the Oxygen Evolution Reaction. *J. Appl. Electrochem.* **1991,** 21, 55-59.

127. Halck, N. B.; Petrykin, V.; Krtil, P.; Rossmeisl, J. Beyond the Volcano Limitations in Electrocatalysis - Oxygen Evolution Reaction. *Phys. Chem. Chem. Phys.* **2014,** 16, 13682-13688.

128. Ye, F.; Liu, H.; Yang, J.; Cao, H.; Yang, J. Morphology and Structure Controlled Synthesis of Ruthenium Nanoparticles in Oleylamine. *Dalton Trans.* **2013,** 42, 12309-12316.

129. Fruchart, R. Effets D'éLectronéGativité Et Interactions Metalliques Dans Les Phosphures Et Arseniures Ternaires Des Elements De Transition 3d, 4d, 5d De Type Metallique. *Ann. Chim. Fr.* **1982,** 7, 563-604.

130. Ohta, S. Magnetic Properties of 4d Metal Phosphides Containing Co and Ni. *J. Phys. Soc. Jpn.* **1996,** 65, 4090-4091.

131. Rundqvist, S. The Structures of Co_2P, Ru_2P and Related Phases. *Acta. Chem. Scand* **1960,** 14, 1961-1979.

132. Rundqvist, S. X-Ray Investigations of Mn_3P., Mn_2P, and Ni_2P. *Acta. Chem. Scand* **1962,** 16.

133. Fruchart, R.; Roger, A.; Senateur, J. Crystallographic and Magnetic Properties of Solid Solutions of the Phosphides M_2P, M= Cr, Mn, Fe, Co, and Ni. *J. Appl. Phys.* **1969,** 40, 1250-1257.

134. Gopalakrishnan, J. Chimie Douce Approaches to the Synthesis of Metastable Oxide Materials. *Chem. Mater.* **1995,** 7, 1265-1275.

135. Gao, M.-R.; Cao, X.; Gao, Q.; Xu, Y.-F.; Zheng, Y.-R.; Jiang, J.; Yu, S.-H. Nitrogen-Doped Graphene Supported $CoSe_2$ Nanobelt Composite Catalyst for Efficient Water Oxidation. *ACS Nano* **2014,** 8, 3970-3978.

136. Ryu, J.; Jung, N.; Jang, J. H.; Kim, H.-J.; Yoo, S. J. In Situ Transformation of Hydrogen-Evolving Cop Nanoparticles: Toward Efficient Oxygen Evolution Catalysts Bearing Dispersed Morphologies with Co-oxo/hydroxo Molecular Units. *ACS Catal.* **2015,** 5, 4066-4074.

137. Dutta, A.; Samantara, A. K.; Dutta, S. K.; Jena, B. K.; Pradhan, N. Surface-Oxidized Dicobalt Phosphide Nanoneedles as a Nonprecious, Durable, and Efficient OER Catalyst. *ACS Energy Lett.* **2016,** 1, 169-174.

138. Liu, G.; Li, P.; Zhao, G.; Wang, X.; Kong, J.; Liu, H.; Zhang, H.; Chang, K.; Meng, X.; Kako, T.; Ye, J. Promoting Active Species Generation by Plasmon-Induced Hot-Electron Excitation for Efficient Electrocatalytic Oxygen Evolution. *J. Am. Chem. Soc.* **2016,** 138, 9128-9136.

139. Danforth, S. J.; Liyanage, D. R.; Hitihami-Mudiyanselage, A.; Ilic, B.; Brock, S. L.; Bussell, M. E. Probing Hydrodesulfurization over Bimetallic Phosphides Using Monodisperse $Ni_{2-x}M_xp$ Nanoparticles Encapsulated in Mesoporous Silica. *Surf. Sci.* **2016,** 648, 126-135.

140. Diaz, A. L.; Bussell, M. E. An Infrared Spectroscopy and Temperature-Programmed Desorption Study of Carbon Monoxide on Molybdena/Alumina Catalysts: Quantitation of the Molybdena Overlayer. *J. Phys. Chem.* **1993,** 97, 470-477.

141. Liu, P.; Rodriguez, J. A. Catalysts for Hydrogen Evolution from the [NiFe] Hydrogenase to the Ni_2P (001) Surface: The Importance of Ensemble Effect. *J. Am. Chem. Soc.* **2005,** 127, 14871-14878.

142. Liu, P.; Rodriguez, J. A.; Asakura, T.; Gomes, J.; Nakamura, K. Desulfurization Reactions on Ni_2P (001) and A-Mo_2C (001) Surfaces: Complex Role of P and C Sites. *J. Phys. Chem. B* **2005,** 109, 4575-4583.

143. Layman, K. A.; Bussell, M. E. Infrared Spectroscopic Investigation of CO Adsorption on Silica-Supported Nickel Phosphide Catalysts. *J. Phys. Chem. B* **2004,** 108, 10930-10941.

144. Sun, Y.; Prins, R. Mechanistic Studies and Kinetics of the Hydrodesulfurization of Dibenzothiophene on Co–MoS_2/γ–Al_2O_3. *J. Catal.* **2009,** 267, 193-201.

145. Bowker, R. H.; Smith, M. C.; Pease, M. L.; Slenkamp, K. M.; Kovarik, L.; Bussell, M. E. Synthesis and Hydrodeoxygenation Properties of Ruthenium Phosphide Catalysts. *ACS Catal.* **2011,** 1, 917-922.

146. Sun, Z.; Zheng, H.; Li, J.; Du, P. Extraordinarily Efficient Photocatalytic Hydrogen Evolution in Water Using Semiconductor Nanorods Integrated with Crystalline Ni_2P Cocatalysts. *Energy Environ. Sci.* **2015,** 8, 2668-2676.

147. Layan Savithra, G. H.; Bowker, R. H.; Carrillo, B. A.; Bussell, M. E.; Brock, S. L. Mesoporous Matrix Encapsulation for the Synthesis of Monodisperse Pd_5P_2 Nanoparticle Hydrodesulfurization Catalysts. *ACS Appl. Mater. Interfaces* **2013,** 5, 5403-5407.

ABSTRACT

SYNTHESIS AND CHARACTERIZATION OF TRANSITION METAL PHOSPHIDE NANOPARTICLES FOR CATALYTIC APPLICATIONS: MODEL CATALYSTS FOR HYDRODESULFURIZATION AND ELECTROCATALYSTS FOR THE OXYGEN EVOLUTION REACTION

by

DON MALINDA RUCHIRA LIYANAGE

December 2016

Advisor: Dr. Stephanie L. Brock

Major: Chemistry

Degree: Doctor of Philosophy

Transition metal phosphides are emerging as efficient catalysts for different processes. Although binary phases have been extensively studied recently researchers have explored the synergism afforded by bimetallic ternary transition metal phosphides. The conventional catalyst preparation methods (temperature programmed reduction or solvothermal synthesis) yield inhomogeneous samples, preventing a detailed understanding of how active site density impacts catalytic activity and mechanism. In contrast, solution-phase arrested-precipitation reactions produce uniform nanoparticles with an excellent control on size, morphology and composition.

This dissertation describes the synthesis of ternary transition metal phosphide nanoparticles ($Ni_{2-x}Co_xP$ and $Ni_{2-x}Ru_xP$) by solution-phase arrested-precipitation reactions and evaluation of their composition-dependent catalytic activity (hydrodesulfurization (HDS) and oxygen evolution reaction (OER)).

Motivated by the enhanced HDS activity of Co-incorporated Ni_2P catalysts produced by TPR methods, a synthetic protocol was developed to produce phase-pure $Ni_{2-x}Co_xP$ ($x \leq 1.7$)

nanoparticles with sizes ranging from 9-14 nm. From TEM analysis, nearly monodisperse particles were obtained (S.D <20%) and metal ratios from EDS closely follow the ratios employed in the synthesis. Attempts to synthesize more Co-rich compositions yielded CoP as an impurity phase. The size distributions broaden with increasing Co content and hollow particles were observed for Co-rich compositions, due to the Kirkendall effect. In order to identify synthetic levers and the mechanism of ternary phase formation, a systematic study was conducted for Ni:Co = 1:1 as a representative composition. It was revealed that heating temperature, heating time, and the P:M ratio, have a huge impact on the nature of both the intermediate and the final crystalline particles. By tuning these conditions, NiCoP nanoparticles could be produced with different morphology (hollow vs dense) in different sizes (from ca 7-25).

Three nickel rich compositions of $Ni_{2-x}Co_xP$ (x= 0.08, 0.25, 0.5) prepared by solution-phase reactions were encapsulated in mesoporous silica and evaluated for dibenzothiophene (DBT) HDS activity. On a mass catalyst basis, the highest activity was observed for the x=0.08 composition at 623 K. A slight decrease in activity was observed with increasing the cobalt content. Nevertheless, the highest turnover frequency was observed for the most Co-rich composition tested (x=0.5). Detailed IR studies on CO adsorbed on the catalyst surface suggest an electron density increase in the Ni sites present in Co-rich materials, which could be attributed to the transfer of electron density from Co to Ni. All studied compositions prefer to undergo the direct desulfurization pathway (DDS) regardless of the Co amount.

Aiming to create an efficient, less-expensive catalyst for the oxygen evolution reaction (OER), a synthetic protocol was developed to prepare ternary metal phosphide nanoparticles, $Ni_{2-x}Ru_xP$, incorporating Ru, the state-of-art-catalyst for OER, and Ni, a highly active but inexpensive metal. Using solution-phase arrested precipitation reactions, crystalline $Ni_{2-x}Ru_xP$ particles could be

realized for compositions up to $x \leq 1$, whereas more Ru-rich compositions, including Ru_2P, were amorphous. For $x \leq 1$ particles are spherical, of sizes that vary between 5-10 nm in diameter (with a clear decreasing trend as the Ru amount is increased), and samples exhibit narrow size distributions (polydispersity <15%); whereas amorphous Ru-rich phases exhibit worm-like morphologies. ICP-MS data indicate the actual metal ratio closely follows the target ratio employed in the synthesis. OER electrocatalytic activity was evaluated for selected compositions over the entire synthesis range ($0 \leq x \leq 2$). Intriguingly, Ru_2P proved to be the least active phase (overpotential of 0.56 V at 10 $mA \cdot cm^{-2}$ in 1.0 M KOH) with the best performance observed for the bimetallic $Ni_{1.25}Ru_{0.75}P$ phase (overpotential of 0.34 V). The augmented activity at $x = 0.75$ is attributed, at least in part, to electronic activation of Ni by Ru, facilitating Ni oxidation and thus decreasing the kinetic barrier for OER.

Some preliminary HDS catalytic data were obtained for Ru-rich $Ni_{2-x}Ru_xP$ materials ($x=0.1$, 0.25, 0.5) encapsulated in mesoporous silica. It was observed 4.6-dimethyldibenzothiophene (4,6-DMDBT) HDS catalytic activity decreased with increasing the Ru content and the highest activity in all temperatures was shown by Ni_2P. Turnover frequencies calculated based on activity and chemisorption capacity mirrors the HDS activity trend, showing a decrease in activity with increasing Ru. Regardless of the Ru content all compositions undergo hydrogenation pathway (HYD).

AUTOBIOGRAPHICAL STATEMENT

DON MALINDA RUCHIRA LIYANAGE

Education

- 2011-2016 - PhD., Inorganic Chemistry, Wayne State University, Detroit, MI

Dissertation: Synthesis and Characterization of Transition Metal Phosphide Nanoparticles for Catalytic Applications: Model Catalysts for Hydrodesulfurization and Electrocatalysts for The Oxygen Evolution Reaction
Advisor: Prof. Stephanie L. Brock

- 2002-2007 – B. S. in Chemistry (Hons.) University of Sri Jayewardenepura, Colombo, Sri Lanka

Research Skills

- Schlenk line and glove box techniques, Powder X-ray Diffraction, Transmission Electron Microscopy, Energy Dispersive Spectroscopy, UV-Visible and Infra-Red Spectroscopy Thermo Gravimetric Analysis, Inductively coupled plasma- mass spectrometry, Surface area and Porosimetry Analysis

Research and Teaching Experience

- 20013-2016 Graduate Research Assistant, Wayne State University, Detroit, MI
- 2011-2013 Graduate Teaching Assistant, Wayne State University, Detroit, MI
- 2008 -2011 Graduate Teaching Assistant, University of Nebraska, Lincoln, NE

Affiliations

- American Chemical Society -member (Since 2010)

Awards

- Summer Dissertation Fellowship, Wayne State University -2016
- Thomas Rumble Fellowship, Wayne State University -2015
- Kokes Award -North American Catalysis Society-2015
- Vanderzee Fellowship in Physical Chemistry – University Nebraska Lincoln-(2008-2011)
- Chemical Industries (Colombo) Ltd. Prize, University of Sri Jayewardenepura -2006

Publications

- Liyanage, D. R.; Danforth, S. J.; Liu, Y.; Bussell, M. E.; Brock, S. L., *Chem. Mater.*, **2015**, 27, 4349 (One of the top downloaded papers for the month of June 2015)
- Samuel J. Danforth, D. Ruchira Liyanage, Asha Hitihami-Mudiyanselage, Boris Ilic, Stephanie L. Brock, Mark E. Bussell., *Surface Science*, 648, June **2016**, 126 (Special issue dedicated to Gabor Somorjai's 80 th birthday)
- Liyanage, D. R.; Da Li; Quintin B. Cheek; Brock, S. L., Synthesis and Oxygen Evolution Reaction (OER) Catalytic Performance of $Ni_{2-x}Ru_xP$ Nanocrystals: Enhancing Activity by Dilution of the Noble Metal. *submitted*